Investigation of phase transitions triggered by laser-induced focusing shock waves

Yevheniia Chernukha

UNIVERSITE MATIERE BRETAGNE MOLECULES LOIRE ET MATERIAUX

Le Mans Université

THESE DE DOCTORAT DE

LE MANS UNIVERSITE
COMUE UNIVERSITE BRETAGNE LOIRE

ECOLE DOCTORALE N° 596
Matière, Molécules, Matériaux
Spécialité : « *Science des matériaux* »

Par

« Yevheniia CHERNUKHA »

« Investigation of phase transitions triggered by laser-induced focusing shock waves »

Soutenu le 16 December 2019 à Rennes
Unité de recherche : Institut de Molecules et Matériaux du Mans, UMR CNRS 6283
Thèse N° : 2019LEMA1038

Rapporteurs avant soutenance :

Laurentiu STOLERIU	Professeur d'université, « Alexandru Ioan Cuza » University of Iasi, Romania
Laurent BERTHE	Directeur de recherche, PIMM, ENSAM-ParisTech, Paris

Composition du Jury :

President de jury :	Laurent BERTHE	Directeur de recherche, PIMM, ENSAM-ParisTech, Paris
Examinateurs :	Laurentiu STOLERIU	Professeur d'université, « Alexandru Ioan Cuza » University of Iasi, Romania
	Didier LOISON	Maître de conférence, Institut de Physique de Rennes, Rennes
	Marion HARMAND	Chargée de recherche, IMPMC, UMR 7590, Sorbonne Université, Paris
	Mathieu DUCOUSSO	Ingénieur-chercheur, SAFRAN, Paris

Dir. de thèse :	Thomas PEZERIL	Charge de recherche, IMMM, UMR CNRS 6283, Le Mans
Co-dir. de thèse :	Maciej LORENC	Directeur de recherche, IPR, UMR CNRS 6251, Rennes
Encadrante :	Marina SERVOL	Maître de conférence, IPR, UMR CNRS 6251, Rennes

Acknowledgements

At this very end of my thesis, I refer myself to all three years passed. At this moment I would like to express my greatest gratitude to all people who contributed to my thesis research for their support and encouragement. This work is a significant step in my professional life and it would never have been completed without each of you.

First and foremost, I sincerely thank my supervisors Thomas PEZERIL and Maciej LORENC, who accepted me as a PhD student three years ago. Both of them became true mentors for me and their contribution cannot be under-assessed. With a careful and permanent supervision, they always permitted and encouraged my autonomy. I highly appreciate all our discussions, your laconic and fruitful advices as well as all your support during these years. What I learned from both of you, makes me a better person and better scientist, I want to believe.

Any scientific project is a teamwork and it was my pleasure to collaborate and communicate with many brilliant scientists during my thesis: Marina SERVOl for her dedicated time, permanent energy and positive way of thinking; Etienne JANOD for scientific discussions, his availability and suggestions; Bertrand TOUDIC for his constructive critics and valuable comments on my presentation skills.

I deeply thank to Keith A. NELSON for inviting me to his group at MIT as a visiting scholar, and especially to David VEYSSET, Steven E. KOOI and Dmitro MARTYNOWYCH, who sacrificed a lot of their time to help me during my stay at MIT. Thanks!

My working time was split between two universities and two scientific groups. I thank all current and former members of "NOVA" group (IMMM, Le Mans) and "Materials and light" group (IPR, Rennes). I enjoyed working in such a pleasant and friendly atmosphere.

I want to thank to my friends: Rostyslav DANYLO, Ievgenia CHABAN, Tymur PARPIEV, Danylo BABICH, Oxana CHERKAS, Marina SANALATII, Borys SHCHUKIN, Alexander ALEKHIN, Artem LEVCHUK, Ela TRZOP, Evgenia SHABALINA and others whom I probably forgot to mention. I will remember our time together and feel so happy that I have met all of you!

Finally, I want to thank my familly. I am who I am thanks to my Mom, Dad and my younger sister. They helped me to survive in the darkest times and I am here thanks to their endless trust in me. Thank you!

Abstract

The ability of certain materials to change its ground state due to laser excitation has arisen a lot of opportunities for light-control of material properties. The field of photo-induced phase transitions counts a rich variety of chemical and physical processes triggered by light-matter interactions involved during the phase transition process. Recently it was reported that elastically driven cooperativity leads to the amplification of spin state in molecular crystals and prolonged the lifetime of the transient state with an ultra-short laser pulse. The cooperative response appears during the propagation of non-linear coherent strain waves, in other words shock waves, coupled with the order parameter field. Shock waves can be seen as a new challenging pathway to achieve a permanently switched state with appropriate excitations.

The main objective of this thesis was to establish if a shock wave can lead to a permanent phase change in materials undergoing photo-induced transitions. First, we introduce time-resolved single-shot imaging combined with the laser shock focusing technique that makes it possible to generate, acoustically focus, and directly visualize under a microscope shock waves propagating and focusing along the sample surface. The spatial separation of the laser-influenced and strain-influenced regions make it possible to disentangle the material changes produced solely by the shock waves. Second, we present experimental results of applying the shock-focusing technique to materials undergoing phase transitions linked with a macroscopic change of their volume (spin-crossover systems, Mott insulators). Post-mortem analyses of the samples confirm permanent phase transition under specific experimental conditions. These innovative results open doors for a generic elastically driven cooperativity.

Keywords: laser ultrasonics, shock waves, phase transition, bi-stable materials, elastic cooperativity.

Résumé

La capacité de certains matériaux à changer d'état fondamental sous excitation laser a ouvert un champ de recherche autour de la manipulation de leurs propriétés par la lumière. Les processus chimiques et physiques mis alors en jeu sont riches et complexes. Dans ce contexte, le rôle prédominant de la coopérativité élastique pour l'amplification et la stabilisation de la transition a été mis en évidence récemment dans un matériau à transitions de spin irradié par laser. Ces observations font apparaître la perspective de commuter de façon permanente certaines propriétés des matériaux par des ultrasons non-linéaires, des ondes de choc excitées par laser.

Le principal défi de cette thèse a concerné la démonstration expérimentale du rôle important, voir prédominant, des ondes de choc lors des processus de transitions de phase photo-induites dans divers matériaux. Dans un premier temps, nous introduisons le dispositif expérimental d'imagerie mono-coup résolu en temps, associée à la technique de focalisation des ondes de chocs excitées par laser au niveau de la surface de l'échantillon. La séparation spatiale des régions irradiées par le laser et influencées par les ondes de choc propagatives permet de discerner clairement les changements du matériaux induits uniquement par les ondes de choc. Dans un second temps, nous présentons nos résultats expérimentaux en lien avec cette technique innovante, aux matériaux dont les changements de phases impliquent un changement de volume macroscopique (systèmes spin-crossover, isolants de Mott). Des analyses post-mortem des échantillons ont permis de confirmer, dans certaines conditions expérimentales, une modification permanente de la phase du matériau par action de l'onde de choc. Ces résultats ouvrent de nombreuses perspectives pour la généralisation à de nombreux matériaux du phénomène de coopérativité élastique donnant lieu à des transitions de phases permanentes.

Mots-clés : ultrasons générés par laser, ondes de choc, transitions de phase, matériaux bi-stables, coopérativité élastique

Contents

Chapter 1

Introduction

We do not see the shock waves in everyday life but they can be easily found in the nature. The simplest way to generate a shock wave is using a bull whip. We all hear a "crack" sound when snapping a whip. This happens when a disturbance wave traveling down the whip exceeds the speed of sound. While snapping, the momentum from the motion at the handle is conserved. Because the rope used in the bull whip narrows from the handle to the tip, the wave speed increases as it travels down the whip. When the velocity of the wave crosses the speed of sound, it generates a sonic boom that we hear as a crack.

Such events, as *volcano eruption i.e.* a rupture in the crust of the Earth, that allows hot lava, volcanic ash, and gases to escape from a magma chamber below the surface happening because of pressure changes within the volcano due to the movement of tectonic plates) leads to the formation of the shock waves. They can be used to get information about eruption dynamics [1, 2].

When planets collide with each other or other space particles, the gravitational acceleration causes high-velocity impacts that launch high-pressure and often long-duration shock waves [3, 4]. Shock waves also can be generated by strongly ablating meteorites with the size greater than a few millimetres [5]. For example, during *2013 Russia meteor event*, a meteor entered into the Earth's atmosphere. The meteor's shock wave produced damages as in a supersonic jet's flyby (directly underneath the meteor's path) and as a detonation wave, with the circular shock wave centred at the me-

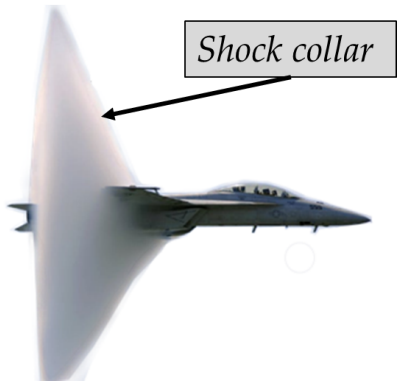

Figure 1.1 *– Illustration of aircraft moving at supersonic speed and a vapor cone formed due to the shock wave.*

teor explosion, causing multiple instances of broken glass in the city of Chelyabinsk and neighbouring areas.

Shock waves appear due to a sudden instantaneous pressure/temperature change in the environment and whenever the different elements of a fluid or solid approach one another with a velocity higher than the local speed of sound (see Figure 1.1). The shock wave physics always was a part of a small branch of physics and through the ages, it became an important interdisciplinary science that gained increasing interest in the scientific community at the beginning of the 19th century. In 1808 Poisson mentioned an intense sound wave as the case 'where the molecule velocities can no longer be regarded as very small'. Stokes (1848) used the term 'surface of discontinuity' and Riemann (1859) introduced the modern term of 'shock compression' and 'compression wave' to illustrate a jump like steepening of the wavefront. However, Toepler in 1864 was the first to use the term *shock waves* in the today's sense after he successfully visualized a shock wave during an electric spark discharge process using a stroboscopic method. The whole historical evolution of this field of science can be found in the book of P. Krehl 'History of Shock Waves, Explosions and Impact' [6].

Classical illustrations of the formation of a steep front in a discontinuous medium is a cartoon 'a train of skiers' from Courant and Friedrichs' book on supersonic flow [7] (Figure 1.2). The skiers in a line go down the narrow run. If the first one skier gets wrapped around a tree and then the

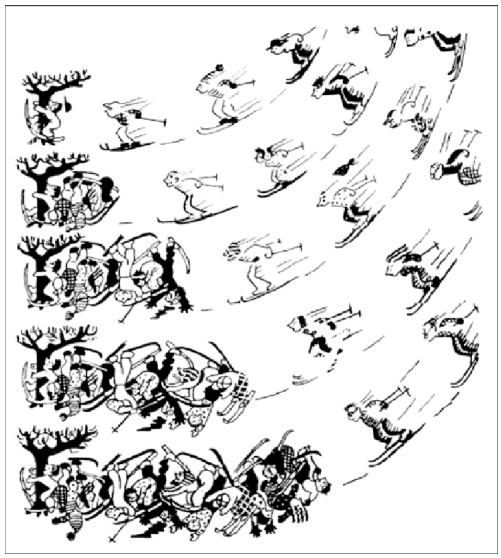

Figure 1.2 *– An example of a receding shock wave: a train of skiers formed when the first skier crashed into the tree and had no time to warn the next one, represents a steep front that moves faster than the medium can respond to new conditions* [7].

next skier crashes into him before being warned, they start to pile up in a heap. Analogously to a receding shock front, the pileup of humans creates a steep front moving up the slope away from the tree. The fact that the first skier didn't have time to warn the next one to slow down is crucial. It represents the condition of the 'supersonic' flow in the sense that it moves faster than medium (skiers) can not respond to a new boundary condition (first crushed skier).

The experimental methods used to generate planar shock waves in the laboratory conditions are:

- explosive devices based on condensed high explosives;
- gas-type launchers, such as powder guns, light-gas guns and ballistic shock tubes;
- devices using a laser source make it possible to produce a high shock pressure at the nanosecond timescale.

High energy pulsed laser allows for the generation of the shocks at significantly high pressure but of shorter durations in contrast with the other

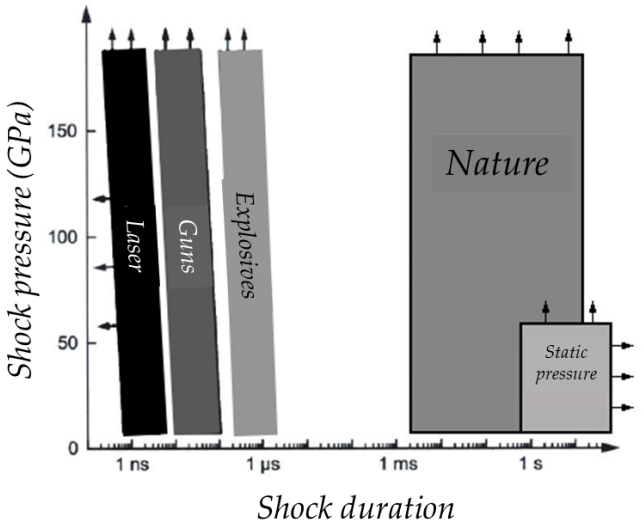

Figure 1.3 – *Characteristic shock pressure and duration ranges according to different shock generation methods. Adapted from* [*8*].

methods (Figure 1.3). Comparing to conventional generators of shock, these particular characteristics offer the possibility to study, reproduce and analyse in the laboratory environment the materials behaviour under extreme conditions at previously unexplored timescales (shorter than ns).

Shock waves have a variety of applications. First and obvious one is using shock waves to produce a strong level of traction leading to the damage of the material or *spallation* [9]. Effects associated with the shock phenomena such as the combination of strong temperatures and pressures are used to carry out the synthesis of new materials. Materials processing uses a process called *laser shock peening* to increase a material's resistance to failure or fatigue over time [10].

Shock wave destructive feature causes the creation of a variety of application for example, in medicine - *extracorporeal shock wave therapy*. Nowadays shock waves are the first choice to treat kidney and urethral stones through disintegration [11]. They used a shock wave, generated outside the body, for example, to destroy a kidney stone. Dose-dependent stimulus

from shock waves is seen to engender tissue regeneration and restoration in various pathologies [12]. Such a method is safe, effective and allows no surgical invention.

In recent years plenty of investigations were made in the field of shock waves: influence of shock wave on properties of materials [13–21], shock wave loading [22–24], medical treatments [25, 26], cavitation and sonoluminescence [27–29], *etc*.

Dynamic compression feature of the shock wave makes them very attractive method for the investigation of different types of phase transitions [30–32]. For example, Jones et al. [33] investigate a $\alpha - \omega$ phase transition in shock-loaded titanium. They revealed a conversion of the $\sim$65% of initially α into ω phase due to shock propagation. Zhao et al. in [34] studied the amorphization of silicon single crystals under high-powered short-duration laser-driven shock compression. Kraus et al. have observed a transition to a diamond for pyrolytic and polycrystalline graphite under shock compression in [35].

This thesis presents an investigation of the shock wave influence on the materials exhibit multistability at certain conditions - spin crossover and Mott insulators. Both types of materials undergo a photo-induced transition and volume is one of the parameters to control. A shock wave, in its turn, represents a dynamically propagated pressure package that can change the volume of the mater potentially used for investigation of phase transition in volume-changing materials. The main goal of this work was to demonstrate if a single shock wave can lead to a permanent transformation of the material with multistability.

The manuscript contains five chapters.

After a brief description of different types of acoustic waves, Chapter 2 introduces all types of acoustic waves that can be generated, the theory behind the formation of the shock waves and a laser generation method that was used in this work. Excitation with a shaped laser beam allows us to separate the shock-influenced and laser-influenced regions which makes it possible to investigate changes produced only by the wave.

The experimental and instrumental development are provided in Chapter 3. The general concept of the imaging methods as well as a technical description of an all-optical single-shot time-resolved imaging system are introduced. The experimental setup makes it possible to generate, focalize

and record a shock wave propagation on the sample surface. We describe a daily procedure of the sample assembling depending on the nature of the investigated material. Finally, we demonstrate typical results and information that we can get using our experimental method and its connection to the multistable materials.

After an introduction to a spin-crossover transition and precise description of the specific compound, Chapter 3 shows a developed method and technical aspects of the performed experiments. Special attention in this section is devoted to a new developed sample cell that makes it possible to control the temperature of the sample in the range $0\,^{\circ}\mathrm{C}$ - $120\,^{\circ}\mathrm{C}^{\circ}\mathrm{C}$. Towards the end, we demonstrate preliminary results and a future investigation direction.

Chapter 4 is devoted to another type of phase transition material - Mott insulators. At the beginning, we introduce a principle of the insulator-to-metal transition in the canonical Mott system - vanadium oxide, V_2O_3. It represents a first study of Mott insulators' behaviour under shock loading. A post-mortem analysis of shocked regions opens a door to a big discussion on the nature of the permanent insulator-to-metal transition induced by a purely elastic process.

Chapter 2

Linear and nonlinear acoustic waves

An *acoustic wave* is a type of mechanical wave where pressure variation propagates through a material. Typically, this term is associated only with sound waves, but in general it also covers all the mechanical vibrational motions of the medium. Acoustic waves in solids are periodic oscillations of molecules that propagate in the material due to the action of elastic forces. The velocity of this motion is called *the speed of sound* and depends on the material. Depending on the nature of the material (gas, liquid or solid) different types of acoustic waves can be excited: longitudinal, shear, Rayleigh, etc. If pressure variation of these waves is relatively small we have to deal with the linear acoustics. But in the case where this variation is significantly large, we have a non-linear acoustic wave that is called *shock wave*. We will take a quick look at both cases and describe all waves that can be excited with a laser pulse. Also, we will present a possibility to focalize generated waves to obtain amplification of propagating pressure, as well as our approach that was used in this work.

2.1 Waves in elastic medium

2.1.1 Waves in infinite medium: bulk waves

For a 3D medium the mechanical displacement can be expressed in terms of the displacement vector $\vec{u} = u_j\vec{i}_j$ and the deformation by the strain tensor:

$$\epsilon_{ij} = \frac{1}{2}(u_{i,j} + u_{j,i}) \tag{2.1}$$

where $i, j = x, y, z$. For the sake of simplicity, let us consider a homogeneous isotropic elastic medium. This medium is described by its density ρ and by two Lamé constants λ and μ, which may be related to another elastic constants: Young's modulus E and Poisson's ratio ν by:

$$\nu = \frac{1}{2}\frac{\lambda}{\lambda\mu} \qquad\qquad E = 2\mu(1+\nu) \tag{2.2}$$

Application of the external stimuli on elastic material will create a deformation and stress generation but when the forces vanish, it returns to its initial size. The stress vector $\vec{\sigma}$ is defined as the force applied on the surface area: $\vec{\sigma} = d\vec{F}/ds$. According to Hooke's law, for a non-piezoelectric body, the stress is related to strain by:

$$\sigma_{ij} = C_{ijkl}\epsilon_{kl} \tag{2.3}$$

where C_{ijkl} is the elasticity tensor of the medium. The material called *elastically homogeneous* if the coefficients C_{ijkl} are constants and *elastically isotropic* with no preferred direction in the material. The elastic constants are the same whatever the orientation of a coordinate system is. Elastic isotropy indicates that the elasticity tensor can be expressed as:

$$C_{ijkl} = \lambda\delta_{ij}\delta_{kl} + \mu(\delta_{ik}\delta_{jl} + \delta_{il}\delta_{jk}). \tag{2.4}$$

Thus, strain-stress relation can be re-written as:

$$\sigma_{ij} = \lambda\epsilon_{kk}\delta_{ij} + 2\mu\epsilon_{ij}. \tag{2.5}$$

By substituting the (2.1) into (2.5) we will get equation of motion (Navier's equation) for the displacement in absence of external forces:

$$(\lambda + \mu)u_{j,ij} + \mu u_{i,ji} = \rho\frac{\partial^2\vec{u}}{\partial t^2}. \tag{2.6}$$

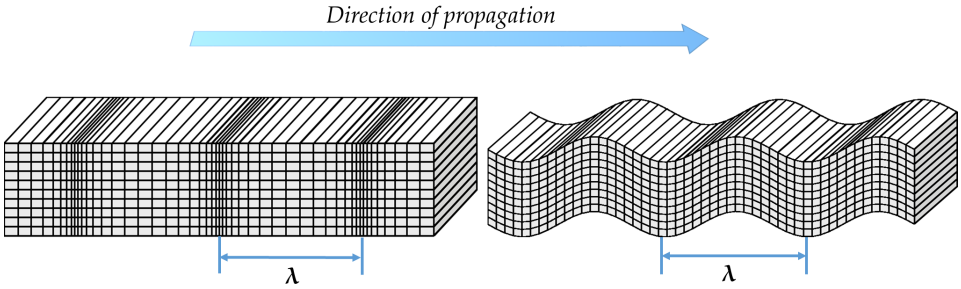

***Figure 2.1** – Longitudinal (right) and shear (left) waves propagating in the same direction (λ represents the wavelength) [36].*

The equation of motion in vector notation can be written as:

$$(\lambda + \mu)\nabla\nabla \cdot \vec{u} + \mu\nabla^2\vec{u} = \rho\frac{\partial^2\vec{u}}{\partial t^2} \tag{2.7}$$

Using Helmholtz's theorem, we can represent a displacement vector as a sum of a gradient of scalar Φ (irrotational part) and a curl of a zero-divergence vector $\vec{\Psi}$ (solenoidal part):

$$\vec{u} = \nabla\Phi + \nabla \times \vec{\Psi}. \tag{2.8}$$

These potentials satisfy the wave equation (2.7) if:

$$\nabla^2\Phi = \frac{1}{c_L^2}\frac{\partial^2\Phi}{\partial t^2} \qquad \nabla^2\vec{\Psi} = \frac{1}{c_T^2}\frac{\partial^2\vec{\Psi}}{\partial t^2} \tag{2.9}$$

where c_L and c_T represent the phase velocities of the bulk elastic longitudinal (compression) and transverse (shear) waves, respectively:

$$c_L = \sqrt{\frac{\lambda + 2\mu}{\rho}} \qquad c_T = \sqrt{\frac{\mu}{\rho}} \qquad \frac{c_T}{c_L} = \sqrt{\frac{1-2\nu}{2(1-\nu)}} \tag{2.10}$$

Poisson's ratio for all real media set in a range $0 \leq \nu \leq 0.5$, so $c_L > c_T$: the longitudinal waves travel faster than the transversal ones. The acoustic displacement of the medium is parallel to the direction of the propagation in the case of longitudinal waves and perpendicular to the propagation direction in the case of shear waves (Figure 2.1).

2.1.2 Waves in semi-infinite media - surface acoustic waves

In case of an unbounded medium only longitudinal and shear waves can propagate. But if a boundary is introduced and the medium is able to maintain both longitudinal and shear waves, the third type of waves - a *surface waves* that propagate along the boundary, can be generated. Surface waves combine both longitudinal and shear motion - particles moves in an ellipsoidal trajectory near the surface of the solid.

There are several types of surface waves.

Rayleigh waves. Surface acoustic waves (SAW), also known as *Rayleigh waves*, were discovered by Lord Rayleigh in 1885 [37]. He studied their contribution to earthquakes and showed that they decrease rapidly with depth and travel at lower velocities than bulk waves.

Let us consider the case of a free interface at the surface of a semi-infinite solid substrate (Figure 2.2). Let us assume that Rayleigh wave propagates along the x-axis and so that all parameters are independent along y-axis. All derivatives with respect to y will be zero. Displacement vector (2.8) in this case can be write as:

$$\vec{u} = u_x\vec{i} + u_y\vec{j} + u_z\vec{k}; \tag{2.11}$$

where

$$u_x = \frac{\partial\Phi_x}{\partial x} - \frac{\partial\Psi_y}{\partial z}; u_y = \frac{\partial\Psi_x}{\partial z} - \frac{\partial\Psi_z}{\partial x}; u_z = \frac{\partial\Phi_z}{\partial z} - \frac{\partial\Psi_y}{\partial x}. \tag{2.12}$$

We can see that potentials Φ and Ψ_y appear in displacement components u_x and u_z, and Ψ_x, Ψ_z - in component u_y. Consequently, the wave motion in (x, z) plane (combination of longitudinal and shear motion polarized vertically) is independent from motion along y (shear motion polarized

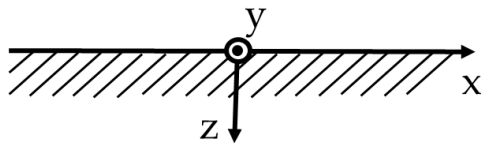

***Figure 2.2** – Coordinate system for free interface of a semi-infinite solid* [38].

horizontally). Thus, we can decompose the potential $\vec{\Psi}$ into two parts respectively:

$$\vec{\Psi} = \vec{\Psi_y} + \vec{\Psi_{x,z}}; \tag{2.13}$$

$$\vec{\Psi_y} = (0, \Psi_y, 0); \tag{2.14}$$

$$\vec{\Psi_{x,z}} = (\Psi_x, 0, \Psi_z). \tag{2.15}$$

We will look only at particle motion in (x, z) plane, so vector $\vec{\Psi}$ has only one non-zero component Ψ_y. Two potentials Φ and $\vec{\Psi}$ that form a displacement vector $\vec{u}$ can be described as:

$$\Phi = f(z)e^{i(kx-\omega t)} \tag{2.16}$$

$$\Psi_y = h(z)e^{i(kx-\omega t)}. \tag{2.17}$$

Substituting equation (2.16) and (2.17) into (2.9) we will get:

$$\frac{d^2 f}{dz} = k^2 - \frac{\omega^2}{c_L^2} f \qquad\qquad \frac{d^2 h}{dz} = k^2 - \frac{\omega^2}{c_T^2} h \tag{2.18}$$

The solutions are waves with exponentially decreasing and increasing parts:

$$\Phi = Ae^{-\alpha z}e^{i(kx-\omega t)}, \qquad\qquad \Psi_y = Be^{-\beta z}e^{i(kx-\omega t)} \tag{2.19}$$

where

$$\alpha = k - \frac{\omega}{c_L} \qquad\qquad \beta = k - \frac{\omega}{c_T} \tag{2.20}$$

Using the equation for the displacement vector (2.8) and stress (2.5) and applying to them the boundary conditions at the free surface $\sigma_{zz} = \sigma_{xy} = 0$, we will get two homogeneous equations for constant A and B:

$$(\beta^2 + k^2)A + 2i\beta kB = 0 \tag{2.21}$$

$$-2i\alpha kA + (\beta^2 + k^2) = 0 \tag{2.22}$$

These give us an equation for surface waves:

$$(\beta^2 + k^2)^2 - 4\alpha\beta k^2 = 0 \tag{2.23}$$

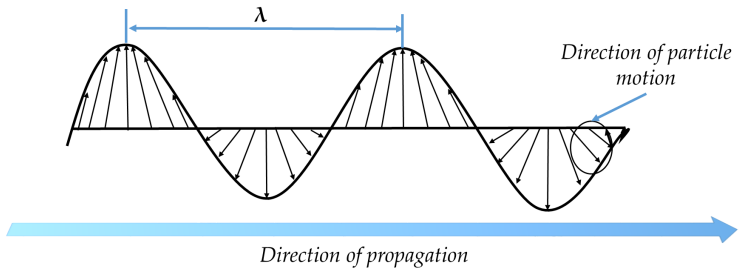

***Figure 2.3** – Particles motion of a Rayleigh wave during propagation*

By introducing a wave velocity $v = \frac{\omega}{k}$ and some rearrangements, we will get the so-called *Rayleigh equation*:

$$(\frac{v}{c_T})^2[(\frac{v}{c_T})^6 - 8(\frac{v}{c_T})^4 + (24 - \frac{16}{\xi^2})(\frac{v}{c_T})^2 - 16(1 - \frac{1}{\xi^2})] = 0 \tag{2.24}$$

with

$$\xi = \frac{2(1-\nu)}{1-2\nu} \tag{2.25}$$

It's easy to see, that (2.24) is a reduced cubic equation in $(\frac{v}{c_T})^2$ and the roots are dependent on Poisson's ratio ν through ξ. There will be three roots to the Rayleigh equation that depend on the value of the Poisson's ratio:

$$\nu < 0.263 \text{ - 3 real roots} \tag{2.26}$$

$$\nu > 0.263 \text{ - 1 real root and 2 complex conjugate roots.} \tag{2.27}$$

Complex roots will not be accepted because they result in attenuation with time, such if damping was present. An approximate expression that has been developed for Rayleigh velocity as a function of the Poisson's ratio is given by:

$$\frac{v_R}{c_T} = \frac{0.87 + 1.12\nu}{1+\nu}. \tag{2.28}$$

Rayleigh waves are the combination of shear-compressional movements which results in elliptic trajectory of molecules (Figure 2.3). The vertical component of the displacement is greater than the horizontal component at the surface. The penetration depth into the material is on the order of

the wavelengths of the Rayleigh wave. The motion decreases exponentially in amplitude with depth and becomes negligible for depths more than a few wavelengths. Additionally, because Rayleigh waves are confined to the surface and propagates only in 2D plane, they spread as $1/r$ in intensity while bulk waves spread as $1/r^2$, making surface waves dominant over bulk waves at the distance far from the generation point.

Other types of surface waves. Other types of surface waves exist, however they will only be mentioned here. A full description of all types of surface waves can be found in [39].

When dealing with interface, Rayleigh wave is referred to other types of waves: for interface formed by liquid-solid contact it is *Scholt wave* [40] and for solid-solid contact it is *Stoneley wave* (*Leaky Rayleigh Waves*) [41]. Both are similar to the Rayleigh waves, *i.e.* are guided by the interface, have the maximum intensity at the interface and decrease exponentially with depth.

When dealing with a material of a few wavelength thick we talk about *plate waves*. They include two waves: *Love waves* with particles motion parallel to plate layer and perpendicular to the propagation direction [42] and *Lamb waves* with particle motion perpendicular to the layer surface [43].

Sometimes a bulk wave can satisfy the boundary conditions on a surface and sliding along the surface. This kind of wave is called *Surface skimming wave* and it combines properties of SAW and bulk waves. The velocity of these waves is less than the velocity of a bulk shear wave [44].

2.2 Non-linear case - shock wave formation

The elastic waves considered above leads to the particles oscillations near their equilibrium position. Shock waves occur commonly in supersonic gas flows and can also occur in solid materials exposed to strong disturbances. During the elastic wave propagation in an elastic material, the stress is not greater than its elastic limit and there is no entropy change, which is not the case for the shock waves. During shock wave propagation, the material is stressed far beyond its elastic limit and there is an entropy increase.

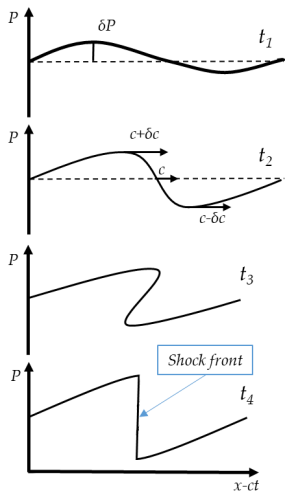

***Figure 2.4** – Self-steepening of a finite-amplitude sound wave. In the region where the state variables of the wave (pressure) would become multivalued (at t_3), irreversible processes dominate to create a steep, single-valued shock front* [45].

A shock wave can be described as a propagating surface with a discontinuous jump in the material properties. The thickness of the shocked layer is negligibly small as compared with other physically relevant dimensions. For example in atmospheric air it is about $0.25\,\mathrm{nm}$.

The problem of shock discontinuities was firstly investigated in the frame of gas dynamics by Stokes, Earnshaw, Riemann, Rankine, Hugoniot and Lord Rayleigh. Infinitesimal pressure changes generate linear compression longitudinal wave that travels with the local speed of sound $c = \sqrt{(\partial P/\partial \rho)_s}$. However if the amplitude of compression wave is significantly large, we will have the situation described in Figure 2.4. At the time t_1 we have the pressure variation $\delta P = P$. Variations in pressure imply variations in sound speed, thus each point of the waveform propagates with its local speed greater at the peaks than in trough. With time the waveform steepens as shown at t_2. Instead of eventual brakes (shown at t_3) to produce multiple values for the state variables, nature inserts a shock front just before the wave

breaks to maintain state variables single-valued (shown at t_4). This description means that all types of acoustic waves that were described above can become a shock wave with sufficiently applied force.

2.2.1 Rankine-Hugoniot relation

Assuming that heat conduction and radiative losses within the shock discontinuity can be considered negligible, all thermodynamic changes are adiabatic and reversible. Let us consider the situation where a piston suddenly compresses a gas (Figure 2.5), this will cause an increase in entropy and generate a shock wave.

Material before shock front is in its initial state with well defined density ρ_0, internal energy e_0, pressure P_0 and particle velocity $u_p = 0$. Material after shock front is compressed with density ρ_1, internal energy e_1, pressure P_1 and particle velocity $u_p \neq 0$ which is equal to speed of the piston. At time t, shock front is at A and propagates to S at time $t+dt$. The particles located initially at time t at A are moved to position B at time $t + dt$. The equation of conservation laws for mass, momentum and energy can be derived as follows:

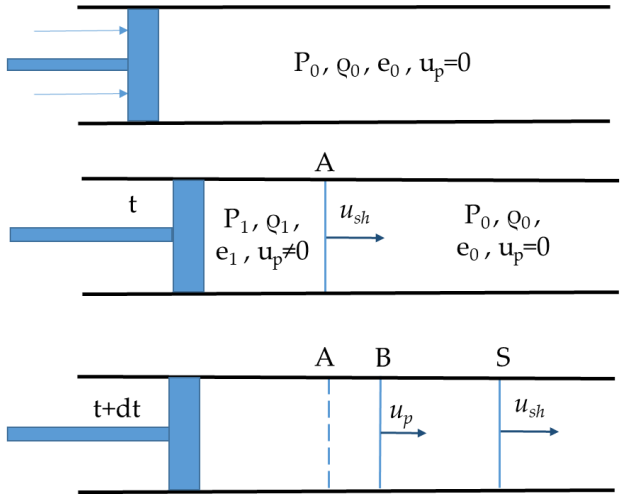

Figure 2.5 *– Schematic showing a sudden compression of a material and a discontinuity at the shock front. Adapted from* [46].

- *Conservation of mass*. At time t, mass of the material in defined cylinder $A - S$ is $\rho_0 u_{sh} dt$ and after time interval dt this region is compressed to $B - S$ with mass $\rho_1(u_{sh} - u_p)dt$. As a result we obtain

$$\rho_0 u_{sh} = \rho_1(u_{sh} - u_p) \tag{2.29}$$

  or

$$V_1 u_{sh} = V_0(u_{sh} - u_p) \tag{2.30}$$

  where $V = \frac{1}{\rho}$ is a specific volume .
- *Conservation of momentum*. Mass $\rho_0 u_{sh}$ acquires momentum $\rho_0 u_{sh} u_p$ which by Newton's law is equal to the impulse of pressure forces. The resulting force acting on the compressed gas is equal to the pressure difference:

$$P_1 - P_0 = \rho_0 u_{sh} u_p \tag{2.31}$$

  where $\rho_0 u_{sh}$ is the *shock impedance*.
- *Conservation of energy*. The compressive work done in dt equals the sum of the kinetic energy and the increase in internal energy:

$$P_1 u_p = \frac{\rho_0 u_{sh} u_p^2}{2} + \rho_0 u_{sh}(e_1 - e_0) \tag{2.32}$$

By eliminating u_{sh} and u_p in equation 2.32 using 2.30 and 2.31, we can easily obtain the *Rankine-Hugoniot relation* :

$$e_1 - e_0 = \frac{(V_0 - V_1)(P_1 + P_0)}{2} = \frac{(P_1 + P_0)}{2}(\frac{1}{\rho_0} - \frac{1}{\rho_1}) \tag{2.33}$$

When the initial state (V_0, P_0) ahead of the shock front and P_1 behind the shock front are given and we know the equation of state $(e = e(P, V))$ of the material, the Rankine-Hugoniot relation can be used to plot *the Hugoniot curve*, as shown in Figure 2.6.

This curve corresponds to all of the possible thermodynamic states that can be achieved for a given material in a well-defined set of initial conditions. A line joining the initial and final states represents the jump condition. It is called the Raleigh line (Figure 2.6). It means that states along the Hugoniot curve cannot be reached in any other way than during shock

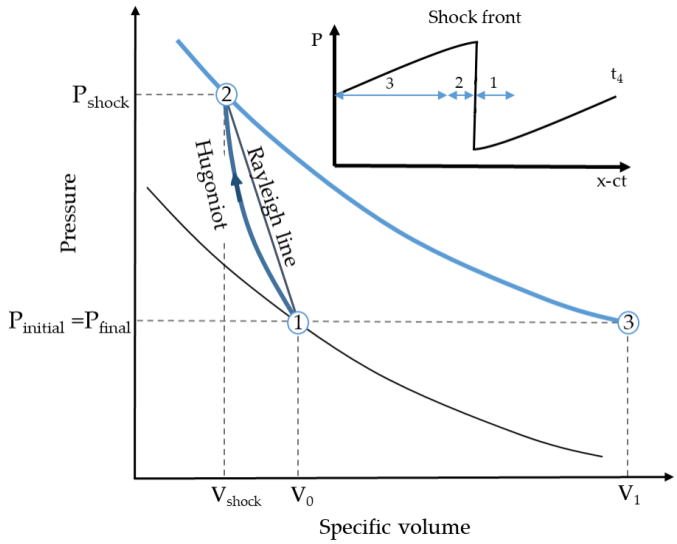

Figure 2.6 *– Hugoniot curve. The passage of a sound wave is a pressure and density oscillation along an adiabat, which is a reversible path. In contrast, the passage of a shock front causes the state jump along an irreversible path from point 1 to point 2, that is to higher pressure, density and entropy. The curve connecting these two states is called Hugoniot. It is followed by relaxation to point 3 along an adiabat, the, returning to its original pressure but higher temperature, entropy and a lower density.*

propagation. If we eliminate the particles velocity term u_p by manipulating the mass and momentum conservation equations(2.30-2.31), we get the following equation for the Rayleigh line:

$$P_1 - P_0 = \frac{u_{sh}^2}{V_0} - \frac{u_{sh}^2}{V_0^2} V_1 \tag{2.34}$$

The slope of this line is u_{sh}^2/V_0^2. If we know the initial and final states of the shock, we can calculate the shock speed from the Rayleigh line slope, and conversely, knowing shock speed and initial state can determine the final state.

Experiments have shown that for the majority of solid materials, the shock velocity u_{sh} and the particle velocity u_p can be empirically described

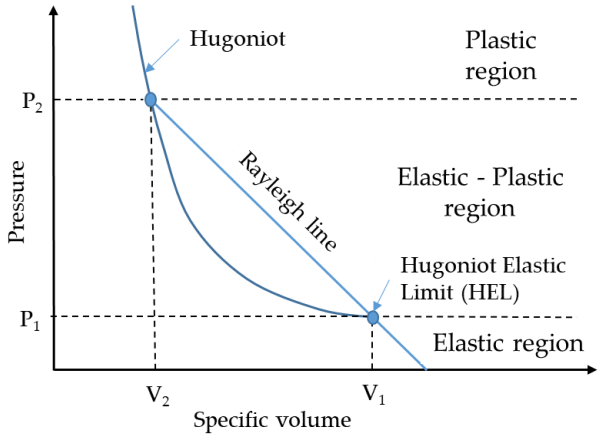

Figure 2.7 – *Hugoniot elastic limit for a shock in elastic-plastic material. Adapted from* [50].

in the regions where a substantial phase change in the continuum does not occur, via the following equation:

$$u_{sh} = c_a + hu_p. \tag{2.35}$$

where c_a is the ambient acoustic velocity and h is an empirical parameter. Tables with the parameters values of c_a, h can be found in literature for many materials. As it was mentioned before, to fully characterize the thermodynamic states of a material, we also need to know the equations of states (EOS). It can be, for example, Mie-Grüneisen equation for shock-compressed solids [47, 48] or the Tait equation for fluids [49].

An important assumption for deriving the Hugoniot relations is the neglect of material rigidity. For solids, material rigidity cannot be neglected since solids do not flow like fluids. Most solid materials undergo plastic deformation when expose to strong shocks. The point on the shock Hugoniot at which a material transition from a purely elastic state to an elastic-plastic state is called *the Hugoniot elastic limit* (HEL) (Figure 2.7) and pressure at which this transition takes place is denoted P_{HEL}. Values of P_{HEL} can range from $0.2\,\mathrm{GPa}$ to $20\,\mathrm{GPa}$ and depend on the types of material. Above the HEL, the material loses much of its shear strength and starts behaving like a fluid.

2.2.2 Shock wave attenuation due to rarefaction wave

A single shock pulse that represents a compression wave, is followed by so-called *rarefaction wave* that is an expansion wave. The expansion of the high-density material to a lower density does not take place instantaneously. The rarefaction wave will be generated by gas decompression.

When a material is shocked, its internal energy is increased, as expressed in Rankine-Hugoniot equation 2.33. To reveal the stress of the shocked material and to return it to the ambient pressure state we can apply a rarefaction wave on it. From thermodynamics we know that the energy change is equal to the difference between the entropy change at the absolute temperature and the work done:

$$dE = TdS - PdV \tag{2.36}$$

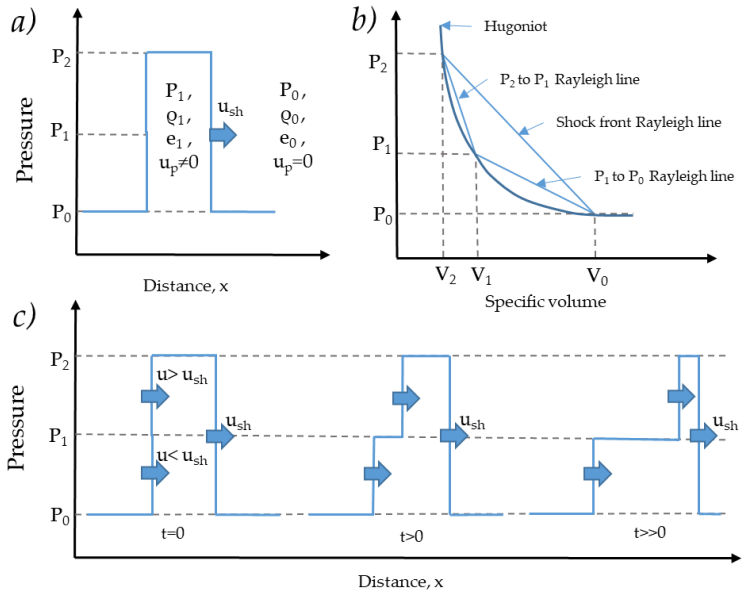

Figure 2.8 *– Schematic representation:* ***a****) square shock pulse with pressure drops in 2 steps:* $P_2 \rightarrow P_1$ *and* $P_1 \rightarrow P_0$ *;* ***b****) Hugoniot and Rayleigh lines for two rarefaction steps; c) the progress of the shock front and 2 rarefaction wavelets. Adapted from* [50].

Let assume that this process is adiabatic $dQ = TdS = 0$ since we didn't carry out this process at absolute zero, $dS = 0$. This means that during the process, the entropy must be constant, so the path of the changes in our state variables P, V must be along an isentrope. This means that we can rewrite 2.36 as:

$$dE = -PdV \tag{2.37}$$

Since we don't have the equation of states we refer to the Hugoniot.

The rarefaction unloads isentropically and we assume that the isentrope is the same as the values along the Hugoniot.

Here, we will treat the rarefaction as if it was a shock. Let us consider a shock pulse illustrated in Figure 2.8. We will apply the jump equations such that we will let the high-pressure material 'jump' down to a lower pressure state in two steps. The first step relieves the material from state P_1, V_1 (shock pressure) to P_2, V_2 (halfway down to ambient). The second wavelet drops the pressure from P_2 to P_0 (ambient). Look at the Rayleigh line for each of these jumps. Remembering that the slope of the Rayleigh line is proportional to the shock speed, we see that the first wavelet has a higher slope than at the shock front which means that it is travelling faster than the shock. Consequently, the second wavelet is travelling slower than the shock front. If we let the steps get smaller and smaller, approaching zero, then indeed we can unload right along the Hugoniot. As soon as each of these infinitesimal steps approach a shock front, it will lose in amplitude. Consequently, the shock wave will attenuate during propagation due to rarefaction wave.
Stability of the formed shock front during propagation, discussed in [51–54], will not be discussed in the frame of this thesis but has to be studied in all following investigations.

To conclude, **depending on the material, due to an external stimuli we can excite a variety of elastic waves.** Each of them can become a shock wave with applying an appropriate amount of pressure. A shock wave, as an abrupt change in material properties, can dramatically change the material behaviour. Among all possible ways of acoustic wave generation, we will address those that involve lasers.

2.3 Laser acoustic wave generation

2.3.1 General principles

Laser ultrasonic techniques are based on the generation of acoustic waves as a result of laser pulse interaction with a material surface. An overview of generation mechanisms can be found in [55, 56]. Here we will only address some basics.

Two regimes of ultrasonic generation depending on the laser energy are identified:

- Thermoelastic regime: generation occurs through homogeneous thermal expansion of the lattice after laser excitation.
- Ablation regime: generation occurs through an expansion of created plasma on the sample surface.

Thermoelastic regime. The absorbed light energy is converted to thermal energy, causing a local thermoelastic expansion of the material near the impact point (Figure 2.9(a)). The significant temperature rises occur only within the 'skin depth' (typically 1-10 nm for metals in the visible range) and the formed stresses will exist primarily in parallel to the surface (the ideal case boundary conditions imply no stress at the free surface).

Ablation regime. It occurs when high fluence (starting from $0.1\,\mathrm{J/cm^2}$ for some materials in case of picosecond pulses [57]), short wavelength

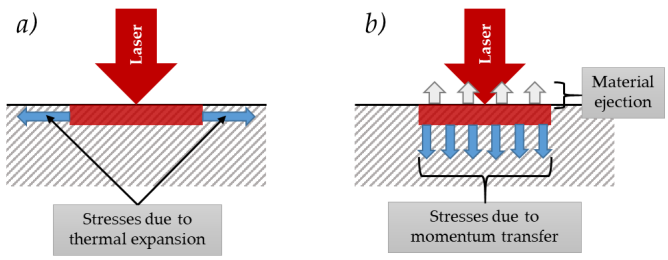

Figure 2.9 *– Photo-thermal generation of acoustic waves:* ***a****) Thermoelastic regime: local thermoelastic expansion of the material gives a rise to stresses and strains on the surface layer;* ***b****) Ablation regime: rapid heating and ionization of the material creates a high temperature plasma. Its expansion induces stresses and strains in depth of the material. Adapted from* [56].

laser radiation interacts with attenuating materials. In this case, a thermoelastic effect is accompanied by the ablation of electrons and ions, forming a plasma that expands away from the surface (Figure 2.9(b)). The resulting momentum pulse is transmitted into the material and causes stresses normal to the surface. This method leads to permanent damage of the material surface.

The efficiency of the acoustic waves generation can be increased by using a sacrificial layer on the top of the sample. Another way is to cover the surface with a glass or liquid that will modify the boundary conditions and stop expansion causing further amplification. The stress-free boundary at the surface no longer exists and this results in the development of normal stresses.

The thermoelastic method, contrary to the ablation method, is a non-destructive and, in mechanically isotropic materials, is responsible for the generation of longitudinal waves. Shear waves are more difficult to deal with and often imply using materials with broken axial symmetry. All surface waves can be generated by both regimes with typically higher amplitudes in the case of the ablation.

The laser fluence deposited on top of the material is the key parameter that allows to divide two regimes of generation. It is not only the energy of the laser pulse that plays a role but the pulse duration as well. Depending on the pulse duration, different physical processes are involved in the laser-matter interaction that induce acoustic waves. The overview of different processes can be found in [58–60]. For a laser pulse of fs duration the dominant process during the ablation is multi-photon ionization and tunnel effect: energy cannot be transferred from the electron gas to the ion network instantly (two-temperature model). For a long pulse duration (ns), the ablation process is dominated by heat conduction, melting, evaporation and plasma formation. The energy of the laser pulse is absorbed on the surface and heat conduction leads to the formation of a temperature field. A ps laser pulse involves the combination of these two regimes and is usually called 'intermediate regime'. This work is focused on the impact of acoustic waves on materials, and the generation process of such waves is only touched upon. However, it should be mentioned that for the further investigations this part would deserve dedicated investigations.

2.3.2 Laser generation of converging acoustic waves

In the frame of this thesis, we have used another method to increase the acoustic pulses amplitude. It applies performing acoustic focusing. The first observation of laser generation of converging acoustic waves was shown in [61, 62]. Authors excited an aluminium sample with the annular laser beam (Figure 2.10) in order to obtain larger ultrasound pulses without reaching the surface damaging ablation regime. They detected propagation of convergent and divergent surface acoustic waves (SAWs) using interferometer and confirm the increase in amplitude by a factor of 20. Also they noticed a variation of the SAW waveforms at different positions along the radial coordinate of the ring: at the position of ~ 10 SAW wavelength from the focal point, they observed a phase difference of π between the Fourier components of the SAW going towards the focus and the one that passed through the focus and going away from it. Such approach was investigated in [63] where authors discussed focusing of bulk waves generated by ring-shaped laser beams on aluminium plates. Wang *et al.*, experimentally showed a strong focusing effect at the center of the laser ring due to constructive interferences between waves generated by different parts of the excitation ring. Numerical simulations on this subject were performed in [64, 65] where finite element model (FEM) were used to simulate propagation of ultrasonic waves on aluminium plates generated by laser rings. These simulations confirmed the strong focusing and wavefront superposition at the center of the laser ring, both on top of the sample and in depth *i.e.* for both surface acoustic waves and bulk waves. In [66, 67], the authors

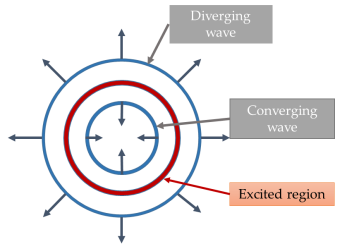

***Figure 2.10** – Sketch for ring-shaped laser pattern that induces waves for acoustic focalization.*

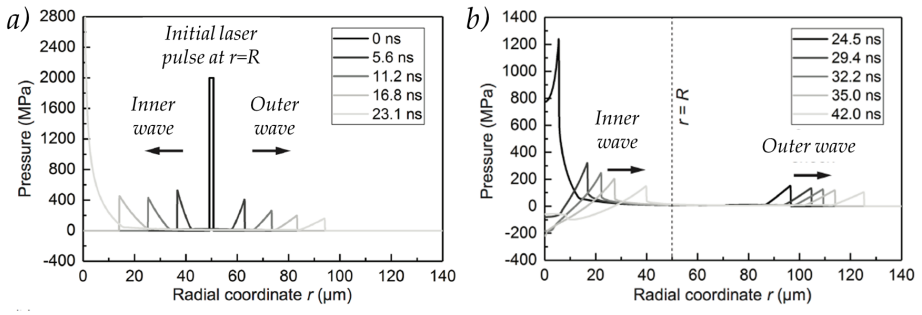

Figure 2.11 *– Numerical simulations of pressure profiles of laser induced shock waves at different times:* ***a****) profile changes with propagation before converging at the ring centre;* ***b****) profile changes with propagation after focalization: appearance of the tensile tail for inner wave coming from acoustic discontinuity at the centre. Adapted from* [68].

discussed the thermoelastic regime in case of annular excitation of acoustic waves. On thick samples, a ring patterned source generates simultaneously SAWs and bulk waves. SAWs travels outwards the laser ring and inwards towards the center of the laser ring, as it's shown in Figure 2.10. Authors indicated a difference in the acoustic profile between the initial SAW (going towards the center of the laser ring) and the secondary SAW (going back after focusing at the center): the secondary SAW is much broader in appearance and reduced in amplitude, which is the indication of the Gouy phase shift which will be discussed later in this section.

D. Veysset *et al.* [68] performed simulations of the shock wave propagation in thin liquid layer confined between two glasses induced by ring-shaped laser pulse. The simulations were done through solving a single component Euler equation with the stiffened equation of state for water [69]. They assume that the laser energy is deposited on a ring with radius $R = 50\,\mu\mathrm{m}$, $1.6\,\mu\mathrm{m}$ width and initial pressure pulse of $P = 2\,\mathrm{GPa}$. Figure 2.11 shows the time evolution of the pressure profile of the shock wave. It indicates a decrease in amplitude for diverging wave and a large increase of the shock pressure for the converging wave at the focal point. This amplification cause by spacial overlap and geometrical confinement of the shock wave. Initially unipolar pulse of the inner wave transforms into

bipolar after converging centre. This bipolar pulse has a positive pressure front and negative pressure tail. It forms due to the discontinuity at the focal point and the occurrence of the Gouy phase shift. This phase shift was first observed by Gouy in 1890 and was shown to exist for any waves, including acoustic waves, that pass through a focus. In [70] R. Boyd explains the Gouy phase shift in terms of the difference in propagation of the Gaussian beam and a plane wave. A Gaussian beam can be considered as a super- position of plane waves with different propagation directions. Those plane waves components with propagation directions different from the beam axis experience smaller phase shifts in the z direction; the overall phase shift arises from a superposition of all these components. In other words, Gaussian beam acquires a phase shift along the propagation direction that differs from that of a plane wave propagating with the same optical frequency. This difference is known as the Gouy phase shift. The same phenomena was observed in [66, 71, 72], not only for SAWs but also for converging bulk waves. **Gouy phase shift should be taken into account for all the converging waves.**

In all the examples described above, ring-shaped laser beams were obtained by using a conical lens Axicon. There are different ways to induce converging acoustic waves in a sample, for example, by using a spatial light modulator (SLM) instead of an Axicon to shape the laser beam into a ring [73], or by using a double line irradiation pattern described in [74] where authors exited a shear-vertical wave which produced a convergence effect at the central axis with a fixed angle.

2.4 Acoustic waves in layered samples

A laser pulse focalized on the sample surface can generate a variety of different acoustic waves. With an enough powered laser pulse we can reach the shock front formation and the acoustic wave becomes a shock wave. By using an approach of converging waves generation we can amplify the shock pressure at the focal point. Technical details of the experiment and sample preparation will be presented in Chapter 3. Here we want to summarize all information.

In this thesis, we used a ring-shaped laser pulse for the generation of the acoustic waves. Depending on the sample nature (liquid or solid) different

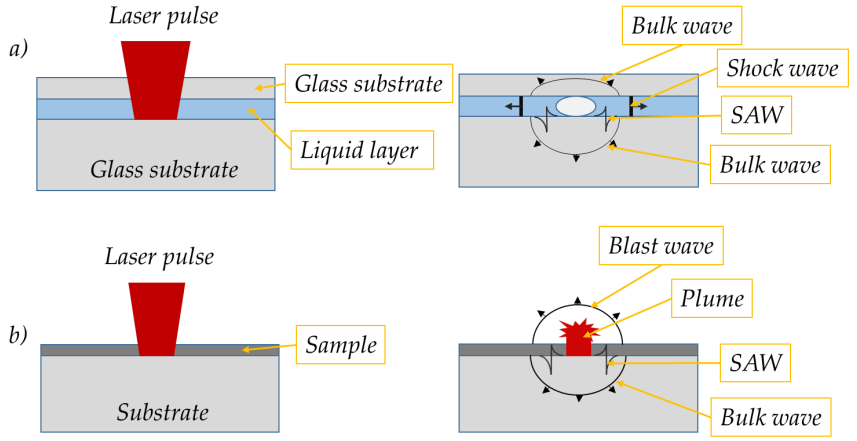

***Figure 2.12** – Sketch of possible excite acoustic waves in different samples: **a**) thin liquid layer; **b**) thin film on the substrate.*

sample configurations were used. In addition, based on the sample nature we also expect different types of acoustic waves to be generated.

In case of thin liquid layer sandwiched between two glass substrates, the main exciting wave will be a cylindrical bulk shock wave. Depending on the power of laser pump pulse we can expect to generate surface waves on the solid/liquid interface. Also, we will generate bulk waves in both substrates (Figure 2.12 (a)).

In case of a thin film deposited on top of the substrate, we can excite surface waves, that will propagate on the interface between thin film and substrate; body wave that will propagate in the substrate; and blast wave that will propagates in the air near thin film surface (Figure 2.12 (b)).

Our main interest is to observe the effect of the in-plane propagated waves (in case of different samples can be SAW, shock wave in a liquid, surface skimming wave) on the sample behaviour and surface morphology.

Because we will be using a laser excitation technique, the wavelength of the generated acoustic waves will be in order of the width of the excitation ring [55]. In this work, the width of the laser ring is in the order of ten microns. The characteristic time of acoustic wave propagation (t_{ac}) and characteristic time of heat diffusion (t_{heat}) towards the center of the laser

Table 2.1 – *Physical properties of materials* [77]

Material	Speed of sound	Thermal diffusivity
Water	$1.45\,\mathrm{km/s}$	$1.43\cdot10^{-7}\mathrm{m}^2/\mathrm{s}$
Glass	$5\,\mathrm{km/s}$	$3.4\cdot10^{-7}\mathrm{m}^2/\mathrm{s}$
Sapphire	$10\,\mathrm{km/s}$	$1.5\cdot10^{-5}\mathrm{m}^2/\mathrm{s}$
Ethanol	$1.14\,\mathrm{km/s}$	$7\cdot10^{-8}\mathrm{m}^2/\mathrm{s}$
Ti_3O_5	$10\,\mathrm{km/s}$ [78]	$4\cdot10^{-6}\mathrm{m}^2/\mathrm{s}$[78]
V_2O_3	$6\,\mathrm{km/s}$ [79]	$1.4\cdot10^{-6}\mathrm{m}^2/\mathrm{s}$

ring can be calculated using following formulas:

$$t_{ac} = R/v_{ac} \qquad\qquad t_{heat} = R^2/\chi \tag{2.38}$$

where R is the ring radius, v_{ac} - the speed of sound in the media and χ is the thermal diffusivity of the material. Table 2.1 illustrates the acoustic and thermal properties of different materials that were used in the experiments. Ti_3O_5 and V_2O_3 are the samples that will be discussed in Chapter 5. Thermal diffusivity for V_2O_3 was obtained from thermal conductivity [75] and specific heat capacity [76].

According to a simple calculation acoustic waves reach the centre of the ring in tens of ns time, depend on the size of the excitation ring, that can vary from 100 to 400 microns with different axicon conical angles. Heat diffusion will reach the centre of the ring later. Since water and glass have low thermal diffusivity (see Table 2.1), it takes up to ten's of ms for the heat wave to reach the centre. Thus, shock influence is not only separated in space but also in time. In case of thin films deposited on top of substrates the heat wave diffusion obviously depends on the substrate but it certainly diffuses toward the centre in a slower timescale than the acoustic waves. In case of glass or sapphire substrates, it will also require ms for the heat to diffuse away from the ring. In case of post-mortem analysis, we should also account for the heat diffusion that can influence on the final transition.

2.5 Conclusion

This chapter presented a brief overview on all types of acoustic waves that can be laser generated within the materials (longitudinal and shear, bulk waves) and at the surface of the materials (Rayleigh waves, Scholt waves, surface skimming waves etc.). A theory of the shock front formation under a shock perturbation of the material as well as a short introduction to laser acoustic wave generation method was also presented.

The speed of the different acoustic waves is the distinguishing criterium in this work. All the acoustic waves that can be generated within the material have their unique speed following:

$$v_L > v_T > v_{SAW} \tag{2.39}$$

where v_L is the longitudinal speed, $v_T$is the shear wave speed and v_{SAW} is the speed of the surface acoustic waves. This relationship is still valid in the non-linear regime where **shock wave front propagates faster than its linear counterpart.**

An experimental approach of converging shock waves generated by using an annular laser excitation was also described. Such method gives us a possibility to amplify the amplitude of the laser generated acoustic waves due to focalization and also to separate spatially laser-influenced regions from shock-influenced regions. All the types of waves that can be generated using the ring-shaped technique in all sort of samples were described at the end of this chapter.

Chapter 3

Shock wave real-time observation

'Seeing is understanding' said once Ernst Mach and till now the direct observation is the first step to understand any physical phenomena. Just looking at the object was enough for some period of history. With science development and necessity to observe the ultrafast complex phenomena especially at the micro-scale, we need to use something more powerful than a naked eye. Today we have a variety of methods that help researchers to see the dynamics of ultrafast phenomena. Till now, optical methods are the first thing to have in mind for 'visualization'. They are whole-field non-contact diagnostic methods that do not destroy sample and usually are simple to build.

This chapter presents the technical aspects of our quotidian shock experiments. The ring-shaped approach was used to generate a converging shock wave that propagates in-plane on the sample. Illumination of the sample surface with another laser pulse makes it possible to observe and image this shock wave propagation. From the images sequence we can obtain information about the speed of the generated shock waves and from the Hugoniot parameters of the material it is possible to estimate generated pressure. Post-mortem analysis of the sample gives an indication about permanent structural modifications. The last part of this chapter highlights the typical results and explains information that can be obtained with this technique.

3.1 Principle of a pump-probe experiment

Pump-probe techniques are a class of ultrafast methods for perturbing (pumping) a system with light and watching (probing) the following responses as a function of the delay time between the pump and probe pulses. The result is a sort of movie of the system evolving with time. An example of capturing dynamics is the photo series of a galloping horse and rider by a photographer Eadweard Muybridge (Figure 3.1). He performed these series in order to find out whether all horse legs left the ground during a gallop or not. Muybridge captured the horse's motion using a series of cameras in a line; each camera snapped a shot as the horse rode by. Ultrafast pump-probe measurements are usually made by the same principle. At first, a pump pulse excites the material inducing a change of state (the horse is set in motion). A probe pulse that arrives sometime after the first one, snaps the current state of the system (a single photo is taken). In this way, step-by-step, by changing the time delay between pump and probe, it is possible to reconstruct a real-time movie of the system evolution. A single snapshot acquisition results from the average of the system evolutions monitored within the duration of the probe pulse. Thus, the shorter is the pulse, the quicker is the interaction and all slower processes are observed as frozen. In this work we used a pump-probe imaging technique with a femtosecond time resolution.

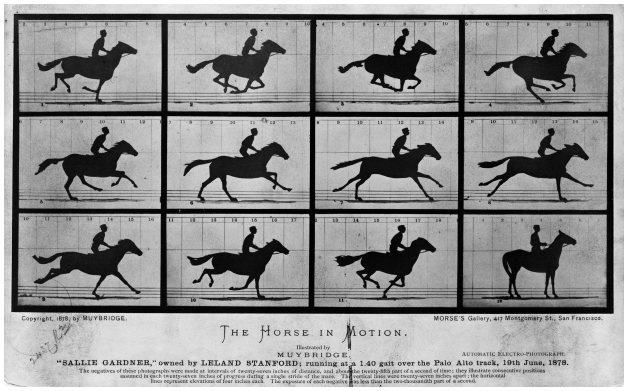

***Figure 3.1** – Series of photographs 'Sallie Gardner at a Gallop', also known as 'Horse in motion', made by Eadward Muybridge (1878).*

3.2 Experimental setup

Here we introduce all necessary parts for our all-optical single-shot time-resolved imaging setup. Schemes containing the features of pump-probe system are shown in Figures 3.2 - 3.3. The experiment has to be single-shot because shock generation process is going through the ablation which leads to permanent damage of the sample. A simple in-plane displacement of the sample allows us to go to the 'fresh' region of the sample and repeat the experiment at different conditions, such as different time delays or different pump fluences. Evolution in time was monitored by changing the delay time between pump and probe pulses. A femtosecond illumination probe pulse was used for achieving short exposure time to 'freeze' the shock wave propagation with characteristic timescale in nanosecond region. The 2D spatial images of the perturbed sample surface were recorded with a two-lens imaging system and a high-sensitive CCD camera.

Several experimental setups were developed to record images in two different configurations: transmission or reflection. The nature of the sample determines which one is used. Both configurations are easily exchangeable one to another. The difference between the two is the way the probe pulse interacts with the sample:

- in **transmission mode**, the probe pulse arrives to the sample from the opposite side to the pump pulse, going through the sample, reflects from the dichroic mirror and finally arrives to the camera (Figure 3.2(a));
- in **reflection mode**, the probe pulse comes from the same side as the pump pulse, illuminates the surface, reflects from the interface and goes to the camera (Figure 3.2(b)).

Due to this difference, the transmission mode is sensitive in depth of the sample while the reflection mode is sensitive at surfaces and interfaces.

An interferometer can be added to each setup configuration. The transmission mode can be extended with a Mach-Zender interferometer (Figure 3.3(a)), and the reflection mode - with a Mickelson interferometer (Figure 3.3(b)). Interferometry is more sensitive to density changes and surface displacements, so the shock front can be detected easier. Fringes bend when a shock wave propagates on the sample surface and the density change can be extracted from the interferograms [80].

3.2.1 Laser systems

In our experiments we used the single-shot pump-probe technique that applied two laser pulses: a pump to excite our sample and a probe to measures the optical changes delayed by a certain time from the pump. The experiments can be performed using just one laser or by synchronizing two lasers with an external trigger. Here we will present short description of each configuration.

Experiments were set with one laser, i.e one-box ultrafast laser *Solstice @ Spectra Physics*. The Solstice system consists of 4 independent blocks: a mode-locked Ti:sapphire MaiTai "seed" laser, a stretcher/compressor, a regenerative amplifier and an Empower pump laser that energizes the 'seed' pulses. The Empower is a Q-switched, frequency-doubled laser that provides the optical energy used to amplify the pulses. This laser system emits a train of pulses with a Gaussian temporal profile with a FWHM of about $150\,\mathrm{fs}$ at a repetition rate of $1\,\mathrm{kHz}$ tuned to a central wavelength of $\sim 800\,\mathrm{nm}$. This laser also can output the amplified but non-compressed pulses at $800\,\mathrm{nm}$ wavelength and $300\,\mathrm{ps}$ pulse duration with a repetition rate $1\,\mathrm{kHz}$. Shock experiment was always performed using picosecond pulse for the pump and femtosecond pulse for the probe. Delay between pulses was changed using a motorized and static optical delay line. The longest time delay that can be achieved in this case was less than $100\,\mathrm{ns}$.

To reach a longer time scale, a second laser has been inserted to the setup: a nanosecond high power *Minilite @ Continuum*. The Minilite is a Nd:YAG laser system that outputs laser pulses of $1064\,\mathrm{nm}$ wavelength and $5\,\mathrm{ns}$ with adjustable repetition rate from single shot to $15\,\mathrm{Hz}$. This laser system uses traditional flashlamp pumping and can be triggered externally. For single-shot experiment we provide a TTL pulse to the flashlamp and Q-switch which allows us to synchronize the laser output with the Solstice laser and reach a delay of more than $1\,\mu\mathrm{s}$.

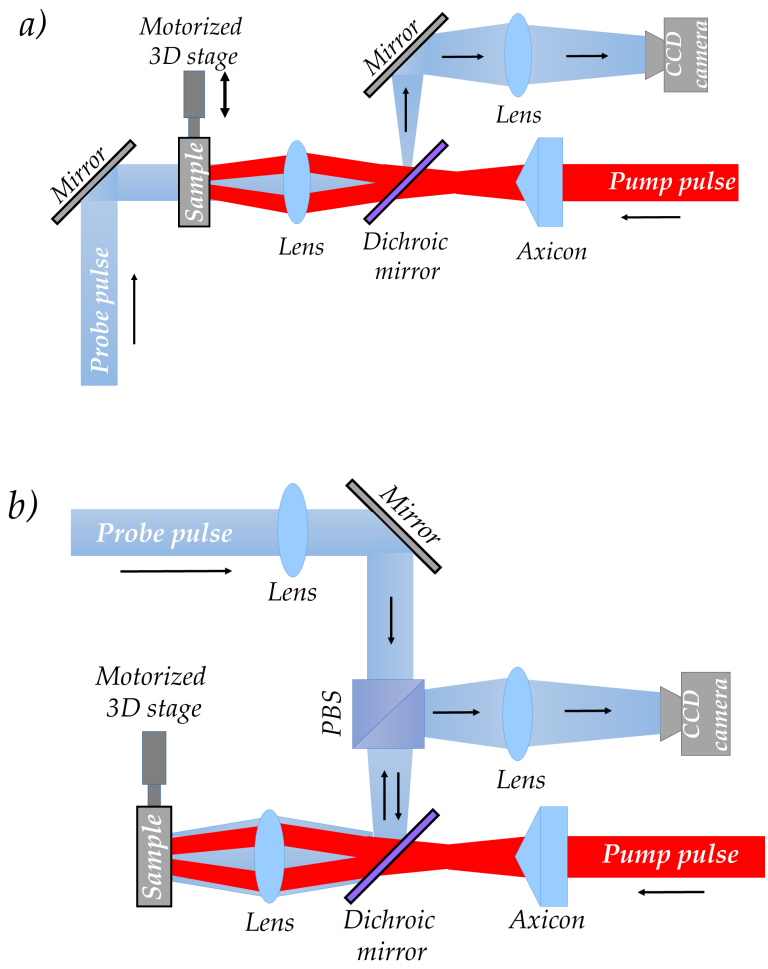

Figure 3.2 *– Scheme of the experimental setup in two configurations:* ***a***) *transmission and* ***b***) *reflection. The pump pulse goes through an Axicon, to form a ring pattern which is focalized on the sample. The probe pulse arrives from* ***a***) *the back side of the sample or* ***b***) *front side of the sample and illuminates the region of interest. After going through or reflecting from the sample surface, the probe pulse goes to the CCD camera that records a snapshot.*

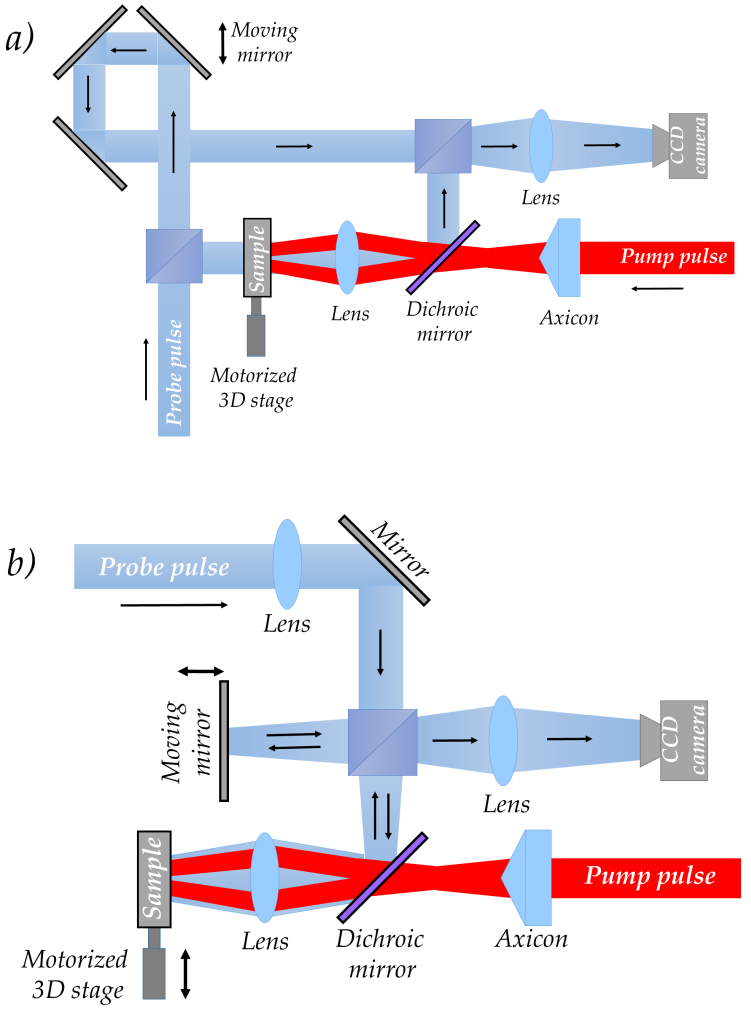

Figure 3.3 *– Schematic representation of the interferometric experimental setup in two configurations:* ***a****) transmission with Mach-Zender interferometer and* ***b****) reflection with Mickelson interferometer. The excitation pulse is shaped into a ring at the sample by using Axicon. The surface is imaged using a variably delayed probe pulse and the interferometer to obtain interferometric images of the shock propagation.*

3.2.2 Optical path for pump

The annular excitation of the shock waves was performed by shaping the pump laser pulses into a ring, using an Axicon (a conical lens) and a lens combination (Figure 3.4) that focalize a laser ring on the sample surface. Usually, we have used a $3\,\mathrm{cm}$ focal lens (AC254-030-B, Thorlabs) or two microscopic objectives (Mitutoyo M Plan Apo) with different magnifications (x10 or x20).

Laser ring size and thickness can be adjusted in two ways: a) by changing the Axicon angle α, that means changing the Axicon or b) by changing the focal length of the lens. At the sample level laser ring generates two counter-propagating shock waves: one wave is a diverging wave that will quickly attenuates and another that focalizes at the geometrical center of the laser ring where a discontinuous point will be created which, in return, generates other diverging wave. For being able to control the pump fluence a simple combination of half-waveplate and a polarized beam-splitter (PBS) was used. A motorized sample stage was used to laterally move the sample to a new undamaged position from shot to shot.

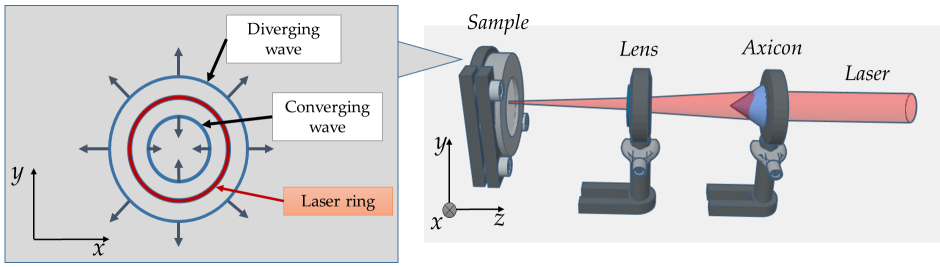

***Figure 3.4** – Schematic representation of ring-shaped pattern for the generation of a converging shock wave. The laser spot is transformed into a ring thanks to a conical lens Axicon and focalized by a $3\,\mathrm{cm}$ lens onto the sample surface. Such pattern generates two counter-propagating waves: converging and diverging.*

3.2.3 Probe part of the experiment

Optical methods for imaging can be divided into two basic techniques: shadowgraphy and interferometry.

Shadowgraphy is an optical technique which projects the shadow of an optical image onto a viewing plane for image capture. The method of collecting shadowgrams is similar to visualization of fluctuations in air density by human eyes, e.g. from the hood of an overheated car or gas rising from a barbecue grill. Shadowgraphy is the simplest visualisation technique which requires a minimum of instruments: a light source and a flat screen to project shadowgrams for observation.

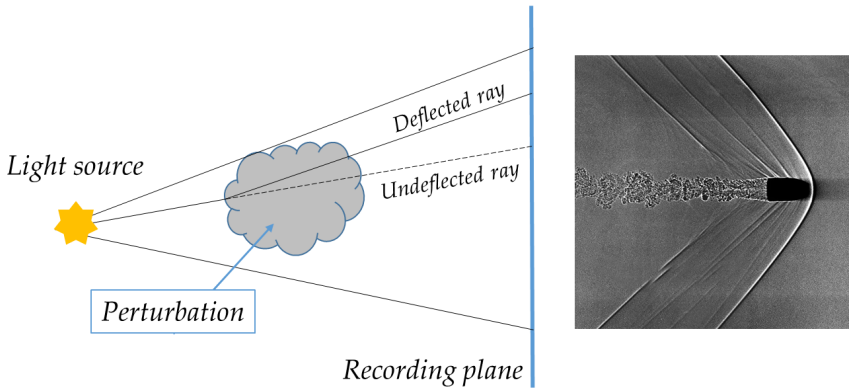

Figure 3.5 *– Schematic representation of direct shadowgraph imaging. Image represents a shadowgraph image of a fired bullet* [*81*].

Figure 3.5 shows a ray-tracing schematic of the refractions that generate the direct shadowgraph images. Shadowgraph imaging requires only a fast change of refractive index for the object, and so, it does not require a collimated imaging source. In fact, the curvature of the phase front for non-collimated imaging light typically enhances the contrast in images collected using shadowgraphy, as the curved phase front causes the light to refract further. The intensity of shadowgraphy images is proportional to second derivative of the refractive index. This technique is the standard method in ballistic testing and was used in this work for shock wave visualization.

Interferometry is a family of techniques that uses the interference phenomena to obtain information. Historically, interferences were used to study

the nature of light but soon people realised that it is also a powerful diagnostic tool. Since interferometers measure the difference in the optical path in two branches, they are widely used for measurement of small displacements, changes of refractive index and surface peculiarities. From all variety of available interferometers, in this work we used just two: Mickelson and Mach-Zender interferometers. However, all of them work with the same basic principle but vary by their technical realisation: Mach-Zender interferometer is more apropriate for visualization in transmission and Mickelson is more for observation in reflection.

Typically, one coherent light beam is splitted in two different pathways and are recombined at some point. Phase difference between two initially identical beams will create an interference pattern. The intensity of the interference pattern for the case presented in Figure 3.6, can be described as follows:

$$I(x,y) = I_1 + I_2 + 2\sqrt{I_1 I_2}cos(\Delta\phi(y)) \approx I_1 + I_2 + 2\sqrt{I_1 I_2}cos(\frac{2\pi}{\lambda}\alpha y) \quad (3.1)$$

where I_1, I_2 are the light intensities of two beams, λ is the light wavelength, α is the angle between the two optical fronts. The appearance of a supplementary phase shift in one arm of the interferometer results in a fringes deformation. L. Mach as the first visualized in 1896 the flow around supersonic flying bullet and saw the shock front on the interference pattern.

In our experiments, the probe pulse is used to illuminate the sample surface and to record a time-resolved image. Usually, as a probe pulse we used a $150\,\mathrm{fs}$, $800\,\mathrm{nm}$ pulse with frequency doubled in a birefringent $\beta - BaB_2O_4$ (BBO) non-linear crystal. Let us follow the beam path for the probe illustrated in Figure 3.2(a). The probe pulse arrives to the sample at some time delay after the pump pulse, and illuminates the pump-modified region, then it reflects from the dichroic mirror used in order to separate the pump and probe pulses of different wavelengths and goes to a camera, here Hamamatsu CCD $C9100 - 01$. The camera records images of the sample surface at a finite-time delay after the pump modification. Combination of half-waveplate and polarized beam-splitter (PBS) was used to control the intensity of a recorded image.

In case of using an interferometer (Figure 3.3), the incoming probe beam is splitted in two: one of which is going through the sample, the other one is the reference probe. Overlapping both probes again after the sample leads

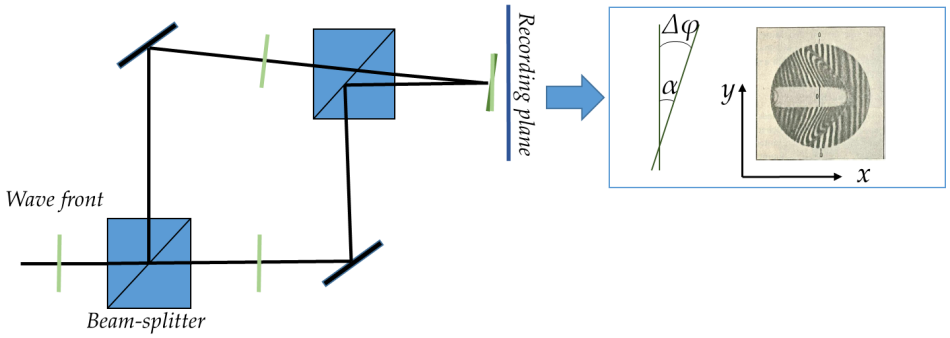

Figure 3.6 *– Principle of Mach-Zender interferometer: a light beam is split into two beams propagating their own path. Their recombination on a screen gives rise to an interference image. The interferogram is the original one recorded by L.Mach representing a travelling bullet* [82].

to an interferogram image of the sample surface. By adjusting the reference beam mirror we can tune the density of the obtained fringes.

The full shock propagation history is recorded by changing the probe time delay. This delay can be controlled in different ways, in case of using one laser system or two. A motorized linear translation stage with dual retro-reflectors mounted on it is used as a delay stage that gives us a delay of around $6\,\mathrm{ns}$. In order to obtain longer delays, we have stretched out the probe beampath by adding multiple reflections between two large mirrors separated by about $50\,\mathrm{cm}$. This simple manipulation increased the delay up to $70\,\mathrm{ns}$. The inconvenience here is that the probe pulse loses intensity and quality while it goes through this 'static' delay line. The advantage of adding a second laser is that the time delay can be controlled electronically. In this case two TTL pulses were used to trigger the flashlamp and Q-switch of Minilite laser. Another TTL pulse was used to trigger the gate mode of Solstice laser to obtain just one laser pulse on the output. The synchronization between the two laser systems was done by a time/delay generator *DG 535 @ Stanford Research system*.

3.3 Sample cell assembly

In this section we present different sample assemblies, depending on whether the samples is liquid or solid. In both cases, the sample is maintained vertically by a sample holder respectively mounted to a 3D stage. This allows us to move the sample after each laser shot unperturbed.

3.3.1 Liquid sample construction

All experiments with liquid samples were performed in transmission mode. Schematic representation of the sample is shown in Figure 3.7 (a). A thin liquid layer is sandwiched between two glass substrates. All of them have a ring shape. The thickness of the liquid layer depends on the used spacer thickness and the inner ring radius regulates the volume of the liquid that can be used. Figure 3.7 (b) shows a liquid sample of distilled water doped with carbon nanoparticles.

We used different types of spacers:

- aluminium foil ($20\,\mu m$),
- deposited polymer ($10\,\mu m$),
- parafilm ($17\,\mu m$).

The laser beam shaped into a ring pattern is focused directly into the

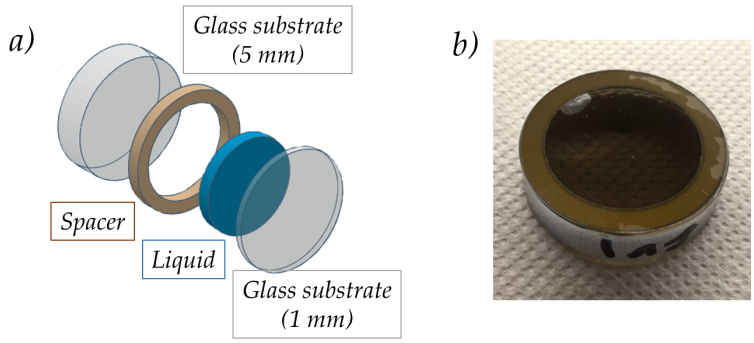

***Figure 3.7** – Liquid sample: **a**) Schematic illustration of the sample geometry - the liquid of interest is sandwiched between two glass substrates with a spacer; **b**) Prepared sample of carbon nanoparticles from ink diluted in distilled water with transducer ring as a spacer.*

liquid layer from the thinner substrate side. The laser beam is absorbed by the liquid and gives rise to two shock waves which propagate laterally within the liquid. The inward-propagating wave converges at the center and the outward-propagating wave diverges and decreases in amplitude. The shock confinement in the liquid was ensured by relatively large impedance mismatch between the liquid and the solid glass substrates (Z_{water} $= 1.45\,\mathrm{Pa}\cdot\mathrm{s/m}$ and $Z_{glass} = 11.3\,\mathrm{Pa}\cdot\mathrm{s/m}$).

3.3.2 Solid sample mount

Solid samples were most often studied in the reflection mode. For the solid sample, we are looking at the surface waves propagation. This kind of samples were mounted in a specially designed metallic mount (see Figure 3.8) which requires a square formed sample. We have a different sample shapes that cannot fit the mount, therefore we simply glued the sample to a glass substrate (BK7, diameter of $25\,\mathrm{mm}$) with a piece of double-face tape (3MC Scotch Brand).

***Figure 3.8** – Holder for the solid sample.*

3.4 Laser induced acoustic waves

Table 3.1 illustrates the types of acoustic waves that we have observed in the different categories of sample structures. By measuring experimentally the speed of the generated wave, we can assign the nature of the acoustic wave that is measured. If the measured speed v_m is equivalent to the longitudinal speed of sound (in case of a liquid layer) or to the speed of surface acoustic waves (in case of solid samples), we are dealing with a linear acoustic wave and the Rankine-Hugoniot relations cannot be used. The non-linear case i.e. shock wave regime, appears when the measured speed exceeds the corresponding linear acoustic velocity. In this case, the Hugoniot relations can be used, even in the case of cylindrical waves, at a position far from the focal point. In the specific case of solid samples and non-linear surface acoustic waves that includes formation of a shock front along the interface the Hugoniot cannot be used.

***Table 3.1** – Sample type vs observed acoustic waves*

Sample	Measured speed v_m	Type of wave	Hugoniot
Liquid layer	$v_m = v_L$	Longitudinal wave	-
	$v_m > v_L$	Cylindrical shock wave	+
Solid	$v_m = v_{SAW}$	linear SAW	-
	$v_m > v_{SAW}$	Non-linear SAW	-

3.5 Propagation of a converging acoustic wave

This section is just the illustration of typical results that can be obtained by the shock visualization technique set up by me in Le Mans.

3.5.1 Cylindrical acoustic waves in water

Linear acoustic waves.

Shock experiments were performed on distilled water with absorbing suspended carbon nanoparticles made from ink (Tusche a drawing ink, Pelikan, black) diluted 10x. The sample was assembled in a layered configuration, described above. The sample consisted of a $200\,\mu\mathrm{m}$ thick liquid layer

sandwiched between two glass substrates. The laser pulse was absorbed by carbon nanoparticles (ink) that undergo photoreactive energy release and vaporization to generate high pressure. The impedance mismatch between the windows and the water sample confines a shock wave laterally in the sample plane. Knowing the speed of this wave we can clearly distinguish this bulk shock wave from the other non-linear waves in the substrates or at the interfaces.

Experiments were performed in transmission mode using $300\,\mathrm{ps}$ pulse duration, $800\,\mathrm{nm}$ wavelength as a pump and $150\,\mathrm{fs}$ pulse duration, $400\,\mathrm{nm}$ wavelength as a probe (both taken from Solstice laser system). To form a laser ring, 0.5^o Axicon (Doric Lenses, Inc.) and a microscopic objective x10 (Mitutoyo M Plan Apo) were used. Width of the formed laser ring was $10\,\mu\mathrm{m}$ and the diameter was $85\,\mu\mathrm{m}$. Figure 3.9(a) shows propagation of the acoustic wave from excitation laser ring to the acoustic focus. The converging wave focalizes in the center within $59\,\mathrm{ns}$ for $0.06\,\mathrm{mJ}$ excitation pulse. From these images we can estimate the average shock speed of the generated shock wave. The speed of the cylindrical shock wave is almost constant along the ring radius and only change at the very close point to the ring center that was predicted mathematically in [83–85] and observed experimentally in [86]. As shown in Figure 3.9(b) the average speed of the shock wave at this fluence is $1.45\,\mathrm{km/s}$, that matches the longitudinal speed

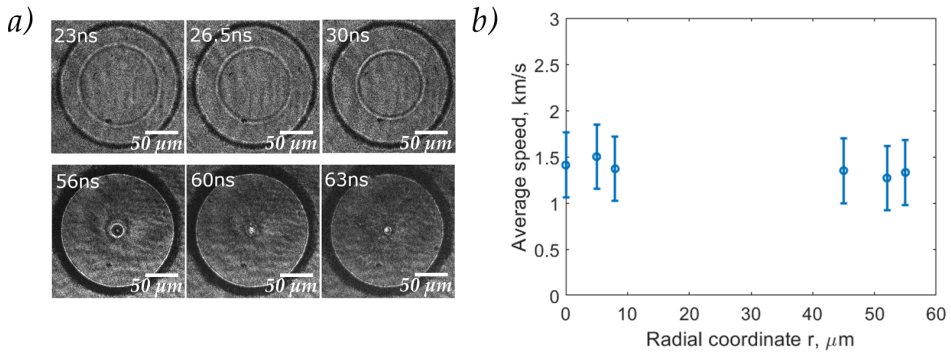

Figure 3.9 *– Shock waves in water:* ***a****) Single-shot frames recorded for an excitation pulse of* $0.06\,\mathrm{mJ}$*,* $300\,\mathrm{ps}$ *and a laser ring of* $85\,\mu\mathrm{m}$ *radius;* ***b****) Converging shock speed vs distance from the acoustic focus.*

of sound. Error bars includes error for time measurement ($\Delta t = \pm 5\,\mathrm{ns}$) and error for length measurement ($\Delta l = \pm 5\,\mu\mathrm{m}$). Repeated measurements with the same time delay showed no significant variation of shock wave speed. At this low laser fluence we get a linear acoustic wave.

Shock waves.

The same experiments were performed using $5\,\mathrm{ns}$, $1064\,\mathrm{nm}$ laser pulse as a pump, coming from the Minilite laser system. The 0.5^o Axicon and a $3\,\mathrm{cm}$ lens were used to form the laser ring with a width $10\,\mu\mathrm{m}$ and a diameter $350\,\mu\mathrm{m}$. Figure 3.10 shows the time history of converging shock wave, that focalizes at the ring center in $85\,\mathrm{ns}$. Laser fluence was $1.5\,\mathrm{mJ}$.

At about $45\,\mathrm{ns}$ delay after shock focalization we observe the on-set of bubble cavitation and growth (dark spot at the center), while the inner shock diverges toward the annular laser-induced bubble cloud. It comes from the tensile part of the bipolar shock pulse appearing after focalization [68]. The following frames show the appearance and evolution of a nucleated secondary bubble cloud due to the inner shock being reflected at the annular laser-induced bubble. Finally, the secondary bubbles disappear within a few hundreds of nanoseconds whereas the central bubble collapses in a timescale longer than $1\,\mu\mathrm{s}$ which is correlated with results

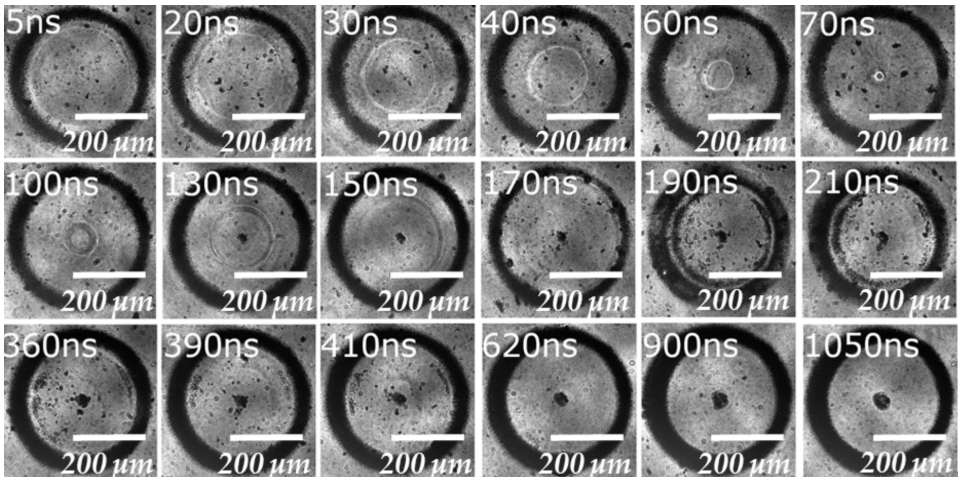

Figure 3.10 – *Single-shot frames recorded for an excitation pulse of* $1.5\,\mathrm{mJ}$, $5\,\mathrm{ns}$ *and a laser ring of* $175\,\mu\mathrm{m}$ *in radius.*

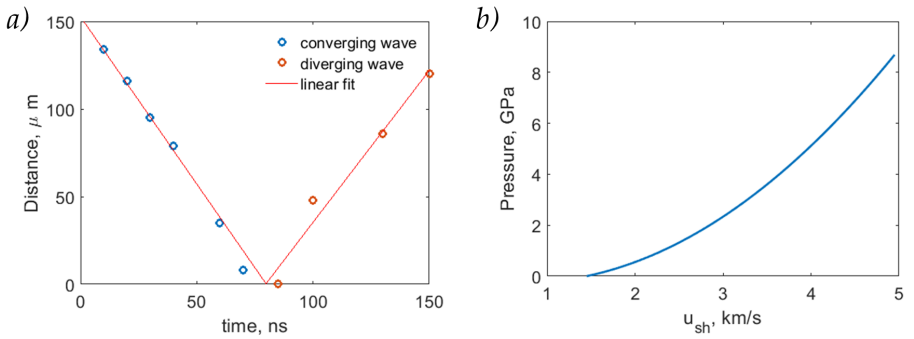

Figure 3.11 *– a) Dependence of the inner shock wave position from the ring center on time delay; b) Hugoniot data for water [87].*

observed in [68].

Figure 3.11(a) represents the shock wave position from center versus time delay extracted from snapshots in Figure 3.10. By fitting this data with linear approximation we can get the speed for inner converging shock wave $1.92\,\mathrm{km/s}$ and inner diverging shock wave $1.73\,\mathrm{km/s}$. This method gives us a reliable estimation of the shock wave speed with the error bar of $\pm 0.3\,\mathrm{km/s}$ but don't allow us to explain the difference in shock wave speed for converging wave (before focus) and diverging one (after focus).

The shock wave peak pressure P in water is related to the propagation speed u_{sh} through the equation of state and is calculated using the Hugoniot data from the literature [87]:

$$P = \rho_0 u_{sh} \frac{u_{sh} - c_0}{1.99} \tag{3.2}$$

where u_{sh} is the shock speed, c_0 is the acoustic velocity in water $(1.45\,\mathrm{km/s})$ and ρ_0 is density of the undisturbed water at room temperature ($0.998\,\mathrm{g/cm^3}$). This dependence is presented in Figure 3.11(b) and the estimated average pressure for the two experiments can be found in Table 3.2. The shock wave speed as well as shock wave pressure increase from an increase of the excitation fluence. Pezeril et al. [86] showed dependence of shock speed and pressure as a function of pump pulse energy.

Here we have an opportunity to compare shock wave excitation with two different laser wavelengths and pulse durations. The duration of the

Table 3.2 *– Shock wave generated pressure for two different pump powers*

Pulse duration	Pump fluence	Shock speed	Peak power
300 ps	0.06 mJ	1.45 km/s	7.32 MPa
5 ns	1.5 mJ	1.9 km/s	0.42 GPa

excitation pulse determines the regime of ablation and creation of plasma at the laser ring region, as it was mentioned in section 2.3.1, this is out of scope in the frame of this work.

Sample will have different optical properties at two wavelengths that were used in this work for excitation. Figure 3.12(a) shows transmission spectra for fused silica glass (5 mm thick substrate) and BK7 glass (1 mm thick substrate). As we can see, glass properties remains the same at both wavelengths - high transmission of about 90 % observed for both types of glass. Water, instead, has a variation in transmission (Figure3.12(b)) of about 10 % between 800 nm and 1064 nm. But on top of all that, the particles of black carbon (CB) made from India ink has the lowest transmission for both excitation wavelengths that leads to a dominant absorption of the laser pulse. The main reason of adding ink into water was to increase the efficiency of laser pulse absorption that leads to increasing in efficiency of shock wave generation.

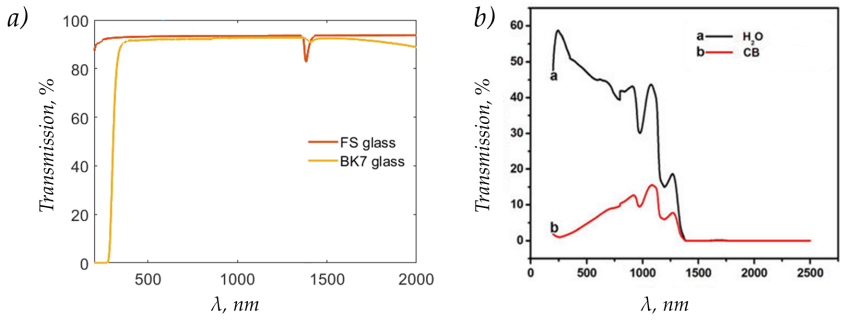

Figure 3.12 *– Transmission spectres: a) fused silica glass (one of substrates) [88] and BK7 glass window (another substrate) [89]; b) water and Carbon Black (CB) nanoparticles made from ink [90].*

3.5.2 Shock wave propagation in ethanol

The very same experiments were performed on another well known liquid: ethanol. The sample configuration was the same as in previous case: $200\,\mu\mathrm{m}$ thick ethanol layer doped with suspended absorbing carbon nanoparticles made from ink (Tusche a drawing ink, Pelikan, black) diluted 10x and sandwiched between two glass substrates. Imaging experiment were performed in transmission mode with using $5\,\mathrm{ns}$ pulse of $1064\,\mathrm{nm}$ wavelength as pump and $150\,\mathrm{fs}$ pulse of $400\,\mathrm{nm}$ wavelength duration as probe pulse. Laser ring diameter in this case was $175\,\mu\mathrm{m}$ with $10\,\mu\mathrm{m}$.

Figure 3.13 shows the time history of the converging shock in thin ethanol layer. The inner shock wave focalizes at the ring center in $110\,\mathrm{ns}$ which gives us an average shock speed of about $1.6\,\mathrm{km/s}$. After converging at the ring center, shock wave reflects and diverges towards the excitation laser ring. At a delay longer than $140\,\mathrm{ns}$ we observe a multibubble cavitation at the center of the ring (dark region). Further delays show a secondary bubble cloud appearing and disappearing after hundreds of nanoseconds. The central bubble cloud stays longer than $1\,\mathrm{ms}$. The creation of a wider secondary bubble region and slightly longer lifetime in comparison to the water case,

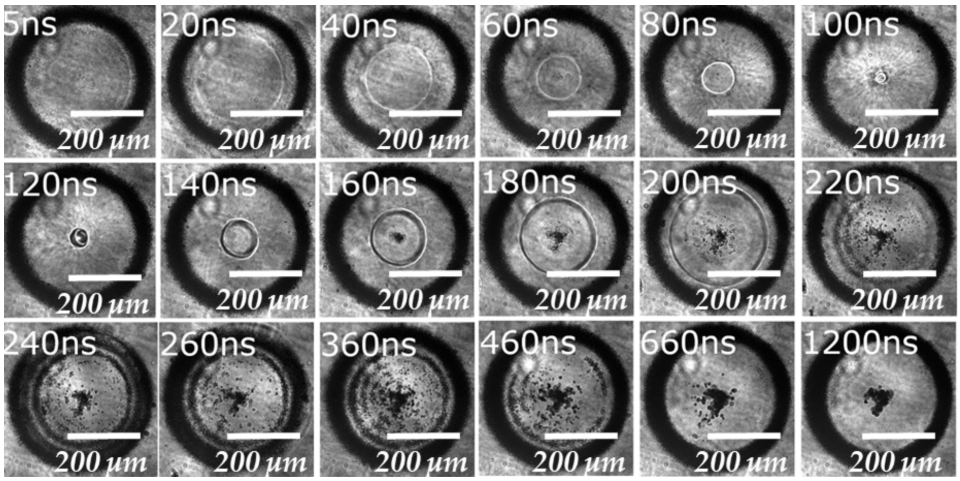

Figure 3.13 – *Single-shot frames recorded for an excitation pulse of* $1.5\,\mathrm{mJ}$ *and a laser ring of* $175\,\mu\mathrm{m}$ *radius.*

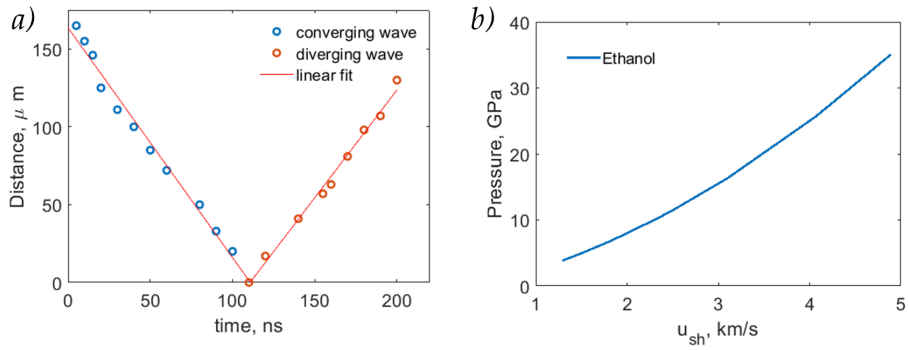

***Figure 3.14 – a**) Dependence of the inner shock wave position from the ring center on time delay; **b**) Hugoniot data for pure Ethanol* [91].

are clearly observed.

The shock wave position from center versus time delay is shown in Figure 3.14(a). Linear fit of this data gives us the average speed for inner converging shock wave $1.54\,\mathrm{km/s}$ and inner diverging shock wave $1.35\,\mathrm{km/s}$. This method gives us a reliable estimation of the shock wave speed. The shock wave peak pressure P is related to the propagation speed u_{sh} through the equation of state and can be estimate using the Hugoniot data found in literature [91] and shown in Figure 3.14(b). For the $1.8\,\mathrm{J/cm^2}$ pump fluence we generate a shock wave with an average speed $u_{sh} = 1.54\,\mathrm{km/s}$ when the speed of sound in ethanol is of $c_0 = 1.14\,\mathrm{km/s}$. This shock speed corresponds to $P \sim 5\,\mathrm{GPa}$ of generated shock pressure.

3.5.3 SAW induced failure in glass

Converging shock waves can be used for studying material damage, fractures, cracks under dynamic pressure. Recently, Veysset et al. [92] observed material failure from gold-coated glass substrates upon surface acoustic wave focusing using the same method os generation. They demonstrated that the focus of SAWs results in the gold layer delamination from the glass substrate and the fraction at the center. At higher laser excitation energies the damage was extended to the glass substrate and more dramatic breakdown of glass at the center was observed. In addition to the crack for-

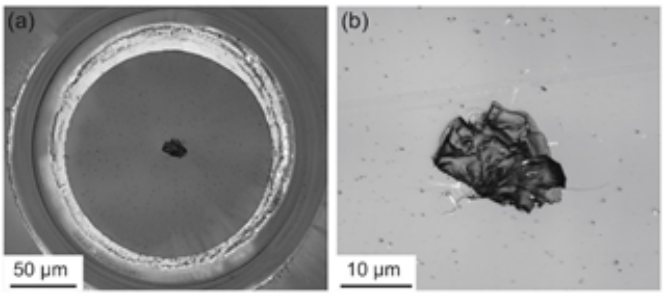

Figure 3.15 – *Laser-scanning confocal microscope images of typical glass damage for a laser energy of* $1\,\mathrm{mJ}$. ***a***) *Large view showing excitation location, parts of remaining gold film, and central crack.* ***b***) *Zoomed-in image of the central damage*[*94*].

mation, the entire gold film initially present inside the excitation ring was removed from the substrate. In order to clarify the result of crack formation on glass, we made the same experiment with shock wave propagating on a bare glass substrate.

This part was done in Le Mans in collaboration with D. Veysset and S. Kooi (Keith Nelson group, Massachusetts Institute of Technology). Sample consisted of a $300\,\mu\mathrm{m}$ - thick borosilicate glass substrate (D263 Schott) with a $160\,\mathrm{nm}$-thick metallic ring. This metallic ring, so-called gold ring, consisted of $10\,\mathrm{nm}$ chromium, in contact with the glass, and $150\,\mathrm{nm}$-nm gold. The gold ring had a diameter of $200\,\mu\mathrm{m}$ and $80\,\mu\mathrm{m}$ width. The laser focus was shaped as a $200\,\mu\mathrm{m}$ - diameter, $5\,\mu\mathrm{m}$ - waist ring using a 0.5^o Axicon and a $3\,\mathrm{cm}$ focal-length lens. The sample was positioned so that the laser focus and the gold ring were overlapped before each experiment. The experiments were performed in reflection mode with an Michelson interferometer and with using $300\,\mathrm{ps}$ pulse of $800\,\mathrm{nm}$ wavelength as pump and $150\,\mathrm{fs}$ pulse of $400\,\mathrm{nm}$ wavelength duration as probe pulse. The fringe density was adjusted to be about $200\,\mathrm{fringes/mm}$ by tilting the reference mirror. The Michelson interferometer was added in order to perform density measurements [93].

Contrary to the experiments on gold layer deposited on glass substrates [92] where large amplitude of SAWs at the focus caused delamination and damage of the film at low laser energy ($\sim 0.1\,\mathrm{mJ}$) and glass substrate frac-

ture at high laser energy ($\sim 2\,\mathrm{mJ}$), in our case of a gold rings we could observe surface displacements even at high laser energies and, after post-mortem sample examination, we could confirm glass fracture at laser energies above $0.75\,\mathrm{mJ}$. Film damage did not obscure the imaging of the SAW at higher laser energies enabling the evaluation of the absolute surface displacements leading to glass fracture.

Figure 3.15 shows an example of the damage observed at the center of the ring at $1\,\mathrm{mJ}$ laser energy. Laser-scanning confocal microscope indicates damage of about $15 - 20\,\mu\mathrm{m}$ in diameter and about $5\,\mu\mathrm{m}$ in depth. For all studied energies, no damage observed between the laser excitation area and the central crack. More details and numerical simulation, can be obtained in [94] (see Annexes).

3.6 Conclusion

This chapter describes a method for generating converging shock waves and investigating the behaviour of material under dynamic pressure. These methods confirm our ability to investigate behaviour of material under conditions far from equilibrium. This methodology can be an alternative tool for testing material strength and film adhesion.

From images sequence of shock wave propagation we can easily estimate a generated shock speed and, if the equation of states for the material of interest is known, estimate the pressure. Therefore, we can control shock pressure and direct the pressure on the sample where it can be applied.

Experimental setup can be easily modified from reflection to transmission mode, allows studying different types of samples (liquids and solids). Converging shock wave propagation in liquid leads to cavitation and generation of additional bubble clouds. In solid samples, shock wave propagation leads to a permanent damage of the sample, not only at laser ring region, but also at the acoustic focal point, *i.e.* at the center of the ring, especially at pump energies higher than $1\,\mathrm{mJ}$. At this energy a cracks on a glass were observed.

Further chapters will present results of laser induced shock waves in materials showing phase transitions with significant volume change in order to see if a single dynamic pressure pulse can drive a phase transition.

Chapter 4

Spin crossover phase transition

4.1 Spin crossover transition

This chapter is devoted to shock wave propagation, and whether it can drive spin transition, in iron-based spin crossover materials. The spin crossover (SCO) is a phenomenon when a spin state changes due to external stimuli. This occurs usually in complexes that consist of a metal ion and organic ligands. Such compounds are prototypes of molecular bi-stability in the solid state. Changes in the spin state trigger changes of the molecular structure (bond length, angle) and consequently, cause changes of other macroscopic physical properties like volume, color, *etc*.

Lets take Fe^{II} compounds as an example. The free ion Fe^{II} has an electronic configuration d^6. Being placed in an environment of octahedral symmetry (O_h), the degeneration of its five *d*-orbitals is raised to form levels of lower energy (t_{2g}) gathering three orbitals and of higher energy (e_g) gathering the other two orbitals. The energy difference between these two levels is determined by the strength of the ligand field and denoted as $10Dq$. The six electrons can then be divided in two different ways (Figure 4.1). If the ligand field is strong, the six electrons stay in the t_{2g} orbitals and the resultant electronic spin is then zero (diamagnetic state). The electronic repulsion linked to the presence of two electrons in the same orbital is less than the separation energy of orbitals t_{2g} and e_g. The rule of Hund is not respected and this is the case of the Low Spin (LS) state (S=0). In a weak ligand field configuration, the electrons occupy the *d*-orbitals fol-

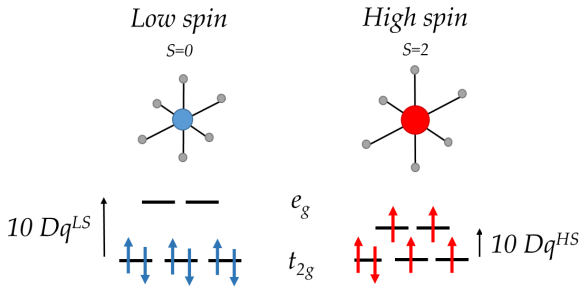

Figure 4.1 *– Representation of two spin states of ion Fe^{II}.*

lowing Hund's rule. Therefore, there are four single electrons, the resulting electronic spin is S = 2 (paramagnetic state) and this is the High Spin (HS) state. In that case, the anti-bonding orbitals are occupied; thus causing elongation of the Fe - ligand distances in comparison to the LS state. In addition to the bond elongations other structural aspects, such as angular distortions, can be involved during the transition. Such changes of molecular geometry lead to the change of lattice cell parameters. New cell parameters are of higher values and explain the occurrence of crystal expansion. The typical values for Fe^{II} system are $5\,\%$ increase of unit cell volume and $10\,\%$ increase of the bond length. For Fe^{III} compounds these values are smaller but still present [95].

The equilibrium state of the material is determined by the free energy, G, which must take the lowest value. The potential energy form is complex in the case of solid-state materials. There may exist numerous minimas of local free energy that allow in certain cases, occurrence of different macroscopic phases with completely different structural and electronic orders. This leads us to the concept of multi-stability where solid-solid phase transformation exist in the same compound. Various materials exhibit transition between two phases with completely different physical properties like para- to ferromagnetic or insulator-to-metal transitions. By triggering the transition in such systems with an external stimuli we are able to control physical properties of the material in question.

The notion of spin transition has been introduced after a number of experiments that appeared firstly as surprising. In 1931, Cambi showed for the first time an abnormal magnetic behaviour during his study of a series of

$Fe(III)$ compounds with dithiocarbamate as a ligand [96]. Subsequently, in 1956, the notion of spin equilibrium is evoked for the first time in a compound of ferrihemoglobin hydroxide [97]. In 1964, Baker and Bobonich demonstrated the first spin transition of the $Fe(II)$ ion in the solid state for the $[Fe(Phen)_2(NCS)_2]$ compound [98]. The fundamentals and applications of SCO complexes have attracted growing interest in a wide range of relevant research fields. In 2013 two comprehensive reviews on SCO were published: a book edited by Halcrow [99] and a review by Gülich and coworkers [100]. Moreover, a large number of reviews on specific subjects relating to SCO complexes have been published to date.

Possibility to control numerous physical properties of SCO systems by light is one of the topical issues of field of *Photo-induced phase transition* (PIPT). Firstly, the term PIPT was used to describe the appearance of a macroscopic domains formed after relaxation of the optically excited state [101]. These domain have a structural order different from the initial ones. In 80's researchers observed short-lived molecules in their HS states generated by light excitation of the Fe^{III} complexes in solution [102]. The same year, Decurtins et al. [103] discovered that the SCO complex $[Fe(ptz)_6](BF_4)_2$ (ptz is 1- propyltetrazzole) exhibits light-induced HS to LS relaxation and is named as *Light Induced Excited Spin State Trapping* (LIESST). But once the irradiation is stopped, system goes back to its thermal equilibrium. At the solid state, the ultrafast LIESST dynamics were studied mostly for Fe^{III}-based SCO compounds using femtosecond optical spectroscopy [104–107]. The idea behind PIPT in spin crossover materials is to reach a false ground state on the potential energy surface. If this state has potential energy barrier high enough to trap the excited state for relatively long time (several days), this state can be treated as metastable and can represent different lattice structure compared to original one.

It is extremely important to study if the structural feedback during a solid deformation has the ability to amplify and stabilize photoinduced transformations. Recently, Bertoni et al., [108] demonstrated a cooperative self-amplified feedback in SCO material during its delayed volume expansion. Authors used a time-resolved optical spectroscopy to study $[Fe^{III}(3-MeO-SalEen)_2]PF_6$ compound that exhibits a $3\,\%$ of crystal volume expansion during the thermal transition from LS to HS state.

Figure 4.2 (a) shows a time evolution of high spin state fraction X_{HS} af-

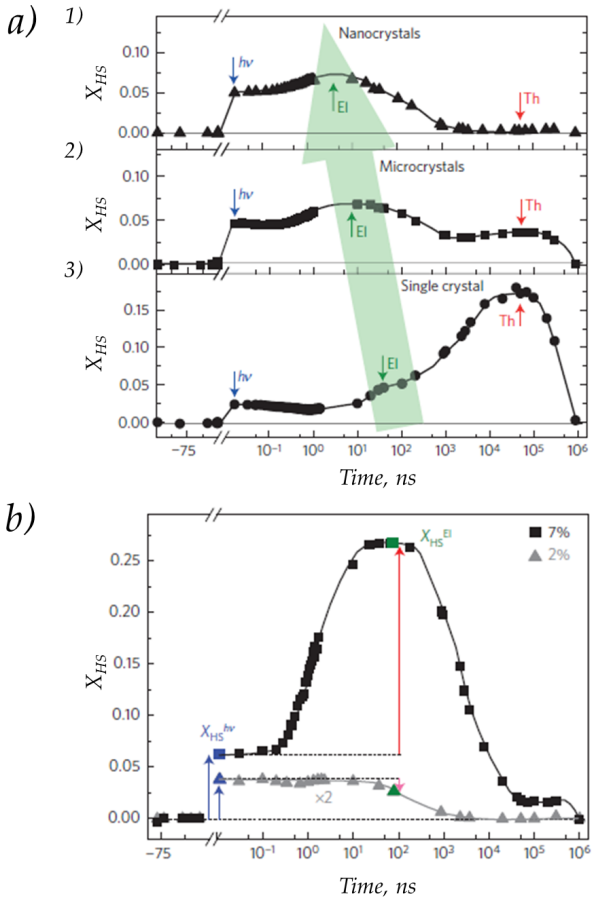

Figure 4.2 *– Femtosecond laser induced response of spin crossover crystals in LS state:* ***a****) high spin fraction* X_{HS} *of* (1) *nanocrystals,* (2) *microcrystals and* (3) *a single crystal. Photoinduced* $h\nu$*, elastic El and thermal Th steps are indicated by blue, green and red arrows. The big green arrow highlights the shift of the elastic step toward shorter times with respect to the sample size;* ***b****) time evolution of photoinduced* X_{HS} *due to two different excitations* (*blue arrows*)*. Relaxation* (*pink arrow*) *was observed for low energy of excitation* (2 %*, grey, scaled by a factor of two*) *and amplification* (*red arrow*) *- for high excitation energy* (7 % *, black*) [*108*].

ter a laser excitation in three types of samples: single crystal, microcrystals and nano-crystals. Three steps can be identified for the evolution of X_{HS}:

- *photoinduced step* $(h\nu)$ is related to local switching of molecules from LS to HS with laser excitation. It is accompanied by a molecular swelling within hundreds of femtoseconds and is indicated by blue arrows;
- *elastic step* (El), a second increase of the HS fraction on the nanosecond timescale - green arrows in Figure 4.2, associated with the establishment of mechanical equilibrium with the environment;
- *thermal step* (Th) indicated by red arrows in Figure 4.2 and accompanied by energy redistribution leading to a global temperature rise in the crystal: the HS population thermally equilibrates at X_{HS} level.

Micro- and nano-crystals were dispersed in polyvinylpyrrolidone (PVP) and sufficient heat transfer from crystals to polymer explains decreasing of X_{HS}^{Th} with sample size reduction. Thermal step position in time is defined by energy barrier between LS and HS spin states and does not depend on sample size.

Elastic step position depends on the crystal size and takes 1-2 orders of magnitude faster to populate X_{HS} in nanocrystal than in single crystal. This corresponds to the propagation of an elastic wave over typical crystal dimensions. Time evolution of X_{HS}^{El} generated with different excitation densities (Figure 4.2 (b)) shows that the elastic step appears above a certain threshold - approximately $3.5\,\%$ of photo-induced molecules. X_{HS}^{El} increases by $20\,\%$ during the elastic step at higher excitation which is the confirmation of non-linear character of the process.

Bertoni et al. [108] proposed a mechanism that can explain non-linear behaviour of elastic step in spin crossover material - see Figure 4.3. During photo-excitation some molecules are switched from LS to HS state. Molecules in HS state have bigger volume thus they provoke lattice expansion and at the same time are pushed back by surrounded LS lattice. Then, the evolution depends on the number of switched molecules: when the $X_{HS}^{h\nu}$ is small, HS molecules relax back to LS state in less than $1\,\mu s$ (Figure 4.3 (a)). When the $X_{HS}^{h\nu}$ is big enough, lattice expansion establishes new mechanical equilibrium and pulls LS molecules to HS state quicker than the relaxation of the latter (Figure 4.3 (b)). This triggers feedback mechanism : the more molecules switch, the more volume expands, and so on. *i.e.* non-linear response after photo-excitation.

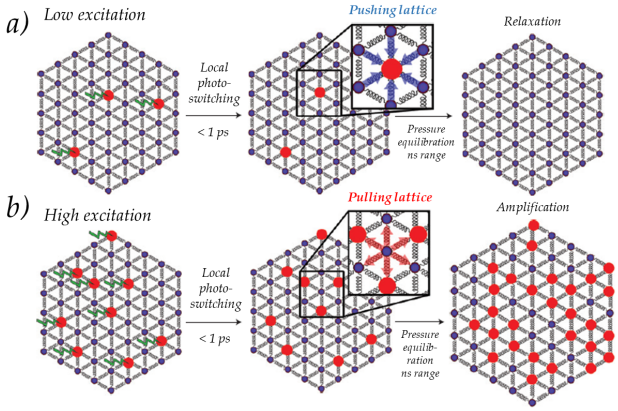

Figure 4.3 *– Scheme of the switching mechanism proposed by Bertoni et al. [108]:* ***a****) at low excitation energy, a few HS molecules (red), that were photo-switched, relax back to the LS state (blue) due to the pushing lattice forces (blue arrows on inset);* ***b****) high excitation energy provoke lattice expansion that pulls LS molecules (red arrows on inset) to cooperatively switch to the HS state (red) with higher molecular volume.*

Recently developed mechanoelastic model [109–111] confirms the proposed mechanism. Elastic interactions in this ball-and-spring model result from lattice distortions that occur because of volume difference between molecule in LS and HS states. The key role of the concept is played by pushing/pulling forces between LS and HS molecules. With the increase of switched molecules, pulling forces applied to LS molecules also increase; this denotes the non-linear response to photo-excitation. The response from simultaneous absorption predominates over a sum of individual responses from molecules that points to cooperative effects induced by laser.

Appearance of the elastic step at a time corresponding to the propagation of a strain wave over the crystal size makes the elastic wave a key point in understanding cooperative effect. In the following sections, we aim to launch elastic waves directly into the SCO crystals and investigate whether PIPT can be thus achieved. To our knowledge, only static pressure studies have been so far carried on SCO materials, hence the attempt to drive SCO with dynamical pressure on ns timescales in nano-crystalline material remains interesting.

4.2 $[Fe(NH_2 - trz)_3](Br)_2$ compound

$[Fe(NH_2 - trz)_3](Br)_2$ (with NH_2 - trz = 4-amino-1,2,4-triazole) [112] is a spin crossover compound with bi-stability close to room temperature. Figure 4.4 illustrates measured by Fouché et al. magnetic susceptibility and diffusive reflectivity of polycrystalline powder with average crystals size of ~ 1 μm [113].Two experiments indicate a thermal hysteresis loop at around $305\,\mathrm{K}$ $(32\,^{\circ}\mathrm{C})$ and of about $15\,\mathrm{K}$ $(15\,^{\circ}\mathrm{C})$ width. It was shown that when the sample undergoes Low Spin → High Spin phase transition, its diffuse reflectivity increases.

Authors in [113] also reported a photo-induced phase transition for this compound induced by nanosecond laser pulse ($\lambda = 400\,\mathrm{nm}$). Figure 4.4(c) displays image of the sample in its Low Spin (pink) and High Spin (white) states respectively. The second image in Figure 4.4(c) shows the state of the

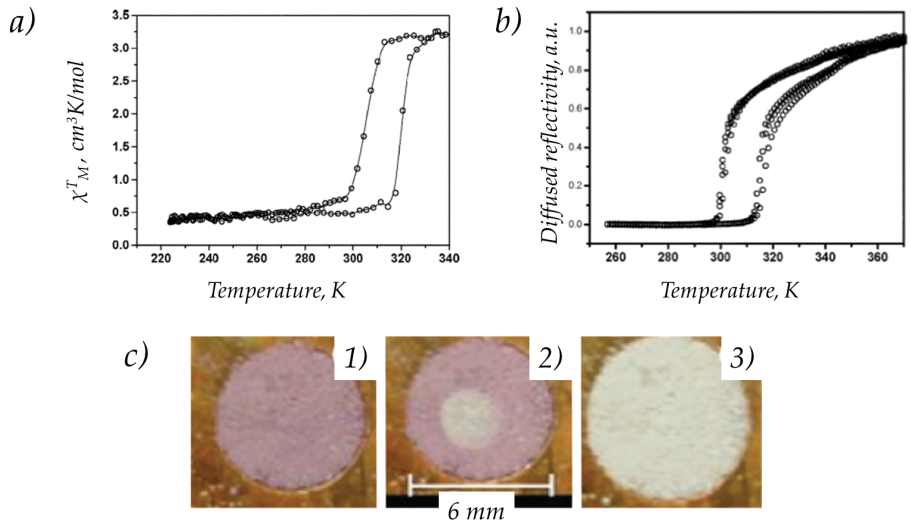

Figure 4.4 *– Experimental plots of temperature dependence of* (***a***) *magnetic susceptibility and* (***b***) *diffused reflectivity on the polycrystalline powder; and* ***c***) *pictures of the sample* ***1***) *in the LS state,* ***2***) *in the LS after photo-excitation by a laser pulse that brings the system in the HS state, as well,* ***3***) *in the HS state* [113].

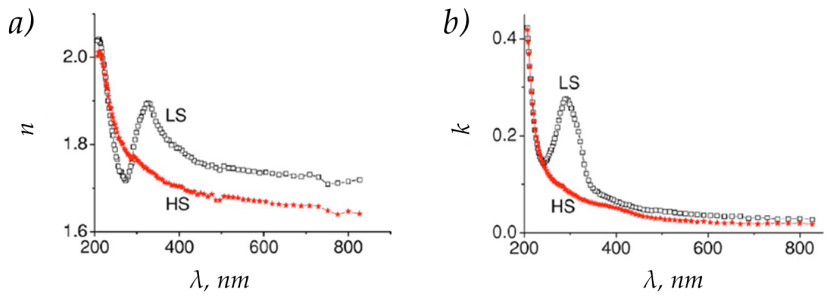

Figure 4.5 *– Extracted wavelength dependence of n* (***a***) *and k* (***b***) *in the HS state* $(at\ 353K)$ *and in the LS state at* $(263K)$ $[114]$. *An absorption band in UV spectral range is presented for Low Spin state and totally gone in High Spin state.*

sample at $36\,^{\circ}\mathrm{C}$ within its hysteresis loop when it is excited by a single pulse at $400\,\mathrm{nm}$ with a pump fluence $\sim 5\,\mathrm{mJ/cm^2}$. It was demonstrated that the part of the sample impacted by the laser pulse becomes whiter. The sample remains in this configuration as long as its temperature is kept within the hysteresis loop and recovers its original pink color once cooled down to $10\,^{\circ}\mathrm{C}$. This indicates that within the hysteresis loop, microcrystallites excited by the laser pulse are switched to the HS state.

The optical properties of this compound were measured by a spectrometric ellipsometry on a pellet in the HS and LS states by Loutete-Dangui et al. [114]. The extracted dispersion coefficient **n** and absorption **k** are shown in Figure 4.5. In the LS state, the sample exhibits a pronounced absorption band centred at $300\,\mathrm{nm}$ that disappears in the HS state. This absorption band has been assigned to the metal–ligand charge transfer transition (MLCT). In the visible spectral range, irrespective of the spin state of the compound, optical properties vary smoothly [114].

In our studies we used $[Fe(NH_2 - trz)_3](Br)_2$ nanoparticles with an average size of $\sim 50\,\mathrm{nm}$ that we provided by research group 'Molécules et matériaux commutables' from Institut de Chimie de la Matière Condensée de Bordeaux. These nanoparticles are relatively stable in ethanol; according to visual tests, they are stable for two weeks. Therefore we have used a suspension of these nanoparticles in ethanol in sandwiched sample configuration (as explained in Chapter 3).

The converging shock wave, described in section 2.3.2, undergoes a profile change while propagating: the initially unipolar pulse becomes bipolar after focal point. Therefore, two possibilities to switch the spin state of the $[Fe(NH_2 - trz)_3](Br)_2$ molecule exist.

The main goal is to induce a transition from HS state that has a bigger volume to LS state with smaller volume using a shock wave propagation (Figure 4.6(a), red arrow). The only possible way to induce HS $\rightarrow$ LS transition can be obtained within the hysteresis loop around the room temperature is by applying pressure to the molecule. This situation corresponds to the positive pressure part of the shock wave. Instantaneous increase in temperature that appears when a shock front forms doesn't play a role here because molecules in HS state remain in the same state with pressure increase.

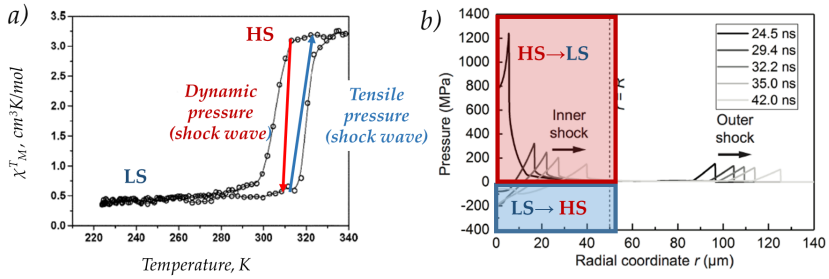

Figure 4.6 – a) *Illustration of a possible transition in* $[Fe(NH_2 - trz)_3](Br)_2$ *compound: positive pressure part of the cylindrical shock wave can induce HS* $\rightarrow$ *LS transition (red line) and negative pressure part that appears after focus can induce LS* $\rightarrow$ *HS (blue line);* ***b)*** *shock wave profile after focalization: tensile (negative) pressure part appears for a shock wave induced with a laser ring* [68].

Another opportunity comes from the shock wave propagation after focus. The tensile pressure part of the shock after focus will stretch out molecules that can induce LS $\rightarrow$ HS transition (Figure 4.6(a), blue arrow). Instantaneous increase in temperature induced by a shock front itself has to be taken into account in this case since it could also influence the final state.

Obviously, while working with a liquid suspension of spin crossover and dealing with cylindrical shock waves only a time resolved experiment could disentangle the happening transformation of the molecules.

4.3 Shock wave propagation in SCO suspension

4.3.1 Sample preparation

To prepare the suspension we took a certain amount of nanoparticles and a respective volume of ethanol and mixed them together in the ultrasonic bath or by stirring for $30\,\mathrm{min}$. Then, using micropipette, we took a few drops of obtained suspension and put it onto a glass substrate with a $10\,\mu\mathrm{m}$ spacer (polymer deposited on the substrate) and covered this cell with another glass substrate. We obtained regular liquid sample (see Figure 3.7). Thus prepared liquid sample was placed directly in the sample mount to hold it vertically.

Suspension concentration plays a big role in the imaging experiment because it influences on scattering and transmission of light. The criterium to find the optimal concentration was a compromise between obtaining a speckle less image at low concentration and a highly absorptive solution that can efficiently absorb the laser at high concentration. When the concentration of the solution was lower than $5\,\%$ we can not excite the shock wave due to low laser absorption but the image quality is the highest. At higher concentrations the solution efficiently absorb the laser for shock gen-

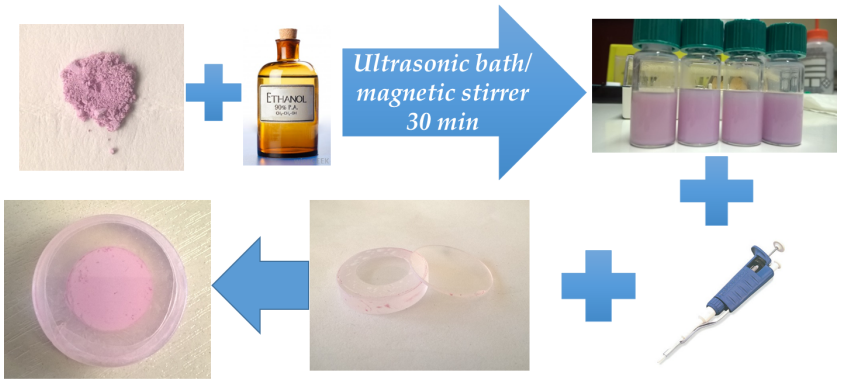

Figure 4.7 – *$[Fe(NH_2 - trz)_3](Br)_2$ suspension preparation routine for shock experiment: $50\,\mathrm{mg}$ of nanoparticles are dispersed in $1\,\mathrm{mL}$ of ethanol and mixed in ultrasonic bath or magnetic stirrer for $30\,\mathrm{min}$. Then a few drops of obtained liquid suspension are sandwiched between two glass substrates separated with a spacer.*

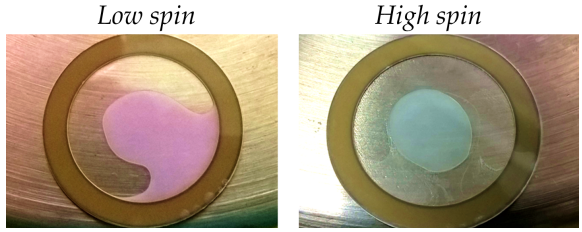

***Figure 4.8** – Color changes of thin layer of experimental suspension of $[Fe(NH_2 - trz)_3](Br)_2$ due to temperature change. The thin layer of prepared liquid suspension undergoes a color change from pink (LS) to white (HS) with temperature. Also, a decrease of liquid volume due to heating caused by ethanol evaporation is observed.*

eration but the solution becomes very dispersive and full of speckles that makes the obtained image very unclear. The suspension with concentration of $5\,\%$ ($50\,\mathrm{g/l}$) can be obtained if we took $50\,\mathrm{mg}$ of $[Fe(NH_2 - trz)_3](Br)_2$ nanoparticles and dispersed it in $1\,\mathrm{mL}$ of ethanol.

To reveal fundamental properties of these nanoparticles we carried out a preliminary test, simply by heating the liquid cell with a heating plate. The color of compound changed due to its spin state induced by temperature as demonstrated in Figure 4.8. The suspension from initial pink color (LS) becomes white (HS) and then remains white at room temperature. The initial pink color can be reversed only by cooling the sample back to $0\,^{\circ}\mathrm{C}$. The same results are obtained by repeating cycle.

4.3.2 Temperature control

We have modified the sample holder to be able to change and measure the exact temperature of the sample (Figure 4.9) and ultimately perform experiment in both spin states. Copper tubes (1) wrapped around sample are connected to chiller (*RTE-111*). Water circulates around the sample and, thanks to controlling the water temperature, we can change the temperature of the sample. To verify sample temperature we use a multimeter with a thermocouple (2): the end of thermocouple is placed close to the sample surface. This system allows to change temperature of the liquid from $-30\,^{\circ}\mathrm{C}$ to $150\,^{\circ}\mathrm{C}$. To cool the sample to the temperature below $0\,^{\circ}\mathrm{C}$,

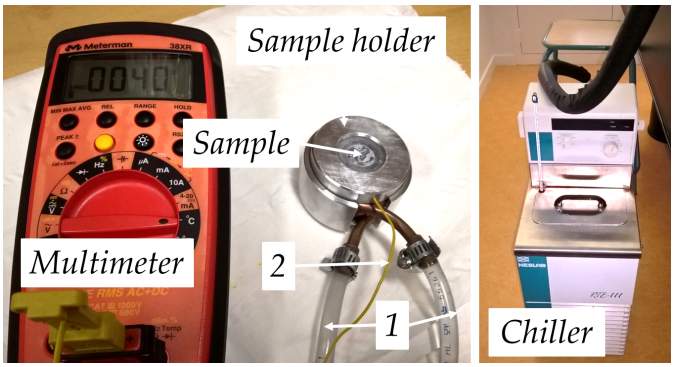

Figure 4.9 – *New elaborated temperature control system: sample holder contains copper tubes that allow water circulation around the sample. These tubes are connected to a chiller (RTE 111) with plastic tubes. This allows for a change of sample environment temperature from* $-5\,^{\circ}\mathrm{C}$ *to* $120\,^{\circ}\mathrm{C}$*. The sample temperature is measured by thermocouple connected to multimeter. The thermocouple probes temperature at the border of the sample placed in the centre of the sample holder.*

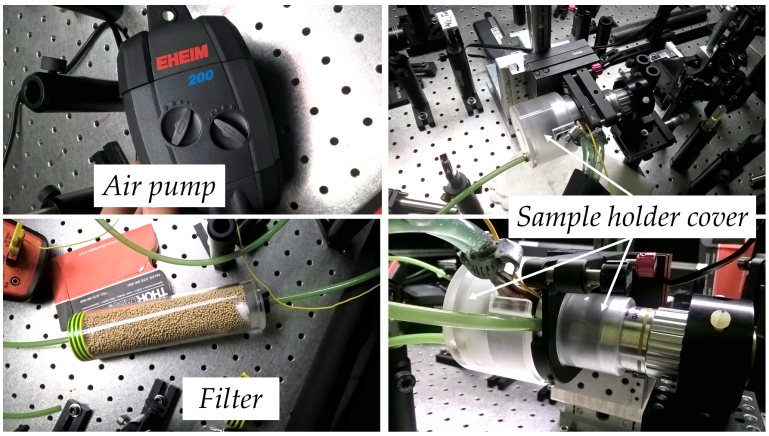

Figure 4.10 – *Dry air circulation system. A plastic cover of a sample holder protects a sample chamber from external environment. This cover is connected to a dry air filter and an air pump. This allows to avoid water condensation on sample surface during the cooling process and improves stabilisation of sample temperature.*

we used a ethylene-glycol mixture as coolant, because of its low freezing point: -13 °C.

During cooling down to 0 °C, we observed a condensation of water from air on the sample holder and glass windows. In order to thermally isolate the sample from laboratory environment we placed a dry air circulation chamber around sample (Figure 4.10). An air pump *EHEIM 200* equipped with two air outlets, both connected to a cartridge with air dryer. Then this filter is connected by tubes to the sample cover. Sample cover is a plastic ring which is mounted directly on a focusing lens or microscope objective. This ring closes the sample chamber from the pump side. From the other side a plastic hat is put on the sample holder in order to close sample chamber. This cylindrical hat has a glass window to open a path to probe laser pulse arriving from back side of the sample. Such system allows to cool sample down to -2 °C with no perturbation due to the condensation.

Temperature dependence of the transmission was measured for the obtained suspension of $[Fe(NH_2 - trz)_3](Br)_2$ in ethanol in order to verify the presence of hysteresis loop. For this we used a simple set-up of a white light that illuminates our sample from the back side. All transmitted light is collected with a fiber connected to an UV-VIS spectrometer. This way, we were able to measure a transmitted spectrum of the sample at different temperatures. Results, obtained for the wavelength of 300 nm, are presented on Figure 4.11. The spin state changes can be observed at 300 nm because there

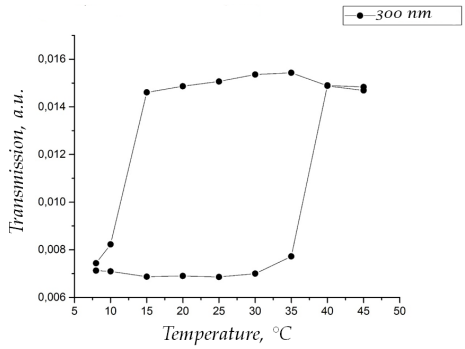

Figure 4.11 – *Transmission of* $[Fe(NH_2 - trz)_3](Br)_2$ *in ethanol measured with temperature change under* 300 nm *light excitation.*

is an absorption band in LS that disappears in HS. The LS $\rightarrow$ HS transition occurs at $40\,^{\circ}\mathrm{C}$ and reverse HS $\rightarrow$ LS transition appears at $5\,^{\circ}\mathrm{C}$.

4.3.3 Shock wave observation

Shock wave experiment was performed in transmission mode with Mach-Zender interferometer (see Chapter 3). As a pump we used a $300\,\mathrm{ps}$, $800\,\mathrm{nm}$ pulse; and $400\,\mathrm{nm}$, $150\,\mathrm{fs}$ pulse was used as a probe; both were taken from Solstice laser system. A 0.5^o Axicon (Doric Lenses, Inc.) was used to form a laser ring with a width of $\sim 10\,\mu\mathrm{m}$ and diameter of $200\,\mu\mathrm{m}$. Images were obtained with black/white CCD camera, so we can not judge on the color of the system.

Figure 4.12 demonstrates propagation of a shock wave generated with pump energy of $1.8\,\mathrm{mJ}$ in time. Images were recorded at room temperature when $[Fe(NH_2 - trz)_3](Br)_2$ solution was in LS and had a pink color. We could clearly observe two shock waves: converging and diverging one. The outer shock wave is going far away from the excitation ring and become less and less clear with time due to attenuation. A converging shock wave is propagating toward the centre of the laser ring and focalizes at $49\,\mathrm{ns}$, which gives us a shock speed $\sim 2\,\mathrm{km/s}$. This speed is different from one obtained in Chapter 3 in case of ink diluted in ethanol $(1.54\,\mathrm{km/s})$ due to different pump energies: $1.5\,\mathrm{mJ}$ for ethanol-ink solution and $1.8\,\mathrm{mJ}$ here.

Images of shock wave propagation due to different pump fluence are shown in Figure 4.13 (a). Pump fluence was controlled by a combination of polarized beam-splitter and half-wave plate. This study was performed at different temperatures in order to compare the shock speed in two states. Knowing a time delay we can estimate a shock speed for different pump powers. Figure 4.13 illustrates a shock wave position due to different pump powers. It indicates a bigger propagation distance for higher pump energy which is a typical feature of the shock wave. It was mentioned above that concentration of the solution is $5\,\%$, so the shock wave propagates mainly in the solvent and its behaviour is determined by ethanol. It explains, why we did not see difference in shock speed at two different spin states. Knowing the average speed of the excited shock wave and using the Hugoniot curve for ethanol [91], we can also estimate the applied pressure. At the lowest pump fluence, it is $5\,\mathrm{GPa}$ and for the highest fluence - $15\,\mathrm{GPa}$.

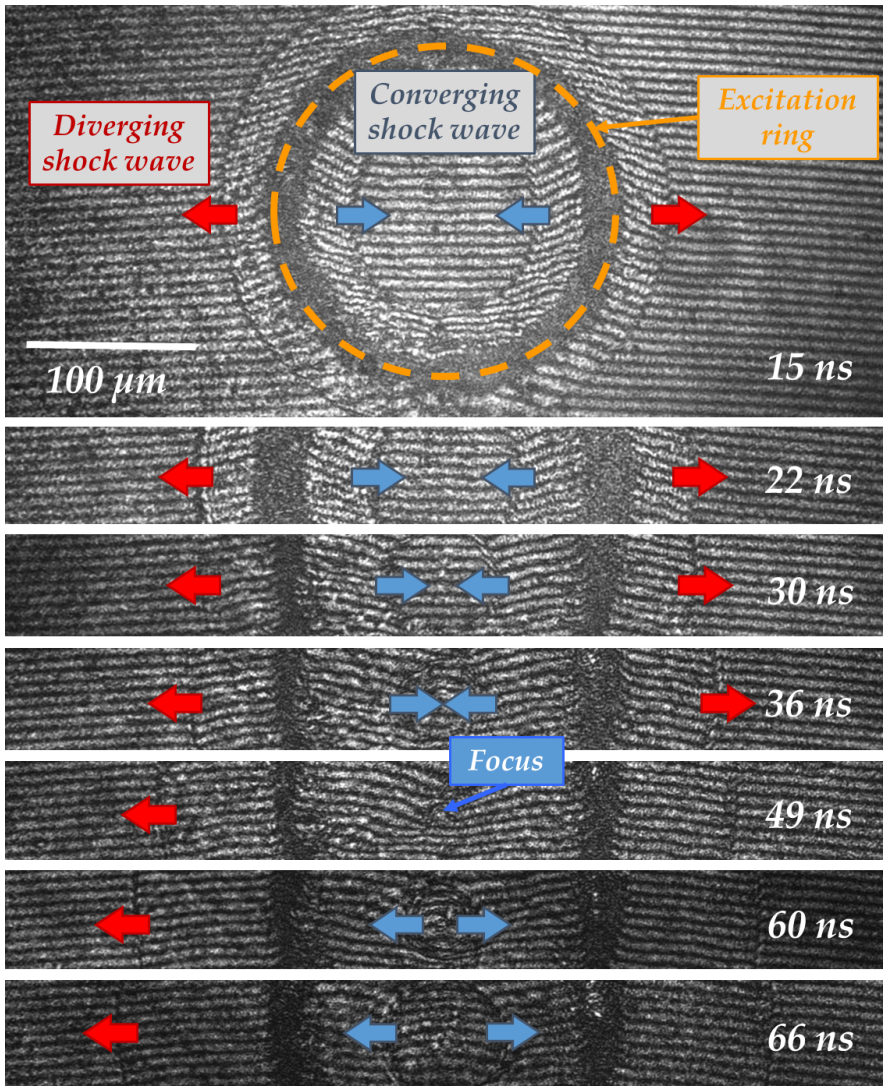

Figure 4.12 *– Time dependence of shock wave propagation in* $[Fe(NH_2 - trz)_3](Br)_2$ *thin layer suspension at ambient temperature generated with a laser energy of* $1.8\,\mathrm{mJ}$*. Inner shock wave focalizes within* $49\,\mathrm{ns}$ *and then goes back to excitation region.*

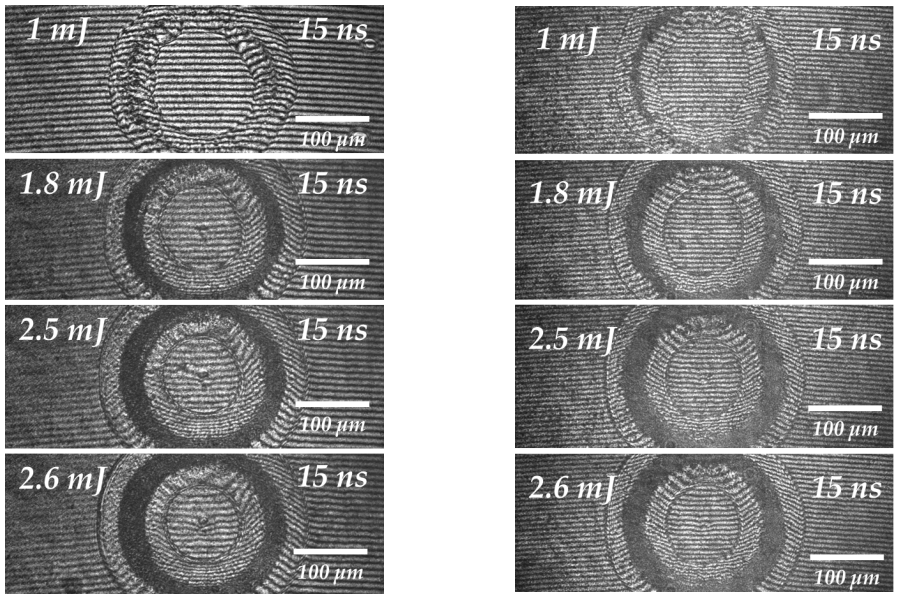

(***a***) $T = 0$ °C, *LS.* (***b***) $T = 47$ °C, *HS*

Figure 4.13 – *Power dependence of shock wave propagation in* $[Fe(NH_2 - trz)_3](Br)_2$ *thin layer suspension in HS and LS states.*

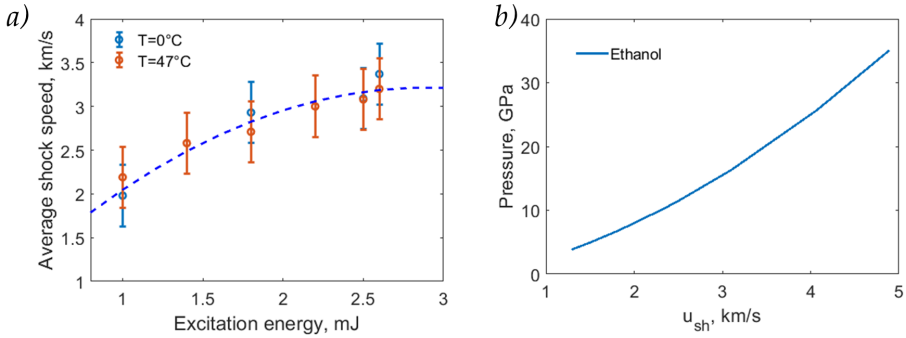

Figure 4.14 – *Experimental plots:* ***a***) *Shock wave speed in thin layer of* $[Fe(NH_2 - trz)_3](Br)_2$ *suspension in ethanol due to different pump fluences;* ***b***) *Hugoniot curve for ethanol* ([91]). *At max pump fluence we can generate* 15 GPa.

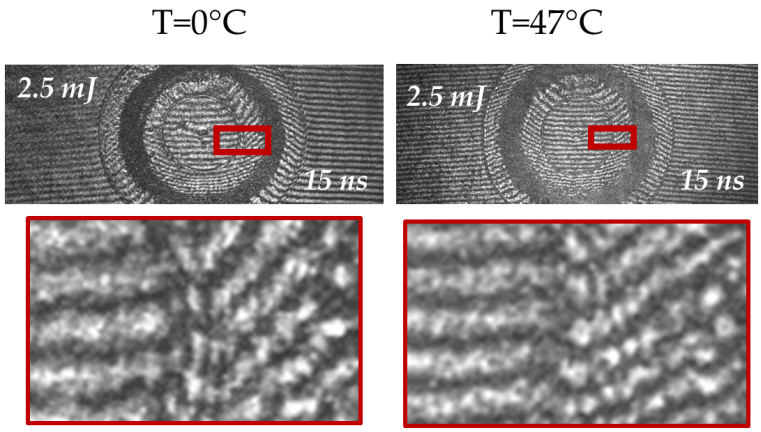

Figure 4.15 – *Comparison of the fringes profile for the* $[Fe(NH_2 - trz)_3](Br)_2$ *suspension at two temperatures: 0°C (LS) and 47 °C (HS).*

An interferometric imaging method was used in this experiment in order to be sensitive to changes in the real part of the refractive index of the compound. As it was shown in Figure 4.5(a) the real part of the refractive index of the $[Fe(NH_2 - trz)_3](Br)_2$ compound changes for $\Delta n = 0.1$ between LS and HS. We wanted to see if we can induce such change due to shock wave propagation and shock-induced spin modification of the nanoparticles. Zoom on the recorded images in Figure 4.15 show us an indication of different behaviours of the fringes bending at two different temperatures *i.e.* for two states. Also, it should be noticed that the introduced bending of the interferometry fringes was created not only due to a phase transition but also due to the shock wave itself *i.e.* $\Delta n = \Delta n_{shock} + \Delta n_{spin}$.Knowing, that by applying pressure to this compound in LS it is impossible to excite HS, the fringes shift at $0\,°C$ can be used as a reference for the Δn_{shock} and so we can determine the Δn_{spin} from images at high temperature $(0\,°C$, HS). Unfortunately, recorded images made it impossible to tell something precise and repeated experiments should be made in order to access accurately this information.

4.3.4 Sample behaviour at high temperature

First and foremost, ethanol was chosen because it does not alter the magnetic properties of $[Fe(NH_2 - trz)_3](Br)_2$ crystallites. However, its boiling point is $78\,^{\circ}\mathrm{C}$. We observed a rapid evaporation of ethanol with the increase of temperature. To solve this problem we use a silicon gel on the edges of prepared sample for tight sealing. But then we observed an aggregation of diluted nanoparticles (see Figure 4.16) thus homogeneity of the sample was severely altered at high temperature. Unfortunately, this sample can not be run through thermal cycles. In order to simplify the working process with this kind of materials and avoid problems with ethanol (evaporation, aggregation), we decide to switch to a thin film solid dispersion in a polymer. However, we are faced with a different problem: unfortunately, this compound is not stable in all polymers and loses its properties in few hours.

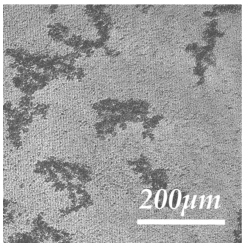

Figure 4.16 – *Image of the aggregated nanoparticles in suspension due to high temperature T=*$47\,^{\circ}\mathrm{C}$*. Image recorded with a* $400\,\mathrm{nm}$ *illumination pulse.*

It is worth to mention that the working process brought a number of challenges, some of which were dealt with, but a decision was made to put on hold further work and move on to a sibling compound, morphologically more resilient and stable (see following chapter). Nevertheless, the $[Fe(NH_2-trz)_3](Br)_2$ compound opens a well founded perspective for investigation of shock induced phase transition. Obviously, from black/white images it is impossible to judge whether or not the transition took place. It was mentioned that this compound has a strong absorption band at $300\,\mathrm{nm}$ in LS state. The use of this particular wavelength as a probe for time-resolved shock imaging will help us to determine a color change related to spin transition, and not only shock propagation.

4.4 $[Fe(HB(tz)_3)_2]$ compound

$[Fe(HB(tz)_3)_2]$ (tz=1,2,4-triazol-l-yl) compound has very similar properties to the previous one - $[Fe(NH_2{-}trz)_3](Br)_2$. Crystals of $[Fe(HB(tz)_3)_2]$ are known to exhibit an extremely abrupt first-order, isostructural spin transition above room temperature ($61\,^{\circ}\mathrm{C}$). Recently, this complex was successfully deposited on different substrates by thermal evaporation allowing to obtain high-quality, nano-crystalline thin films [115]. Finite size effects on the spin-state switching dynamics of these films were recently reported by Ridier et al. [116].

Figure 4.17 (a) shows the UV-Vis absorbance spectra of the $100\,\mathrm{nm}$ thick film at various temperatures between $20\,^{\circ}\mathrm{C}$ and $120\,^{\circ}\mathrm{C}$. At room temperature , *i.e.* at LS state, the films exhibit intense absorption bands in the UV range between 250 and $340\,\mathrm{nm}$, which completely disappear with heating and transition to HS state. The temperature dependence of the HS fraction, extracted from the variation of the optical density with $\lambda = 317\,\mathrm{nm}$, is shown in Figure 4.17 (b). The films of different thickness exhibit a similar spin transition around $64\,^{\circ}\mathrm{C}$ with a narrow thermal hysteresis of $\sim 0.8\,^{\circ}\mathrm{C}$ width.

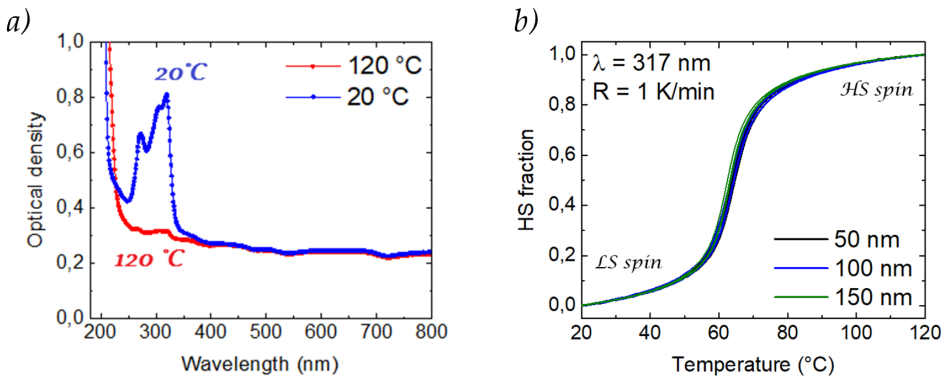

Figure 4.17 *– Characterization of* $[Fe(HB(tz)_3)_2]$ *thin films:* ***a)*** *Optical absorbance spectra of the* $150\,\mathrm{nm}$ *thick film at two different temperatures:* $20\,^{\circ}\mathrm{C}$ *(LS) and* $120\,^{\circ}\mathrm{C}$ *(HS);* ***b)*** *temperature dependence of the HS fraction at* $\lambda = 317\,\mathrm{nm}$ *during one heating–cooling cycle at* $1\,^{\circ}\mathrm{C/min}$ *scan rate for the three films* [116].

Ridier et al. [116] investigated photo-induced switching dynamics induced by a femtosecond laser pulse in $[Fe(HB(tz)_3)_2]$ thin films. They observed photo-induced and elastic steps that follow a low spin to high spin transition initially induced by femtosecond laser pulse. Figure 4.18 shows different photo-responses in the $100\,\mathrm{nm}$ thick film due to various excitation energies. Authors clearly observed a threshold phenomenon: for fluences below $4\,\mu\mathrm{J}$ the photo-switched molecules return to the LS ground state through a single-step relaxation process occurring within $100\,\mathrm{ns}$. Above an excitation threshold of $6\,\mu\mathrm{J}$ a second increase of HS molecules fraction is observed on nanosecond timescale.

4.5 Preliminary investigation of SCO thin films

Investigated sample was $200\,\mathrm{nm}$ thin film of $[Fe(HB(tz)_3)_2]$ deposited on the glass substrate provided by research group 'Matériaux moléculaires commutables' from Laboratoire de Chimie de Coordination de Toulouse. We verified a thermal hysteresis loop the same way as we did for $[Fe(NH_2-$

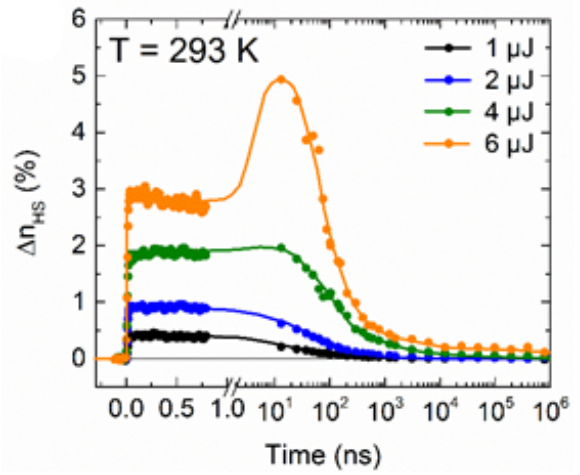

***Figure 4.18** – Photo-response of the thin films of $[Fe(HB(tz)_3)_2]$ on the ns-ms time range: Time evolution of Δn_{HS} at room temperature in the 100 nm thick film following a femtosecond laser pulse with various excitation energies.*

$trz)_3](Br)_2$ in ethanol. Figure 4.19(a) shows the optical transmission measured at $\lambda = 308\,\mathrm{nm}$. We clearly observe transmission changes with temperature. These results correlates with results presented above: slightly bigger width of the hysteresis is due to the way we measure the temperature (see section 4.2.3). These measurements show that above $80\,^{\circ}\mathrm{C}$ our thin film is in HS state and below $50\,^{\circ}\mathrm{C}$ - in LS state. Transmission change for over $50\,\%$ between LS and HS at $308\,\mathrm{nm}$.

Ring shaped excitation experiments were performed on $200\,\mathrm{nm}$ thin film of $[Fe(HB(tz)_3)_2]$ compound with $800\,\mathrm{nm}$ pump and $400\,\mathrm{nm}$ probe. Because we work with the solid sample thus we will excite a surface acoustic waves (see Chapter 2). The very first try to generate SAW in direct ablation failed because of low optical density of this sample at $800\,\mathrm{nm}$. Figure 4.19(b) illustrates an image of shock wave propagation. In these experiments however, we did not observe a laser irradiated region, not even a shock front.

To increase the amount of energy deposited by a pump pulse we deposited on top of a thin film the gold rings as done by Veysset et al. [92]. Gold has a high absorption in Vis-range which allows for easier generation

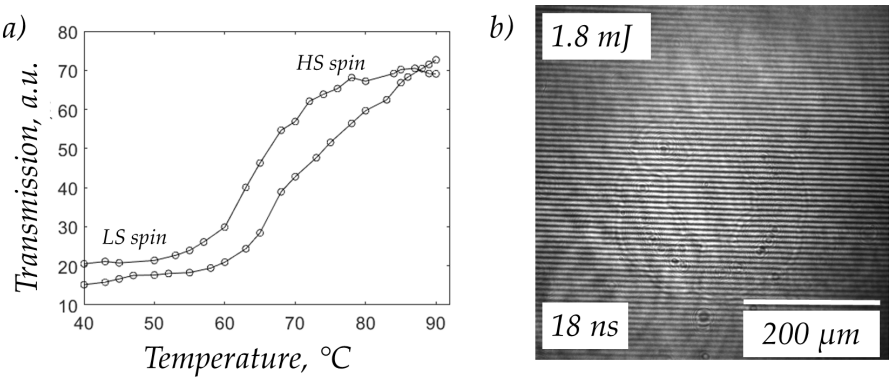

***Figure 4.19** – Results: **a**) Measured temperature hysteresis of $200\,\mathrm{nms}$ $[Fe(HB(tz)_3)_2]$ thin film sample recorded at $308\,\mathrm{nms}$; **b**) image of SAW excited at $800\,\mathrm{nm}$ with a fluence $1.8\,\mathrm{mJ}$ on $[Fe(HB(tz)_3)_2]$ $200\,\mathrm{nm}$ thin film at $18\,\mathrm{ns}$ delay. A small absorption of $800\,\mathrm{nm}$ lies to a weak SAW wave. We hardly observe a small damage even at a laser ring region, which usually is the most damaged.*

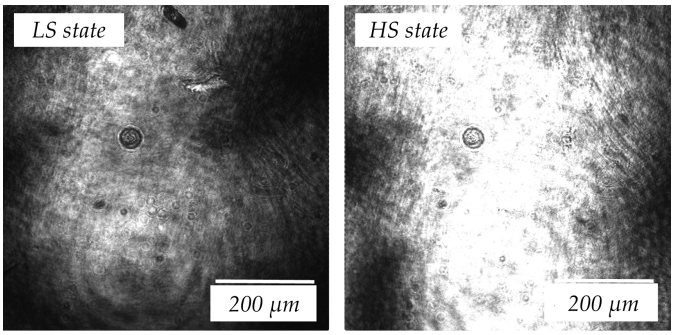

Figure 4.20 – *$[Fe(HB(tz)_3)_2]$ thin film intensity changes with temperature.*

of the surface acoustic waves. I carried out these trials during my short stay at Massachusetts Institute of Technology (Cambridge), where identical experimental setup I used at IMMM (Le Mans) was available. The advantage of the MIT experiment resides in broad wavelength tunability for time-resolved imaging. However, the first attempts were hindered by the limits of chemical deposition process, also carried out at MIT. The films turned out to be very sensitive to a lift-off process following the deposition of gold rings.

Also, a $400\,\mathrm{nm}$ wavelength was used as a probe light for all of shock experiments discussed in this section. $[Fe(NH_2-trz)_3](Br)_2$ in ethanol as well as $[Fe(HB(tz)_3)_2]$ have weakly varying absorption between LS and HS states at this wavelength. In UV range, more precisely at $300\,\mathrm{nm}$, both compounds reveal strong absorption band only in LS state. Subsequently, we should switch to this wavelength to probe a phase change during shock wave excitation and propagation. Switching the wavelength can be done by using *Optical Parametric Amplifier* (OPA). It is a well-known non-linear optical process occurring in second-order non-linear crystals and involving energy transfer among beams at different frequencies. I used OPA *TOPAS-C @ Light Conversion* output for imaging at different temperatures: at $20\,^{\circ}\mathrm{C}$ (LS) and $80\,^{\circ}\mathrm{C}$ (HS) for thin films sample. Results are presented in Figure 4.20. The strong contrast is a strong difference in the image intensity for low spin state and high spin state. This intensity difference is a valuable parameter to investigate changes in real-time upon, and in-the-wake of shock propagation.

4.6 Conclusion

This chapter has addressed the appearance of self-amplified elastic steps after photo-excitation of different spin-crossover compounds. The appearance of the elastic step at a nanosecond (acoustic) timescale indicates a coupling between the LS/HS switching and the elastic wave. That leads us to the question: can an elastic wave alone drive this transition?

Here we demonstrate successful generation of shock waves in thin layer of $Fe(NH_2 - trz)_3](Br)_2$ suspension in ethanol. The speed of the shock wave and the pressure are determined by ethanol, because the concentration of $Fe(NH_2 - trz)_3](Br)_2$ nanoparticles in suspension was just $5\,\%$. Knowing the Hugoniot properties of the ethanol and the shock wave speed, extracted from imaging, we can estimate the pressure: at highest pump fluence which is $15\,\mathrm{GPa}$. Unfortunately, at high temperature the sample is unstable: the nanoparticles start to aggregate and subsequently the homogeneity of the sample is altered.

$[Fe(HB(tz)_3)_2]$ thin films are more promising. They show so far the existence of an elastic step at a nanosecond timescale after photo-excitation. The first shock wave experiments failed so far due to low absorption in the Vis range. It can be improved by depositing on the top of the thin film several gold rings. Future experiments are already in preparation. We plan to perform shock wave experiments on $[Fe(HB(tz)_3)_2]$ thin films with gold rings; this will allow us to increase the efficiency of the SAW generation. Imaging in the UV range (particularly at $300\,\mathrm{nm}$) will allow us to directly detect changes in absorption between HS$\rightarrow$LS. Following post-mortem diffused reflectivity or spectral ellipsometry measurements of 'shocked' regions will indicate whether there was phase transition or not.

Another important point is the duration of the generated shock wave (non-linear SAW). LS and HS states are separated by local energy barriers and ultimately the time required to overcome the barriers is determined by thermo-elastic processes: while pressure can reduce the barrier immediately, the temperature changes need some time to change the probability of molecules to reside either in LS or HS. So we need to introduce a new parameter - the latency time between the elastic propagation and HS/LS switching. This means that not only the amplitude of the shock but also the duration may be a critical parameter. Thus, we plan to perform the

shock wave experiment with different pump pulse durations (picosecond and nanosecond).

Chapter 5

Shock wave in correlated materials

5.1 Insulator-to-metal transitions in correlated materials

By *Correlated materials* we call all systems for which the interactions between different degrees of freedom have to be considered in order to describe their properties. Among correlated materials, the large class of 3d transition metal oxides (*i.e.* oxides containing elements between titanium $Z = 22$ and copper $Z = 29$) is particularly attractive. In these materials, the coexistence of various relevant degrees of freedom – spin, charge, orbital and lattice – leads to an extraordinary variety of phases in competition, as illustrated in the representative example of manganites shown in Figure 5.1. It is noteworthy that some of these phases are metallic while others are semiconducting or insulating. Application of external stimuli such as temperature, pressure or electronic doping (modification of the average number of electron per transition metal) can easily induce insulator-to-metal transition in such materials.

We will not discuss here all possible situations leading to *insulator- to-metal transitions* (IMT). We will rather focus on the simple case of IMT's in Mott insulators. The Mott insulator state is ubiquitous in transition metal oxide. One of the reason is that $3d$ electrons have a small radius of the wave

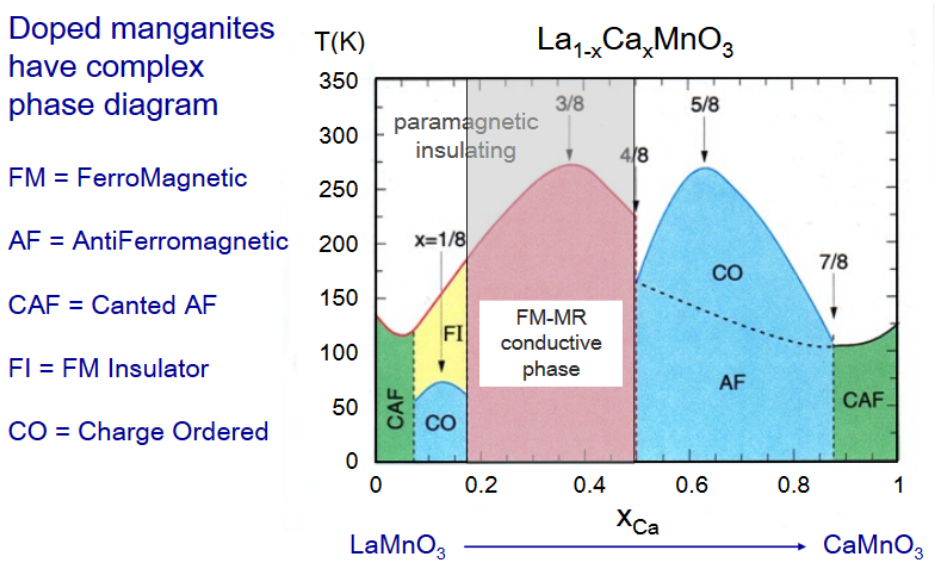

Figure 5.1 *– Illustration of the variety of phases in competition existing in a typical transition metal oxide, the $La_{1-x}Ca_xMnO_3$ family. By varying the average number of 3d electron per Mn – from $3d^4$ in $LaMnO_3$ to $3d^3$ in $CaMnO_3$ – and temperature, several insulating or metallic phases with various charge or magnetic order can be stabilized. Adapted from* [117].

function compared to the crystal lattice parameter, which leads to two important consequences. First, there is only a moderate overlap of the $3d$ orbitals with the $2p$ orbitals of oxygen ligands, leading usually to a moderate or small bandwidth W. Second the electrostatic (Coulomb) repulsion between unpaired $3d$ electrons confined in the small volume of the $3d$ wave function is dramatically enhanced compared to uncorrelated materials – such as silicon with its [Ne] $3s^2 3p^2$ electronic configuration – where valence electrons lie in large s or p orbitals. This repulsive energy U between electrons located on the same transition metal is neglected in the standard band theory. This has led to dramatic failures of this theory in the case of correlated materials.

In 1937, De Boer and Verwey pointed out that the transition metal oxides with partially filled $3d$ and $4d$ orbitals behave as insulators, whereas

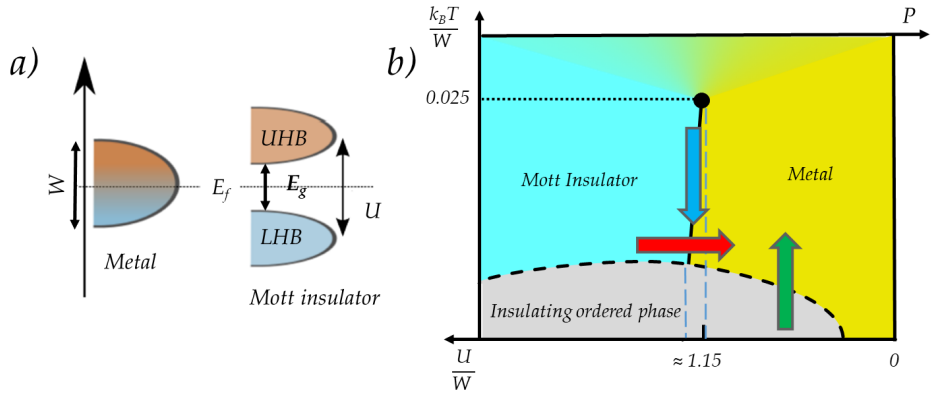

***Figure 5.2** – Basic concept of Mott insulator: **a**)lower and upper Hubbard bands created from a partially filled band W due to Coulomb repulsion U; **b**) schematic phase diagram of half-filled compounds: Mott insulator and metal phases are separated by first order transition line. Arrows indicate possible transitions due to different external stimuli: pressure (red arrow) and temperature (blue and green arrows). Transition along green arrow happens with the change of symmetry. Adapted from [121].*

the standard band theory would predict a metallic state [118]. These observations led N.F. Mott to propose that repulsive electrostatic interaction between electrons might explain this discrepancy [119, 120]. This illuminating idea allowed to define a new class of insulating materials beyond the well understood class of band insulators, the *Mott insulators*.

As mentioned above, the Mott insulator state is ubiquitous in $3d$ transition metal oxides. However, it exists only if a specific condition is fulfilled: the average number per $3d$ transition metal has to be an integer. This situation is encountered for example in V_2O_3 (V^{3+}, electronic configuration $3d^2$, hence two unpaired $3d$ electrons per vanadium), but not in Ti_3O_5 (average valence $Ti^{3.33+}$, electronic configuration intermediate between $3d^0$ and $3d^1$ with two $3d$ electrons for three titanium: 0.66 $3d$ electrons per titanium on average). Let us consider for simplicity a compound with a single band close to the Fermi energy, partially filled with one electron. In this so-called half-filled situation (only one electron is in a band that can contain two electrons), such a material should be metallic according to the conventional

band theory because its Fermi levels lie exactly in the middle of the band (Figure 5.2(a)). However when the Coulomb repulsion energy U becomes greater than the bandwidth W , this band splits in two sub-bands: so-called *lower* and *upper Hubbard bands*. An energy gap created between LHB and UHB is roughly equal $Eg = U - W$. In a Mott insulator the valence electrons are localized on the transition metals ions therefore the conductivity is significantly low. This can be viewed as a competition between the kinetic energy of the electrons and the Coulomb repulsion.

Numerous transition metal oxides exhibit this kind of Mott insulating state, for example titanium oxides, vanadium oxides, or copper oxides [122–124]. As expected from the above discussion, increasing the bandwidth (*i.e.* decreasing the U/W ratio) can lead to a transition between the Mott insulating state and a metallic state. The classical phase diagram: temperature – U/W of Mott materials (Figure 5.2(b)) shows this almost vertical first order transition line between insulating and metallic phases. This line ends with a critical point at high temperature. Classical IMT occurs without symmetry breaking. There are three main ways to initiate IMT in Mott insulating systems:

- bandwidth control: thanks to application of an external pressure which enhances the orbitals overlap and increases the bandwidth W (red arrow);
- temperature control: done in a narrow band of $U/W \approx 1.15$ around transition line between high temperature insulator and low temperature metal (blue arrow);
- filling control: chemical doping will change a number of electrons per transition metal and can induces a Mott insulator-to-metal transition.

There also exists a fourth way (green arrow) which in theory is possible if material exhibits a long-range order at low temperature (insulating ordered phase, Figure 5.2(b)). In reality, this transition usually happens with crystallographic symmetry breaking, thus this process involves some mechanism additional to competition between the kinetic energy of the electrons W and the Coulomb repulsion U. An overview of Mott insulator compounds can be find in the article of Janod et al. [121].

As mentioned above, a bandwidth-controlled insulator to metal transition is induced by application of pressure in canonical Mott insulators. This transition is accompanied by compression of the unit cell volume. In the

canonical Mott system V_2O_3, the volume decrease at the pressure-induced IMT is around $-1.4\,\%$.

Conversely, the Ti_3O_5 system can also undergo a pressure-induced metal-insulator transition (see next section), but with an opposite unit cell volume change : the unit cell volume of the metallic $\lambda - Ti_3O_5$ phase is larger than the one of the isostructural and semiconducting $\beta - Ti_3O_5$. In this context, this makes these two systems, V_2O_3 and Ti_3O_5, very promising case study for shock wave application. This section concentrates on these two solid materials. We will discuss the propagation of non-linear surface acoustic waves (SAW) that could possibly initiate volatile or non-volatile phase transition. The variation of laser fluence will reveal a clear **non-linear behaviour of the generated SAWs** which is the signature of the shock wave. Regions of the sample that undergo SAW influence will be called *'shocked'* in all following discussions. Examination of these 'shocked' regions gives us an indication if phase transition took place or not.

5.2 Semiconductor to metal transition in Ti_3O_5

Ti_3O_5 compound is a correlated material undergoing of semiconductor to metal transitions. Ohkoshi et al. [125] found a unique metallic phase of titanium oxide, $\lambda - Ti_3O_5$. Heating this phase to $367\,^{\circ}\mathrm{C}$ causes a second order phase transition to a $\alpha - Ti_3O_5$ - high temperature metallic phase. By applying a static pressure to a flake sample $\lambda - Ti_3O_5$, part of the crystals can be converted to β phase which is semiconductor with a bandgap of $0.14\,\mathrm{eV}$. By application of pressure we can convert up to $80\,\%$ of the sample (Figure 5.3(b)). X-ray diffraction measurements showed appearance of β phase peak and decreasing of λ peak intensity (Figure 5.3 (a)) with pressure increasing.

Ohkoshi et al. [125] also demonstrated a photoinduced transition from $\lambda - Ti_3O_5$ to $\beta - Ti_3O_5$ (Figure 5.4(a)). When the flakes of $\lambda - Ti_3O_5$ were irradiated six times with $532\,\mathrm{nm}$, $6\,\mathrm{ns}$ laser pulse with fluence $1.5 * 10^{-5}(mJ/\mu m^2)$ pulse at room temperature, the irradiated area changed from black $\lambda - Ti_3O_5$ to brown $\beta - Ti_3O_5$ (Figure 5.4(b)). Subsequent irradiation with $410\,\mathrm{nm}$ $(8 * 10^{-3}mW/\mu m^2)$ caused irradiated spots return to black. The X-ray diffraction measurements showed that brown area was a β-phase. Hence, the color change from black to brown indicates a transition from $\lambda - Ti_3O_5$ to $\beta - Ti_3O_5$. Recovering initial black color after second irradiation confirmed the reverse transition from $\beta - Ti_3O_5$ to $\lambda - Ti_3O_5$. Irradiation with different nanosecond-pulsed laser at 533 or $1064\,\mathrm{nm}$, caused a similar phase transition.

Figure 5.4(b) describes all possible ways to induce a phase transition in Ti_3O_5. Transition from a metastable $\lambda - Ti_3O_5$ (red line) to a true stable $\beta - Ti_3O_5$ (blue line) phase can be generated by nanosecond pulse (blue arrow pointing downwards and a top inset). The reverse transition from $\beta - Ti_3O_5$ to $\lambda - Ti_3O_5$ can be excited in two waves: directly by nanosecond pulsed laser irradiation (blue arrow pointing upwards and a middle inset) or by continuous wave laser irradiation system firstly pass through $\alpha - Ti_3O_5$ to give $\lambda - Ti_3O_5$ (dotted blue arrow and bottom inset).

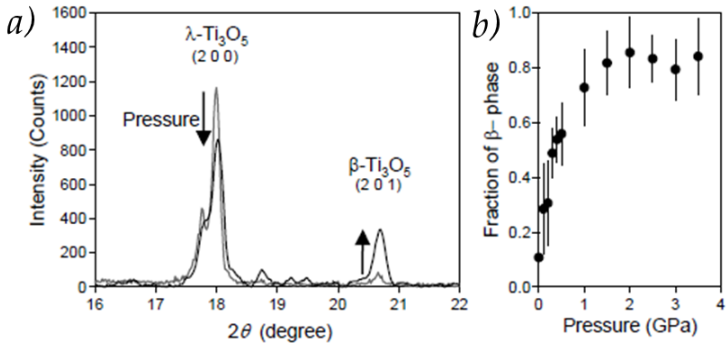

Figure 5.3 – *The pressure induced phase transition of Ti_3O_5 in its flake form:* ***a)*** *X-ray diffraction diagram of the flake before (gray) and after (black) applying external pressure of 0.3 GPa;* ***b)*** *The increase of the fraction of $\beta - Ti_3O_5$ by the external pressure [125].*

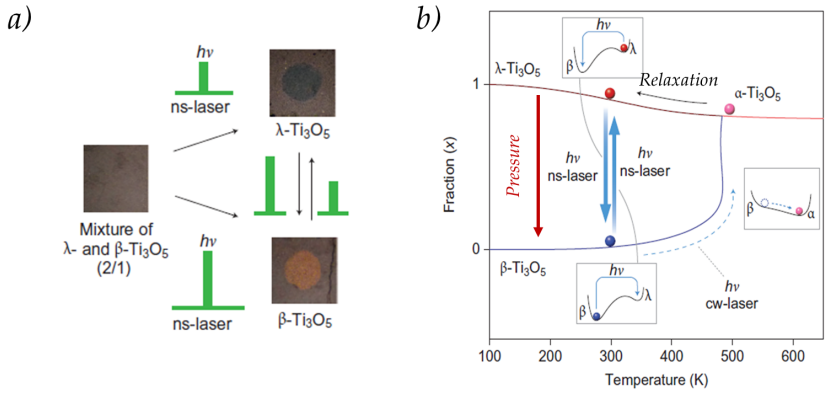

Figure 5.4 – a) *A mixed flake sample of λ and β phases ($\lambda/\beta = 2/1$) irradiated with 532 nm pulsed laser light at various laser-power densities [125];* ***b)*** *Mechanism of the photo-induced phase transition in Ti_3O_5. Red, pink and blue lines indicate different phases of Ti_3O_5: λ, α and β respectively. Reversible $\lambda - Ti_3O_5$ to $\beta - Ti_3O_5$ transition can be achieved by excitation with ns laser pulse. Transition $\beta - Ti_3O_5 \rightarrow \alpha - Ti_3O_5$ can be induced by cw laser and then it's thermally stabilizes into $\lambda - Ti_3O_5$ phase.*

5.2.1 Sample characterization

For studies, we took a $\beta - Ti_3O_5$ pellet made with a nanocrystals of $\sim 1\,\mu m$ size and prepared from $\lambda - Ti_3O_5$ flake by applying pressure of 2.7 GPa. In results, our sample consisted of 70 % of $\beta-$ phase and 30 % of $\lambda-$ phase. This sample was provided by Ohkoshi and Tokoro research group from the University of Tokyo. White light microscopy images (Figure 5.5(a-b)) illustrate the color difference of our samples: majority $\beta - Ti_3O_5$ and pure$\lambda - Ti_3O_5$ phases. The majority $\beta - Ti_3O_5$ phase pellet is darker than the pellet of $\lambda-Ti_3O_5$ phase. Histograms shows that RGB components have an equal contribution to color of a final image. By comparing histograms (Figure 5.5(c)) of $\beta-$ and $\lambda-$ phase, it indicates darkening in case of $\beta - Ti_3O_5$. We clearly see that the intensity distribution for $\beta-$ phase is sharper and asymmetric compare to the $\lambda-$ phase. We observe a shift of the median to lower pixel values in case of $\beta-Ti_3O_5$. We used these RGB color changes and looked at histogram treatment for the sample post-mortem analysis in order to reveal a phase of the 'shocked' regions.

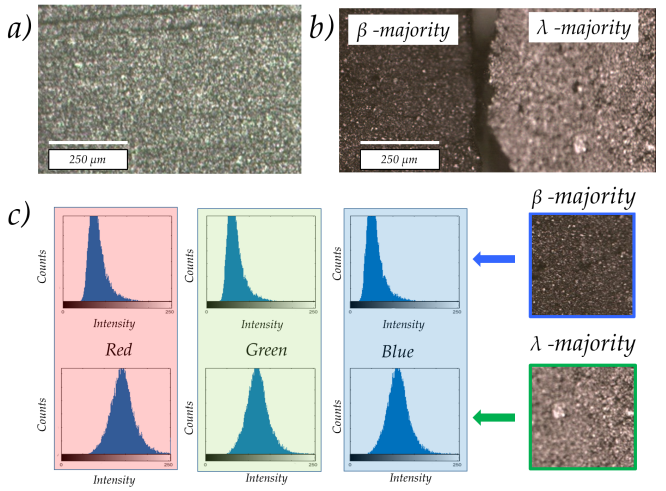

Figure 5.5 *– Sample characterization:* ***a****) surface of the mixture of* 70 % $\beta-Ti_3O_5$ *and* 30 % $\lambda - Ti_3O_5$ *flake sample;* ***b****) color difference between two states: pure* $\lambda - Ti_3O_5$ *and majority* $\beta - Ti_3O_5$*;* ***c****) histograms of RGB components for both* $\beta-$ *and* $\lambda-$ *phases.*

5.2.2 SAW observation on powdered samples

A shock wave experiment in reflection described in Chapter 3 was performed on $\beta - Ti_3O_5$ pellet. Because our sample is solid the waves we observed are surface acoustic waves (SAWs). SAWs were excited with $300\,\mathrm{ps}$, $800\,\mathrm{nm}$ laser pulse and images of their propagation were observed at $150\,\mathrm{fs}$, $400\,\mathrm{nm}$ laser pulse; both coming from the *Solstice @ Spectra Physics* laser system. We recorded several shots at various time delay and pump energies. The laser ring diameter was set to $200\,\mu\mathrm{m}$.

A sequence of images of surface acoustic waves excited with power of $2\,\mathrm{mJ}$ registered at different time delays is shown in Figure 5.6(a). Ring radius was $\sim 105\,\mu\mathrm{m}$ and laser ring width $\sim 10\,\mu\mathrm{m}$. SAWs appear as a broad dark region that makes it more challenging to determine the SAWs propagation compared to all previous shock observations (see Chapters 3-4). It can be explained by high inhomogeneity of the sample: nanoparticles size is of the same order as the laser wavelength (hundreds of nm). As we can see, at $58\,\mathrm{ns}$ the inner SAW is still not focalized at the centre of the laser ring that allows to determinate an average speed of $\sim 1.75\,\mathrm{km/s}$. Figure 5.6(b) shows the SAW position at the same delay $(33\,\mathrm{ns})$ but at different excitation powers.

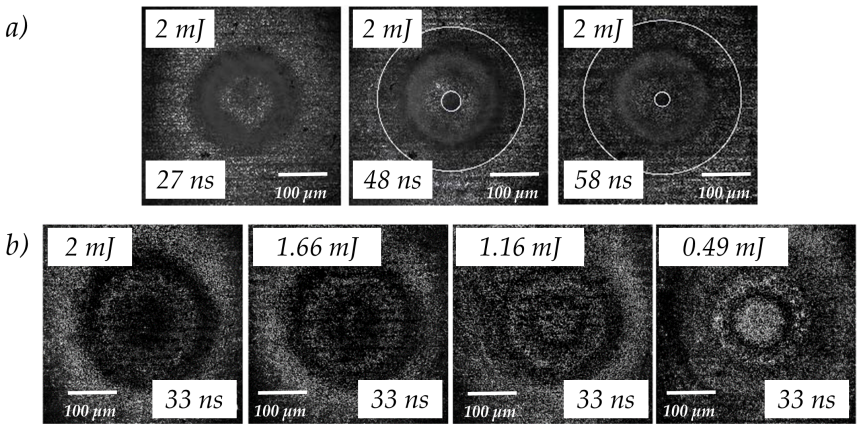

Figure 5.6 *– SAW propagation on Ti_3O_5 sample surface:* ***a****) at different time delays with pump power of $2\,\mathrm{mJ}$;* ***b****) Images taken with $33\,\mathrm{ns}$ after laser excitation at different pump powers.*

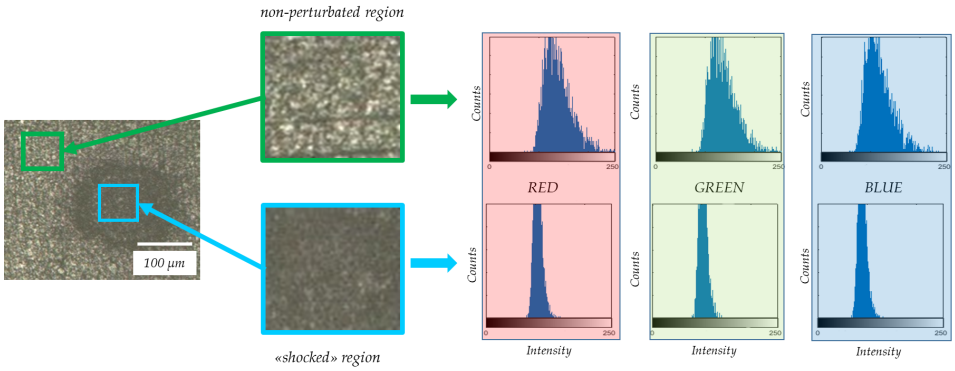

Figure 5.7 *– White light microscopy image of Ti_3O_5 after SAW propagation. We can notice some color change on 'shocked' regions, which are darker than the non-'shocked' sample regions.*

White light microscopy performed on the sample indicates slight color change between non-perturbed region and the 'shocked' regions. Histogram analysis of the RBG components of post-mortem image (Figure 5.7) shows the results clearly different from Figure 5.5(c). Here we can see that non-perturbed (mixture of $\beta-$ and $\lambda-$ phases in proportion $3:1$) sample has distribution shape similar to the $\beta-$ phase but shifted towards higher pixel intensity. The 'shocked' region, in contrary, is more similar to the $\beta-$ phase case. It seems that the 'shocked' region is more $\beta - Ti_3O_5$ than the initial mixture. This can happen only if we convert $30\,\%$ of $\lambda - Ti_3O_5$ initially present in sample to $\beta - Ti_3O_5$ due to SAW propagation.

Figure 5.4(b) illustrates the switching pathway from λ to β - phase that can be obtained only by pressure: heating of λ-phase leads to high-temperature α-phase and then, by relaxation, back to initial phase. Compression of β-phase due to SAW propagation will not give us λ - phase: compound will stay in its initial β-phase. Therefore, the only possible explanation of the observed color change is the transition of $30\,\%$ of $\lambda - Ti_3O_5$ initially present in sample to $\beta - Ti_3O_5$.

Because the observation of the surface acoustic waves wave is failed due to a surface morphology of the sample, we decided to switch to similar compound - canonical Mott insulator, V_2O_3.

5.3 Insulator-to-metal transition in $(V_{1-x}Cr_x)_2O_3$

Discovered in 1946 by Marc Foëx [126], V_2O_3 compound has attracted a lot of interest and become a textbook example of Mott-Hubbard physics. Over the years many theoretical and experimental efforts have been devoted to understand in detail the behaviour of this compound.

Phase diagram. Vanadium sesquioxide has a sharp first-order insulator-to-metal transition. Three regions can be determined in pressure - temperature - composition phase diagram for V_2O_3 system: *paramagnetic metal* (PM), *paramagnetic insulator* (PI) and *antiferromagnetic insulator* (AFI) (Figure 5.8). Pressure origin that induced phase transition in V_2O_3 can be external (hydrostatic) and internal (chemical). In a simplified view, chemical pressure can be introduced with substitution of vanadium by some other isovalent elements like chromium.

The pure compound V_2O_3 is a metal with corundum structure. Transition from PM to AFI phase can be observed at around $T = 160\,\mathrm{K}$ with a seven orders of magnitude resistivity jump. This transition is accompanied by a crystal symmetry change contrary to a classical IMT transi-

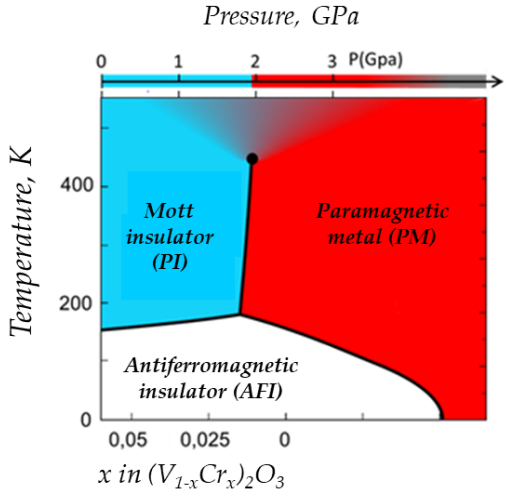

***Figure 5.8** – Pressure-temperature-composition phase diagram of V_2O_3 compound. Adapted from [127].*

tion. For Cr-doped V_2O_3 compound a new insulating phase appears with the same corundum structure but with slightly different lattice parameters. This transition (PM-PI) is a true Mott transition since there is no symmetry breaking. The resistivity of the insulating phase drops by almost two orders of magnitude compare to the metallic phase. The transition can also be crossed using hydrostatic pressure starting from PI phase. The transition PI-AFI can be observed with a temperature decrease at around $T = 180\,\mathrm{K}$. The transition from PM to AFI displays a much stronger change of resistivity: a jumps 6 orders of magnitude. The first order transition line presents a large temperature hysteresis ending at a second order critical point. Above the critical endpoint at $450\,\mathrm{K}$, there is no longer a transition, but a continuous crossover between the Mott and the correlated metal phases.

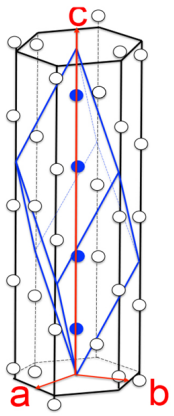

***Figure 5.9** – V_2O_3 crystal structure showing the hexagonal unit cell (black line) and the primitive rhombohedral cell (blue lines), with four vanadium atoms (blue circles) in the centre. Adapted from [128]*

Crystal structure. The AFI phase is monoclinic and we will not concentrate on it. In the PI and PM phase the material has a corrundum structure with a rhombohedral unit cell (Figure 5.9). The most striking structural parameter signing the Mott transition is the vertical $V_1 - V_2$ - distance along the ***c***-direction between two adjacent vanadium atoms (Figure 5.9).

Table 5.1 shows the lattice parameters and $V_1 - V_2$ distances for different Cr concentrations in $(V_{1-x}Cr_x)_2O_3$. Despite the drop of the c parameter from PM phase V_2O_3 to the PI phase $(V_{1-x}Cr_x)_2O_3$, an increase of the $V_1 - V_2$ distance appears. This overcompensation effect is due to the position shift of the vanadium inside the crystal lattice.

Raman spectra. Figure 5.10 shows Raman spectra for the insulating phase $((V_{0.985}Cr_{0.015})_2O_3)$ and the metallic phase (V_2O_3) [130]. These measurements were performed on $30\,\mu\mathrm{m}$ single crystals.

Seven Raman-active modes are expected: two A_{1g} modes and five E_g

Table 5.1 *– Unit cell parameters and $V_1 - V_2$ distances for Cr-doped V_2O_3 [129].*

Sample	Phase	a (Å)	b (Å)	c (Å)	$d_{V_1-V_2}$
V_2O_3	PM	4.95	4.95	14.00	2.697
$(V_{0.989}Cr_{0.01})_2O_3$	PI	4.99	4.99	13.93	2.747
$(V_{0.972}Cr_{0.028})_2O_3$	PI	4.99	4.99	13.91	2.747
$(V_{0.944}Cr_{0.056})_2O_3$	PI	5.01	5.01	13.89	2.747

modes. Two A_{1g} modes and three E_g modes have been identified. The Raman signatures of undoped metallic and Cr-doped Mott insulator V_2O_3 are rather similar which is expected since they are isostructural. Cr doping is accompanied by an increase of the frequencies ω by several cm^{-1} (see Figure 5.10). The biggest shift is for A_{1g} modes at $246\,\mathrm{nm}$ and $501\,\mathrm{nm}$. We can also see that the intensity of the E_g mode at $234\,\mathrm{nm}$, dramatically decreases in Cr-doped V_2O_3.

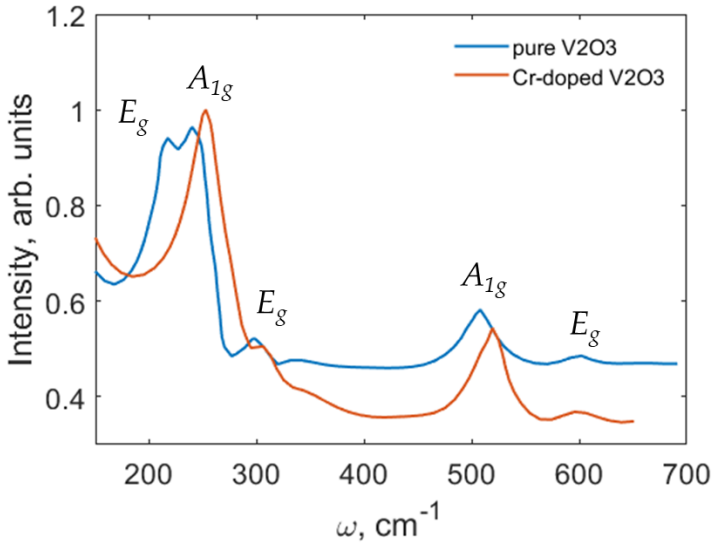

Figure 5.10 *– Raman scattering spectrum of pure V_2O_3 (metallic phase) and $(V_{0.985}Cr_{0.015})_2O_3$ (insulating phase). Adapted from [130].*

Optical properties. Reflectance measurement on differently doped $(V_{1-x}Cr_x)_2O_3$ single crystals in their various phases were performed by Lo Vecchio et al. [127]. Pure V_2O_3 is in its metallic phase at $T = 300\,\mathrm{K}$ and shows significantly higher reflectance in mid-infrared region compared to Cr-doped samples, which are in the insulating phase at room temperature. The reflectance change of $25\,\%$ can be an indication of insulator-to-metal transition.

Because we are looking at our sample with optical methods in Vis region, we should look at its optical properties in these wavelength range. Our pump wavelength $(800\,\mathrm{nm})$ and Raman probe measurements $(785\,\mathrm{nm})$ have the same penetration depth $(\sim 60\,\mathrm{nm})$. There is a slight difference $(\text{about } 10\,\mathrm{nm})$ in penetration depth for these wavelengths for insulating and metallic phases, but we can most probably neglect it.

One way of controlling IMT in Cr-doped V_2O_3 is to apply a static pressure. When the crystal volume is compressed, two vanadium atoms get closer to each other and the gap between two Hubbard bands becomes smaller, thus the material becomes more metallic. This process is always reversible: with releasing the pressure the system goes back to its initial insulating phase. This material has been chosen for the study of non-linear SAWs that will be discussed in the next section.

5.3.1 Non-linear surface acoustic wave observation

Samples. We performed experiments on samples of $(V_{0.95}Cr_{0.05})_2O_3$ thin films of $100\,\mathrm{nm}$, $150\,\mathrm{nm}$ and $250\,\mathrm{nm}$ thickness deposited on a sapphire substrate. These films consist of nanocrystals with average size of $30\,\mathrm{nm}$ and were provided by research group 'Physics of materials and nanostructures' at Jean Rouxel Institute of Materials in Nantes.

For characterization of the initial state of our samples we check the Raman spectrum on each of them (Figure 5.11). Raman spectrum of the non-perturbed surface of the deposited thin films indicate two main peaks: an intense A_{1g} at $250\,\mathrm{cm}^{-1}$ which corresponds mostly to a stretching mode of the $V_1 - V_2$ atom and a weaker peak A_{1g} at $516\,\mathrm{cm}^{-1}$. We observed a shift of A_{1g} at $250\,\mathrm{cm}^{-1}$ between pure metal (V_2O_3 without chromium). A small peak at $413\,\mathrm{cm}^{-1}$ which is clearly observed for a very thin sample of $100\,\mathrm{nm}$ corresponds to the peak from the sapphire substrate. A_{1g} peaks position remains the same for all samples regardless the thickness which confirms

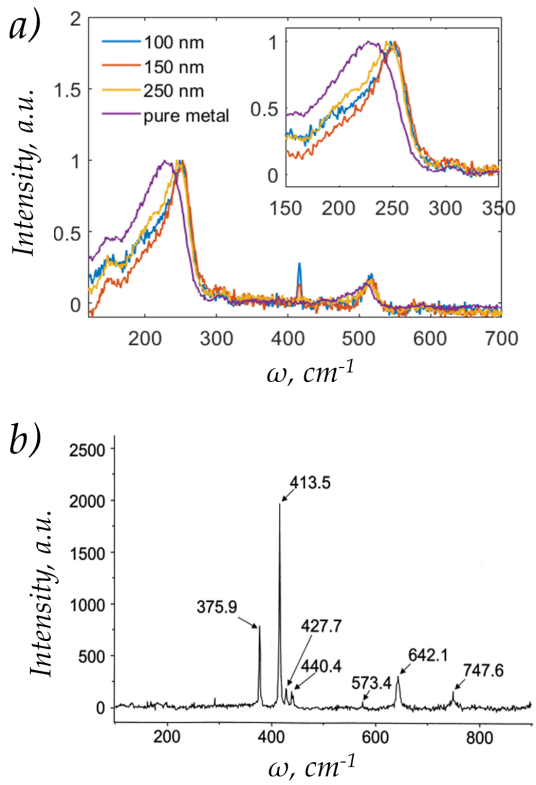

Figure 5.11 *– Raman spectra of:* ***a****) different thickness of* $(V_{0.95}Cr_{0.05})_2O_3$ *thin films deposited on a sapphire substrate. Insert graph illustrates the Raman shift for selected* A_{1g} *peak; b) sapphire substrate* [131].

that all samples are in the insulating phase. We will look at the shift of the Raman peak A_{1g} as an indication of creation of the metallic phase.

Experiment. Generation of SAWs and observation of its propagation were done in reflection configuration of single shot experiment, previously described in Chapter 3. We used a *Solstice @ Spectra Physics* laser system: $300\,\mathrm{ps}$, $800\,\mathrm{nm}$ laser pulse was used for the excitation and $150\,\mathrm{fs}$, $400\,\mathrm{nm}$ laser pulse was used for SAW observation. Black-and-white CCD camera was used to record images at the same time delay of $15\,\mathrm{ns}$ but for different pump fluences. Diameter of the excitation ring was $200\,\mu\mathrm{m}$ width $10\,\mu\mathrm{m}$.

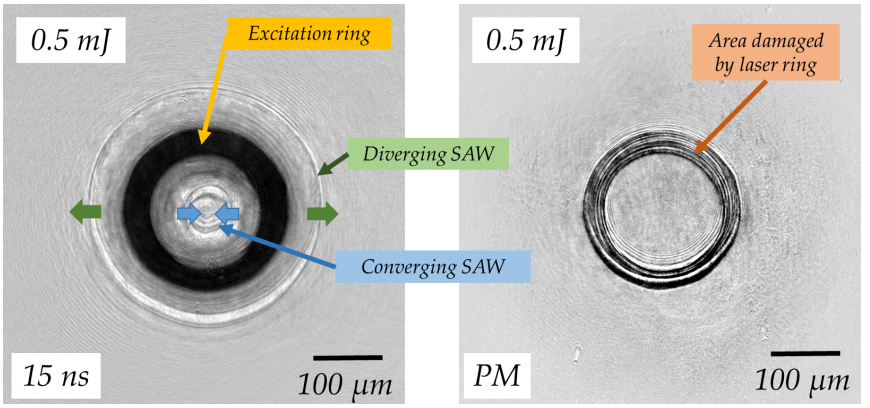

Figure 5.12 *– Representative image showing shock wave propagation on* $(V_{0.95}Cr_{0.05})_2O_3$ *thin film sample (left). This image was recorded at the laser energy of* $0.5\,\mathrm{mJ}$ *and at time delay of* $15\,\mathrm{ns}$*. Post-mortem image of 'shocked' region is displayed on the right.*

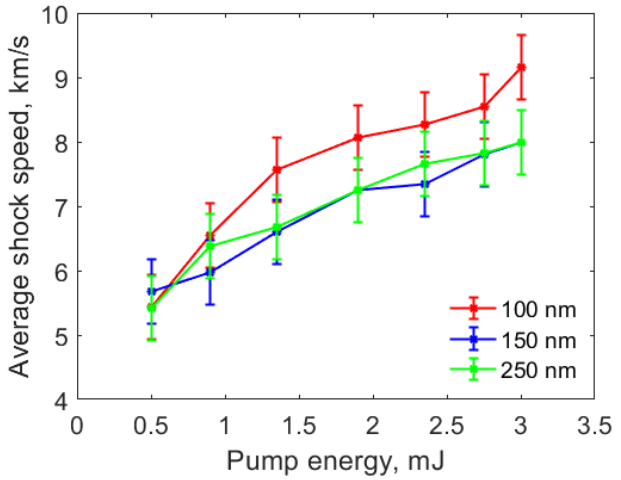

Figure 5.13 *– SAW speed of the diverging wave as a function of the pump fluence for different sample thickness. The speed of the generated SAW does not depend on the thickness of the sample because it is determined by the substrate.*

Figure 5.12 illustrates an image of the $(V_{0.95}Cr_{0.05})_2O_3$ sample surface. We clearly observe diverging and converging SAWs on the image recorded at the $15\,\mathrm{ns}$ delay. Each shot causes permanent damage to the sample surface delaminated by the ring-focus. Post-mortem image shows the area that was modified due to SAW propagation. At a low pump energy, like $0.5\,\mathrm{mJ}$, the only damage is observed at the laser ring region. We will look closer at this region for post-mortem surface analysis.

We can estimate the SAW speed by knowing the time delay and the propagation distance. As we can see, even for low pump fluence at $15\,\mathrm{ns}$, inner SAW is almost focalized at the centre of the ring. At high fluence it was difficult to determine the speed of the converging wave. The one we clearly observe is the divergent wave. We can estimate its speed which is surely lower than the one of the converging wave. Figure 5.13 shows SAW speed dependence on pump fluence. In such configuration the wave that we observe is the wave that propagates at the interface between V_2O_3 thin film and sapphire substrate, the so-called Stoneley wave (see Chapter 2). Because V_2O_3 is extremely thin compared to the SAW wavelength in the order of $10\,\mu\mathrm{m}$, the characteristic speed and pressure of this surface wave are determined by the sapphire substrate. The speed of the surface acoustic waves on sapphire is $5.97\,\mathrm{km/s}$ [132]. Our calculation of the diverging SAW speed shows a non-linear dependence on pump fluence that indicates a non-linear behaviour of the waves. Once again, the wave we observe is non-linear surface acoustic wave that propagates at the interface between the film and the substrate.

5.3.2 Post-mortem analysis

Figure 5.14 shows a 3D tomographic reconstructed image of the surface height of the 'shocked' region for the $250\,\mathrm{nm}$ $(V_{0.95}Cr_{0.05})_2O_3$ film on sapphire. The image indicates the laser ablated region at the laser ring (blue zone) and modification of surface morphology due to the propagating SAW. Depending on the pump fluence used for SAW generation, the surface morphology changes dramatically. For example, the Figure 5.14 (a), that correspond to a weak pump energy, shows a tiny modification of surface color at laser ring. At high pump fluence, all internal region of the laser ring is modified as it is shown in Figure 5.14(b). Region near, the excitation ring also shows a height changes that can happen due to ablation

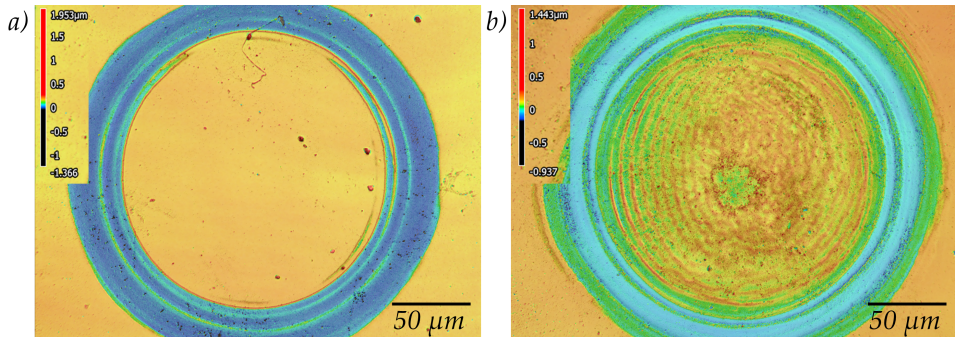

Figure 5.14 *– Optical tomographic images of shocked sample of* $250nm$ *Cr-doped* V_2O_3 *thin film for excitation fluences of* ***a***) $0.9\,\mathrm{mJ}$ *and* ***b***) $3\,\mathrm{mJ}$*. Color indicates the height of the surface.*

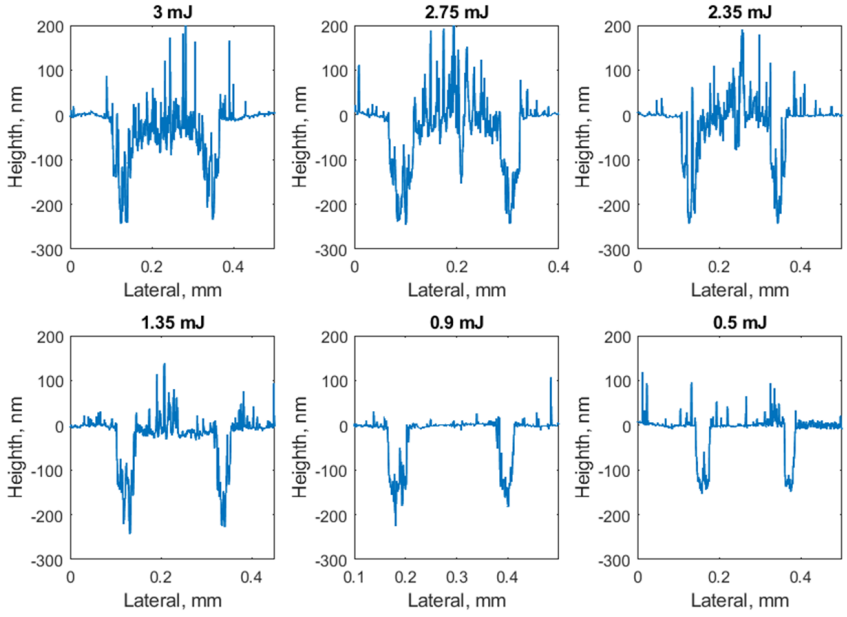

Figure 5.15 *– Measured profilometry of the* $250\,\mathrm{nm}$ *thin film of Cr-doped* V_2O_3*, shocked at different pump energies.*

process, but more importantly we will examine only the region near the centre of the ring at the acoustic focus.

We have performed profilometry measurements of the 'shocked' regions as well. We have looked at the topography of the sample surface along the diameter of the laser ring. Results presented in Figure 5.15 indicate a dramatic change on the inner part of the laser ring at high pump fluence. We observed creation of periodic peaks on the surface that are radially concentrated. At high fluence we also observe formation of a crater at the centre of the laser ring due to high pressure at the acoustic focus. Conversely, low pump fluence does not change the surface morphology and sample surface remains unperturbed. Profilometry measurements confirms that ablation process used for SAW excitation completely removes the thin film from the substrate.

As it was mentioned above, we examine the Raman spectrum in order to track a shift for the peak A_{1g} at $250\,\mathrm{cm}^{-1}$ in the insulating phase. We scanned the 'shocked' region using a Raman Microscope. Laser wavelength for Raman Microscope was $785\,\mathrm{nm}$ with spatial resolution of $1\,\mu\mathrm{m}$.

Figure 5.16 shows an optical image of the 'shocked' region that was taken at $3\,\mathrm{mJ}$ pump pulse. The color circles indicate the positions at which the corresponding Raman spectra were recorded at the vicinity of the A_{1g} peak at each spatial position. Pristine (unperturbed) spectrum was taken on the outside position and it correlates with initial Raman spectrum, shown above. We clearly observe a shift of about $18\,\mathrm{cm}^{-1}$ for all internal positions. This leads us to the conclusion, that the inner region is transformed from the initial insulating phase to the metallic phase. This change is obviously permanent (non-volatile). At low fluence of $0.9\,\mathrm{mJ}$ (Figure 5.17) we observe A_{1g} peak shift just in the centre of the laser ring. Profilometry shows no damage or material removing at the centre of the ring. Therefore, focalization of weak SAW (that leads to amplification) is enough to initiate permanent switching from insulator to metal.

If we analyse the Raman measurements done on a sample of $150\,\mathrm{nm}$ of $(V_{0.95}Cr_{0.05})_2O_3$ thin film on sapphire (Fig.5.18), we observe almost the same behaviour. The difference here is that the transited region is clearly seen on the optical image: it is located close to the ring centre and is separated from laser irradiated region by non-transformed region. If we compare the Raman peak A_{1g} for the pristine position (Figure 5.18, blue) and

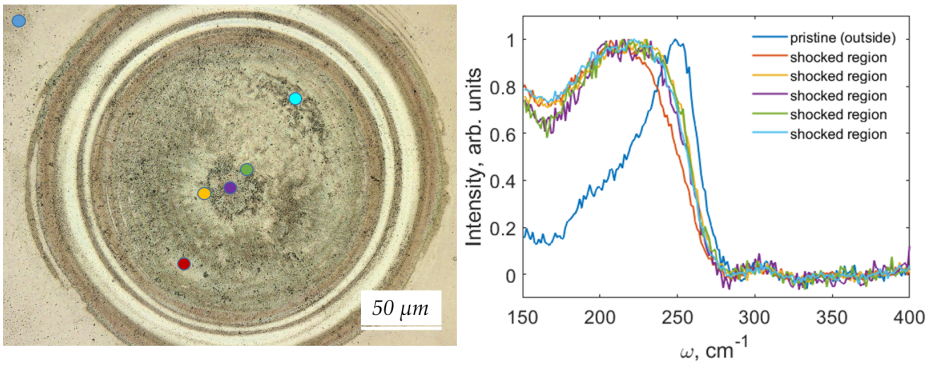

Figure 5.16 *– Post-mortem optical image of the 'shocked' sample region of* $250\,\mathrm{nm}$ *Cr-doped* V_2O_3 *thin film obtained at* $3\,\mathrm{mJ}$ *pump energy is presented on the left image. Right graph indicates a position of* A_{1g} *Raman peak for different positions at the sample surface, marked with different color circles.*

the same from inner non-transformed region (Fig. 5.18, green), there is no shift. Instead, on the central part for which on the optical image has a different color, we clearly observe a shift for this peak of about $18\,\mathrm{cm}^{-1}$ (Figure 5.18, red). This leads us to a conclusion that only the central part has trans-

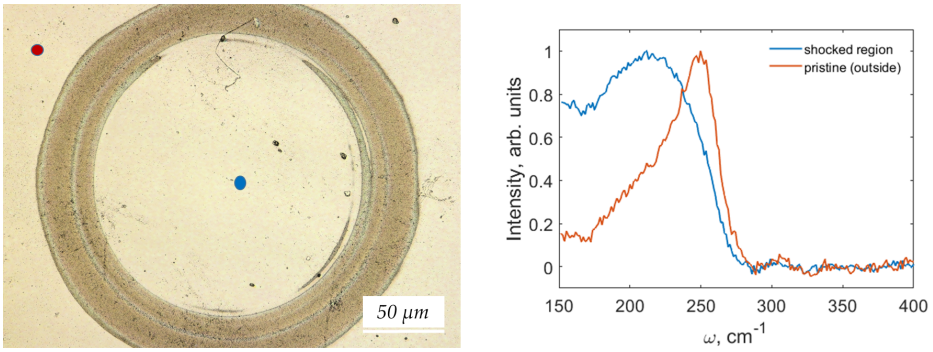

Figure 5.17 *– Post-mortem optical image of the 'shocked' region of* $250\,\mathrm{nm}$ *thin film obtained with* $0.9\,\mathrm{mJ}$ *pump energy (left). Right graph indicates a position of* A_{1g} *Raman peak for different positions at the sample surface, marked with different color circles.*

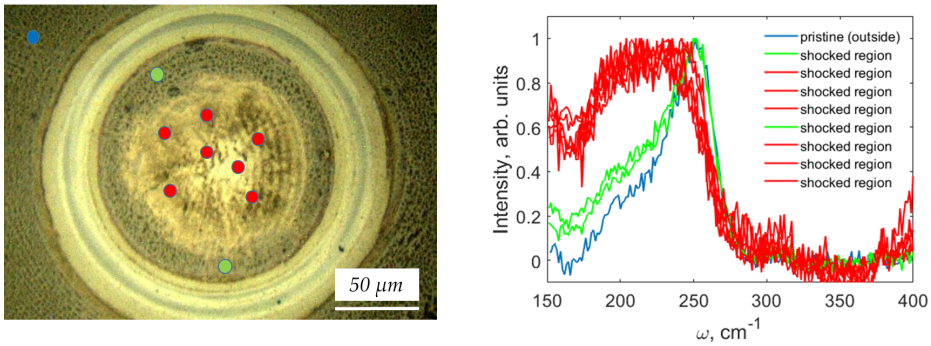

Figure 5.18 – *Post-mortem optical image of a 'shocked' regions of* $150\,\mathrm{nm}$ *thin film of* $(V_{0.95}Cr_{0.05})_2O_3$ *obtained at* $3\,\mathrm{mJ}$ *pump energy (left). Right graph indicates a position of* A_{1g} *Raman peak for different positions at the sample surface, marked with different color circles.*

formed from insulator to metal phase. As we can see, the A_{1g} peak shift for the $18\,\mathrm{cm}^{-1}$ in cases of $250\,\mathrm{nm}$ and $150\,\mathrm{nm}$ sample thickness (SAWs were generated with the same fluence). This means that thickness of the sample does not influence on the phase transition.

One can notice not only change in the Raman peak position but also change in its form. This spectrum change can be explained as following. In the $150-280cm^{-1}$ range, V_2O_3 and $(V_{1-x}Cr_x)_2O_3$ have two Raman modes (Figure 5.19): one E_g mode around $210-220cm^{-1}$ (red dashed line) and the A_{1g} mode around $250\,\mathrm{cm}^{-1}$ (blue dashed line). The intensity of the E_g mode is very low in the insulating phase, but strongly increases in the metallic one. This E_g mode can be seen in insulating phase only in polarized Raman measurements (Figure 5.19, bottom spectrum). In the case of unpolarized Raman spectrum (or Raman measured on a polycrystal film like in our case), the mode is much broader in the metallic state, because it is actually the sum of two peaks of similar intensities. That's why we see not only shifting of the peak position but also broadening of the A_{1g} peak.

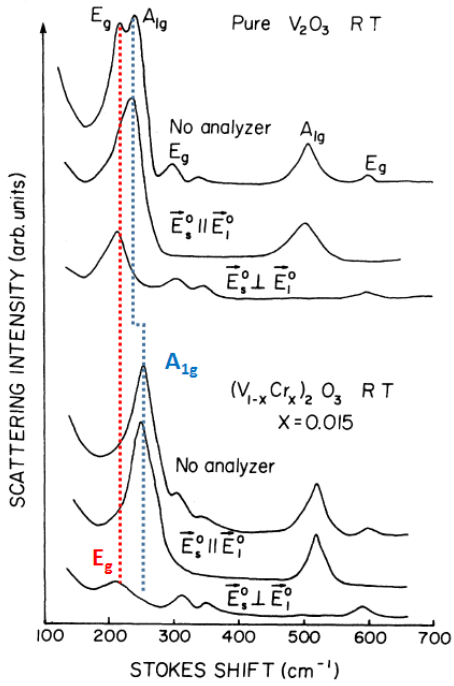

Figure 5.19 *– Raman scattering spectrum of pure V_2O_3 (metallic phase) and $(V_{0.985}Cr_{0.015})_2O_3$ (insulating phase) [130].*

5.3.3 Discussion

Our experiments have shown a creation of a metallic phase due to the propagation of non-linear surface acoustic waves. From static pressure measurements, we know from literature that Cr-doped vanadium oxide undergoes an isostructural insulator to metal transition at around $1.5\,\mathrm{GPa}$ - $2\,\mathrm{GPa}$ for sample with $5\,\%$ of chromium (see phase diagram Figure 5.20). However, the transition is volatile and returns to its initial state when the static pressure is released. In our experiments, under non-linear SAW influence, the transition becomes permanent. This surprising result leads to a new important question: what is the mechanism driving non-volatile transition?

It is known that under high strain, either extensive or compressive, duc-

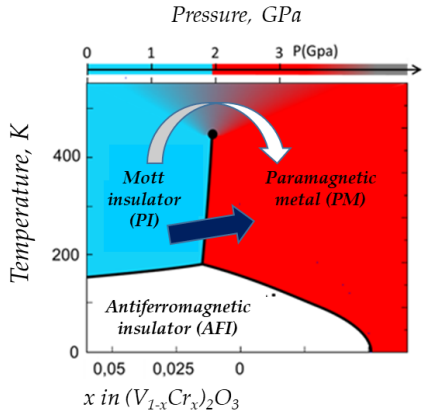

Figure 5.20 *– Phase diagram of V_2O_3 compound. White line indicates transition from PI to PM by passing through crossover region above critical point while blue line indicates direct isostructural IM transition.*

tile materials enter into plastic domain. Unlike the elastic domain where the macroscopic deformation under strain is cancelled as soon as the strain stops, in plastic domain, the mechanical changes are not reversible. In this plastic regime, atomic planes can slide and create dislocations. The elastic modulus or the frequency of the Raman mode, which characterizes the stiffness of the chemical bonds, are kept unchanged by a plastic deformation.

To explain our shock-wave-driven irreversible transition, an additional ingredient is required. A possible picture is that the convergence of surface acoustic waves generates a pressure high enough for Cr-doped V_2O_3 to pass from insulator to metallic state but also to bypass Hugoniot elastic limit (HEL). In this plastic regime, one might argue that a high density of dislocations is created, which could act as traps preventing the metallic compressed domain to relax to their Mott insulator thermodynamic equilibrium state. In other words, the key ingredient to explain this shock-wave-driven irreversible IMT could be a compression effect allowing to cross the first order Mott line; and a plastic deformation creating dislocation preventing the compressed domain to relax and hence maintaining the metallic state. Temperature rise that appears due to non-linear SAW propagation

will also affect the processes involved in the insulator-to-metal transition observed in this section. If the temperature change is small, we observe a direct transition from paramagnetic insulator to paramagnetic metal (1st order transition without symmetry change, indicated in Figure 5.20, blue line). But if temperature change is high enough to pass the critical point at $450\,\mathrm{K}$, the final metallic state can be obtained by passing through crossover region (Figure 5.20, white line). But even in this case, the temperature will play insignificant role in the transition process, because by simple heating of an insulating phase we can not obtain the metallic phase.

5.4 Conclusion

In this chapter we demonstrate the possibility to initiate IMT with converging non-linear surface acoustic waves propagating on the surface of two correlated compounds: the strongly correlated compound Ti_3O_5 and the canonical Mott insulator $(V_{1-x}Cr_x)_2O_3$.

Laser induced converging SAW were generated at the sample surface of both compounds. In case of Ti_3O_5, the sample was a pressed pellet without any substrate. Thus, the surface acoustic waves were generated and guided by the material itself. Due to high dispersivity of the sample, it was hard to observe a SAW front. White light microscopy and image treatment indicate the formation of a pure semiconductor phase. The further investigation should be done on samples with different morphologies, for example, thin film.

In case of Cr-doped V_2O_3 thin films, the SAW is generated and propagates at the interface between the thin film and the substrate. Its properties is determined by the substrate because of the small thickness of the film. Time-resolved imaging at different pump fluences indicates a non-linear character of the SAW that makes it a shock-like wave. Post-mortem analysis of the 'shocked' regions show destruction of the sample surface at high fluences. It also indicates a permanent Mott insulator-to-metal transition. A possible explanation of the permanent character of the transformation might involve plastic deformation and stabilization of compressed domains by dislocation. However, further investigation, like X-ray diffraction of 'shocked' regions are obviously necessary to clarify the physical mechanism behind this transition. X-ray diffraction measurements give us the

information of the unit cell parameters that are unique for each phase in both cases: Ti_3O_5 and Cr-doped V_2O_3. Also, in case of the vanadium oxide, one can imagine the resistivity or conductive AFM measurements to find out the conductivity difference between undisturbed and 'shocked' regions. The main difficulty for this kind of experiments is the small size of the transformed region that requires micro-metric resolution.

General conclusion

The present thesis is focused on the study of phase transitions induced by converging shock waves in two types of materials: Mott insulators and spin-crossover. An all-optical setup for generation and observation of converging shock waves was built. The used technique of shaping a laser beam in a ring pattern allows us to directly generate converging shock waves and spatially separate laser-influenced and shock-influenced regions. This permits to study changes induced only by shock wave propagation.

Mott insulators are a family of materials that undergo a transition with significant volume change without symmetry change. In this thesis, we observed a successful permanent insulator-metal transition in two compounds: Ti_3O_5 and V_2O_3 induced by converging non-linear surface acoustic wave. In the case of the first one, we observed a transition from metal to a semiconductor at the inner part of the laser ring. This change was detected by simple RGB image analysis. The observation of non-linear SAW was less successful because of the high inhomogeneity of the sample. In contrast, the surface of Cr-doped V_2O_3 thin films has a good optical quality, so we clearly observe the SAW propagation. Images of propagation reveal a non-linear character of the generated SAW. The samples reside initially in the insulating phase and postmortem investigation of 'shocked' regions shows a dramatic change of the sample's surface after propagation of the shock wave at high pump fluences, including the formation of a crater at the centre of the laser ring. Raman measurements at the inner region of the laser ring, both at high and low fluences, indicate the formation of a permanent metallic phase. We demonstrate a non-volatile nature of such transition and provided a tentative explanation of the stabilizing mechanism. Future X-Ray diffraction measurements will provide insights into the structure of

the "shocked" regions, whether they bear signatures of long-range metallic order.

We successfully generated shock waves in a thin layer of $Fe(NH_2 - trz)_3](Br)_2$ spin-crossover suspension. The experimentally determined maximal shock had an amplitude of $15\,\mathrm{GPa}$, and a speed of $3\,\mathrm{km/s}$. Unfortunately, we did not observe any indication of phase transitions due to existing experimental conditions. Performed experiments indicate the importance of imaging by transition sensitive wavelength (here $300\,\mathrm{nm}$). Another non-trivial aspect was the stability of the sample during the experiment. In the case of $Fe(NH_2 - trz)_3](Br)_2$ suspension, the sample behaviour at high temperature precluded further investigations due to permanently altered sample morphology. However, a sibling compound, $[Fe(HB(tz)_3)_2]$, that was successfully deposited in the form of the thin film is more stable and promising for future investigations. Preliminary investigations indicate a huge potential of this compound, but the experimental conditions need modifications due to low absorption. Absorption can be dramatically increased by lithographic deposition of a gold ring on the $[Fe(HB(tz)_3)_2]$ film. The new attempts are ongoing. Another important parameter is the duration of the shock pulse: as the spin states are separated by local energy barriers a certain time is required to overcome these barriers. Thus, the duration of dynamic pressure should be in the time range of such a process.

This work did not address all questions about the driving mechanisms and the nature of studied transitions, but it paved the way for further investigations of different compounds that exhibit phase transition with significant volume change. Laser-induced shock waves are very promising new stimuli for driving such transitions on ultrafast timescales at the nanometric level. In this work specifically, we shed light on how irreversible IMT are generated by structural, rather than electronic excitation. In the case of spin-crossover systems, despite a limited amount of experimental data, we explored a range of control parameters, sample morphologies and imaging conditions that will facilitate the ongoing and future studies.

Annexe

Scripta Materialia 158 (2019) 42–45

Contents lists available at ScienceDirect

Scripta Materialia

journal homepage: www.elsevier.com/locate/scriptamat

Glass fracture by focusing of laser-generated nanosecond surface acoustic waves

David Veysset [a,b,*], Steven E. Kooi [a], Ryadh Haferssas [a,c], Mostafa Hassani-Gangaraj [d], Mohammad Islam [a,c], A.A. Maznev [a,b], Yevheniia Chernukha [e], Xiaoguang Zhao [f], Keiichi Nakagawa [g,i], Dmitro Martynowych [a,b], Xin Zhang [f], Alexey M. Lomonosov [h], Christopher A. Schuh [d], Raul Radovitzky [a,c], Thomas Pezeril [d], Keith A. Nelson [a,b]

[a] Institute for Soldier Nanotechnologies, Massachusetts Institute of Technology, Cambridge, MA 02139, USA
[b] Department of Chemistry, Massachusetts Institute of Technology, Cambridge, MA 02139, USA
[c] Department of Aeronautics and Astronautics, Massachusetts Institute of Technology, Cambridge, MA 02139, USA
[d] Department of Materials Science and Engineering, Massachusetts Institute of Technology, Cambridge, MA 02139, USA
[e] Institut Molécules et Matériaux du Mans, UMR CNRS 6283, Université du Maine, 72085 Le Mans, France
[f] Department of Mechanical Engineering, Boston University, Boston, MA 02215, USA
[g] Department of Bioengineering, The University of Tokyo, Tokyo 113-8656, Japan
[h] Prokhorov General Physics Institute RAS, Moscow, Russia
[i] Department of Precision Engineering, The University of Tokyo, Tokyo 113-8656, Japan

ARTICLE INFO

Article history:
Received 10 July 2018
Accepted 14 August 2018
Available online 29 August 2018

Keywords:
Dynamic fracture
Surface acoustic waves
Interferometry
Glass

ABSTRACT

Dynamic fracture of borosilicate glass through focusing of high-amplitude nanosecond surface acoustic waves (SAWs) at the micron scale is investigated in an all-optical experiment. SAWs are generated by a picosecond laser excitation pulse focused into a ring-shaped spot on the sample surface. Interferometric images capture the SAW as it converges towards the center, focuses, and subsequently diverges. Above a laser energy threshold, damage at the acoustic focal point is observed. Numerical calculations help us determine the time evolution of the stress distribution. We find that the glass withstands a local tensile stress of at least 6 GPa without fracture.

The dynamic fracture of glassy materials is of great importance for a wide range of technologic applications, from cracked mobile device screens or car windshields hit by rocks on the road to the International Space Station's windows subjected to space debris impacts [1]. Glasses, despite being intrinsically among the strongest man-made materials, are vulnerable through their defects, which can reduce the static tensile strength by orders of magnitude [2]. While the theoretical tensile strength limit of silica glass is about 20 GPa [3], experimentally-measured static tensile strength can be as low as 0.1–0.2 GPa in bulk specimens [4]; in nanoscale specimens that sample few or no flaws much higher tensile strengths exceeding 10 GPa can be measured [5]. When dealing with high strain rate situations (e.g. an impact of a micro-meteorite on a spacecraft), static material properties offer only limited insight into materials resistance to crack initiation and propagation [6]. Dynamic fracture of silicate glasses on the microsecond time scale has been extensively studied in shock spallation experiments under plate [7–10] or laser-induced shock [11]. These measurements, in which spallation is caused by tensile stresses in release waves, reveal a much higher tensile strength under dynamic loading, typically in the few GPa range. For example, the reported spall strength of soda lime glass ranges from 2.2 to over 5 GPa [7,9,11]. The interpretation of tensile strength measurements in plate impact experiments is complicated by the fact that the material is initially subjected to compression; above ~4 GPa many studies report an apparent structural degradation under compression ("failure waves") [8–10,12–14], which reduces the subsequently measured tensile strength on release. It is evident that the dynamic strength of glass is not a material constant; rather, it depends on the duration of the tensile stress and on the entire loading history. Whereas laser shock experiments on metals such as aluminum and copper [15] indicate that under very short (sub-nanosecond) shock pulses, the spall strength approaches the theoretical limit for those materials, it remains an open and practically relevant question whether the theoretical limit can be approached for silicate glasses.

In this work, we describe a methodology for studying glass failure on the nanosecond time scale using focusing laser-generated surface acoustic waves (SAWs). High amplitude SAWs have already been

* Corresponding author at: Institute for Soldier Nanotechnologies, Massachusetts Institute of Technology, Cambridge, MA 02139, USA.
E-mail address: dveysset@mit.edu (D. Veysset).

https://doi.org/10.1016/j.scriptamat.2018.08.026
1359-6462/

proven capable of causing fracture in brittle materials [16,17]. In those prior works [16,17] fracture was caused by the formation of "surface shock waves" accompanied by a sharp increase of the stress at the surface; the measurements could only provide a lower bound estimate of the peak stress value. In a recent study [18], we proposed an alternative approach, based on focusing SAWs. The short SAW propagation distance (100 μm) prevents shock front formation, and the high stress that occurs where the SAWs are focused is essentially achieved in the linear elastic regime. These measurements are very different from traditional shock spallation studies in that the tensile phase of the SAW pulse lasts only a few nanoseconds and is not preceded by a significant precompression. In experiments on gold-coated glass, we observed failure of the gold coating and, at higher laser energies, of the glass substrate. However, the early failure of the gold layer prevented measurements of the SAW pulse profile at high amplitudes and complicated the interpretation of the observations of the glass damage. In the current work, we report experiments in a modified arrangement, wherein a gold coating is still used to generate SAWs but their focusing occurs on a bare glass substrate. Above a certain SAW amplitude threshold, glass failure at the focal point and the formation of a crater due to the ejection of the fractured material are observed. Numerical calculations matching experimentally measured displacement profiles in the focused SAW allow us to characterize the dynamics of the stress distribution in the sample.

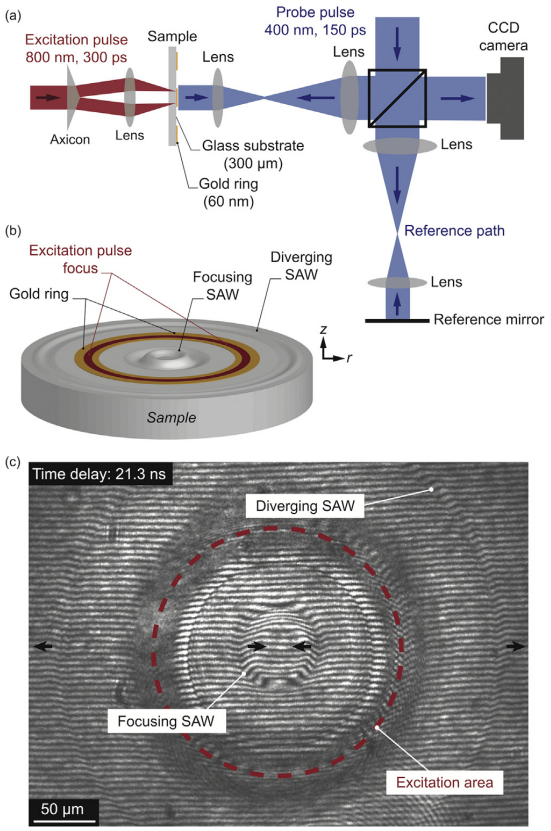

Fig. 1. (a) Experimental setup. The excitation beam is shaped as a ring with an axicon/lens combination. Interferometric imaging is achieved using a Michelson interferometer. (b) Schematic of the sample configuration. The excitation pulse is focused on the gold ring, generating focusing and diverging surface acoustic waves. (c) Interferometric image showing surface displacement caused by focusing and diverging SAWs. This image was taken for a laser energy of 0.25 mJ with a delay of 21.3 ns between the excitation and the probe pulses. Thedashed ring indicates the laser excitation area. Circular fringes appearing at the bottom of the image comes from a defect on one of the imaging optics. See supplementary material for images taken before laser excitation and post mortem.

The experimental setup, shown schematically in Fig. 1, follows the design developed by Veysset et al. [18]. A laser excitation pulse, derived from a Ti:sapphire amplifier, with a 300-ps duration, 800-nm wavelength and adjustable energy (from 0.15 mJ to 1.50 mJ), was focused onto the surface of a 300 μm-thick borosilicate glass substrate (D263 Schott) to ablate a 160 nm-thick metallic ring. The metallic ring, henceforth referred to as the gold ring, consisted of 10-nm chromium, in contact with the glass, and 150-nm gold. The gold ring had an inner diameter of 160 μm and an outer diameter of 240 μm (see supplementary material for sample fabrication). The laser focus was shaped as a 200 μm-diameter, 5 μm-wide ring using a 0.5° conical prism (axicon) and a 3 cm focal-length lens, as described by Pezeril et al. [19] and Veysset et al. [20,21] Multiple rings were fabricated on the same substrate and the sample was translated to move the laser focus to a new ring for each laser shot, with the laser focus and ring overlapping as in Fig. 1b each time. Imaging of the sample surface was achieved using a variably-delayed, 150-fs duration probe pulse reflected from the surface of the sample. The probe pulse, derived from the same amplifier system, was frequency-doubled to 400-nm wavelength. Interference fringes of equal thickness obtained using a Michelson interferometer configuration were recorded by a CCD camera.

For each laser shot, stress waves were produced following ablation—therefore destruction—of the metallic film and a single image was recorded with a set time delay between the excitation and the probe pulses. Because of the ring shape of the excitation, focusing and diverging surface waves were generated and propagated on the surface of the bare glass (see Fig. 1b and c). Bulk waves were also generated but were not imaged in the present configuration. As the surface was displaced under SAW propagation, the phase of the reflected pulse shifted (the phase shift is denoted as $\Delta\varphi$) causing fringes to shift on the CCD image (see Fig. 1c). By measuring the fringe shift, we could determine the corresponding out of plane surface displacement $u_z(r)$ through the relationship $u_z = \lambda\Delta\varphi/4\pi$, where $\lambda = 400\ nm$ is the probe pulse wavelength. After each shot, the sample was positioned to a new ring and different time delay and laser energy could be set.

We recorded images such as that shown in Fig. 1c for multiple time delays and laser energies and extracted the surface displacements along a ring diameter. More details regarding the image analysis can be found in Veysset et al. [18]. Fig. 2a presents surface displacement profiles showing the propagation of the focusing SAW for 7 delays at a laser energy of 0.25 mJ, corresponding to a laser fluence of 4.5 J/cm^2. The SAW focused around 30 ns after being generated and subsequently diverged. Fig. 2b shows the surface displacements obtained for a laser energy of 0.75 mJ. Around this laser energy, the image quality was degraded at longer times and the surface displacements closer to the focus or right after the focus could not be accurately extracted. Fig. 2c shows the peak-to-peak amplitude of the SAW taken at a delay of 12.7 ns for varying laser energies and shows that the SAW amplitude started to saturate at laser energies above 1 mJ.

In our previous work, with the same experimental design but with the sample surface uniformly coated with a gold film, the large amplitude of the SAW at the focal point caused delamination and damage of the film at low laser energy (~0.1 mJ) and glass substrate fracture at high laser energy (~2 mJ) [18]. The film damage obscured the imaging of the SAW at higher laser energies making it impossible to evaluate the absolute surface displacements leading to glass fracture. Here, with no metal film inside the ring, we observe surface displacements even at high laser energies and, after sample examination under laser-scanning confocal microscope and atomic force microscope, can confirm visible glass fracture at laser energies above 0.75 mJ. The substrate visibly fractured at the center in about 10% of the cases for a laser energy of 1.00 mJ and in 100% of the cases for a laser energy of 1.50 mJ (see Fig. 2c,

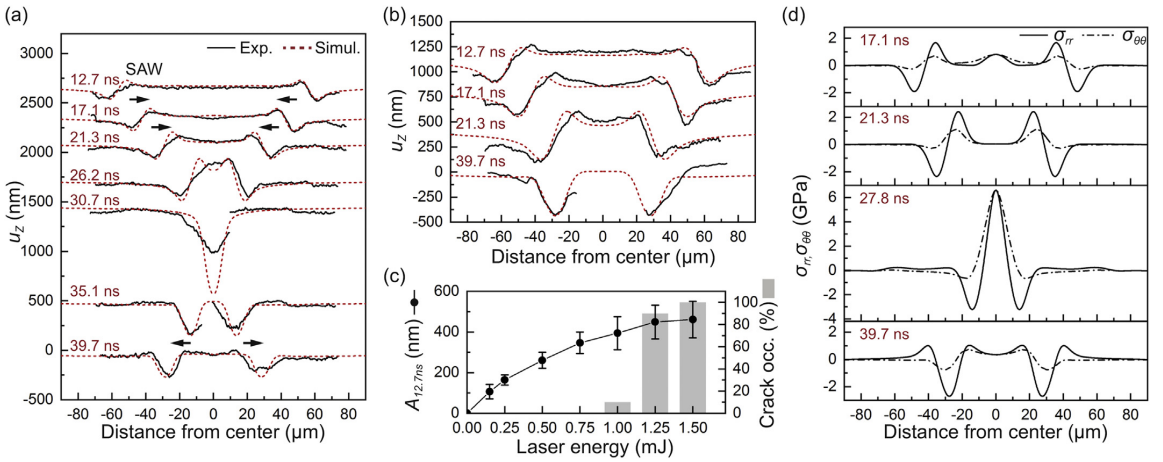

Fig. 2. (a–b) Experimental and simulated surface displacements, u_z, as a function of time delay for two laser energies: (a) 0.25 mJ and (b) 0.75 mJ. (c) (left axis) SAW peak-to-peak amplitude experimentally measured after a delay of 12.7 ns with varying laser energy. The data points represent the average between the left and right lobes of the SAW and taking into account different shots. The error bars represent the standard deviation on the peak-to-peak amplitude. (right axis) Visible occurrence, in % of observed cases, of glass fracture as a function of laser energy. (d) Simulated non-zero stresses σ_{rr} and $\sigma_{\theta\theta}$ at the sample surface ($z = 0$) corresponding to the last three simulated surface displacements shown in (b) and for the delay corresponding to the maximum tensile stress at the center (27.8 ns).

right axis). When visible damage was observed, a laser-scanning confocal microscope revealed a crater of about 10–20 μm in diameter and about 4–5 μm in depth, as shown for example in Fig. 3. In rare instances, the ejected piece of glass was found near the central pit (see Fig. 3b and the corresponding elevation profile in Fig. 3c). It is interesting to note that the removed piece is a single piece of glass. For all studied energies, we observed no damage between the laser excitation area and the central crater.

In order to estimate the stress levels that were reached through SAW focusing, we implemented a 2D axisymmetric finite element model (see supplementary material for more details on the model) and simulated the linear SAW propagation following a Gaussian distribution impulse at the laser focus position. The amplitude and the width of the initial pressure distribution were calibrated to match the experimentally-measured peak-to-peak amplitudes of the SAW for laser energies of 0.25 and 0.75 mJ. The simulated surface displacements and stresses σ_{rr} and $\sigma_{\theta\theta}$ at the surface are shown in Fig. 2a, b and d. The reasonable agreement between the experiments and the simulations confirms the linear propagation of the SAW. The good agreement after the focus is consistent with the absence of the visible damage.

As shown in Fig. 4a, at the focal point and at the surface of the sample ($r = 0, z = 0$), after the passage of the longitudinal surface skimming wave (SSWL), the material experienced a high level of tension, then a high level of compression, and finally a lower level of tension brought by the SAW. Fig. 4b and c show the principal stress profiles, σ_{rr} and σ_{zz}, at the center of focus, as a function of depth (with $z = 0$ being the surface of the substrate) for three delays 27.8, 31.7, and 35.1 ns, corresponding to the three stress extrema of the SAW. We assume that damage is initiated by the initial tensile phase of the SAW pulse at the sample surface, where the radial tensile stress is the highest. We note that during this initial tensile phase the surface velocity at the focal point is directed outwards, which can explain the ejection of the fractured material.

Despite a simulated equibiaxial tension as high as 6.6 GPa at the center of focus at the surface (Fig. 4b, depth $z = 0$) at a laser energy of 0.75 mJ, we observed no sign of failure of the substrate at this laser energy. It is well known that in a variety of materials the high strain rate strength can exceed the static strength by orders of magnitude [15,22–24] and the present value is higher than what has been previously reported in the literature for the dynamic fracture of glass. The high stress value can be justified by a combination of factors pertaining to the experimental method. First, the glass experienced an ultra-high strain rate, up to 10^8 s^{-1}, upon the passage of the nanosecond-duration SAW, which is shorter than the typical microsecond time

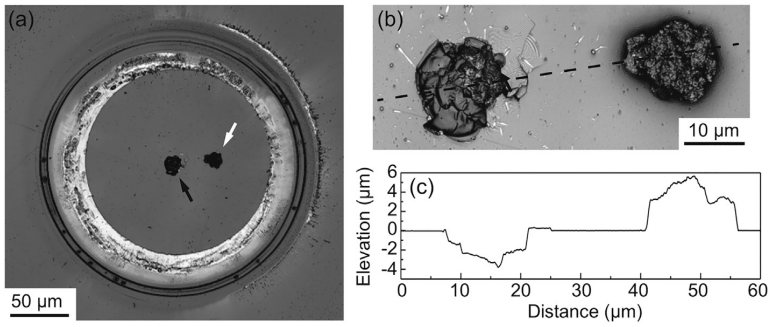

Fig. 3. Laser-scanning confocal microscope images of typical glass damage for a laser energy of 1.00 mJ. (a) Large view showing excitation location, parts of remaining gold film, and central crack. The black arrow points to the central crack and the white arrow to the removed piece. (b) Zoomed-in image of the central damage and corresponding delaminated piece. (c) Elevation profile along the dashed line shown in (b).

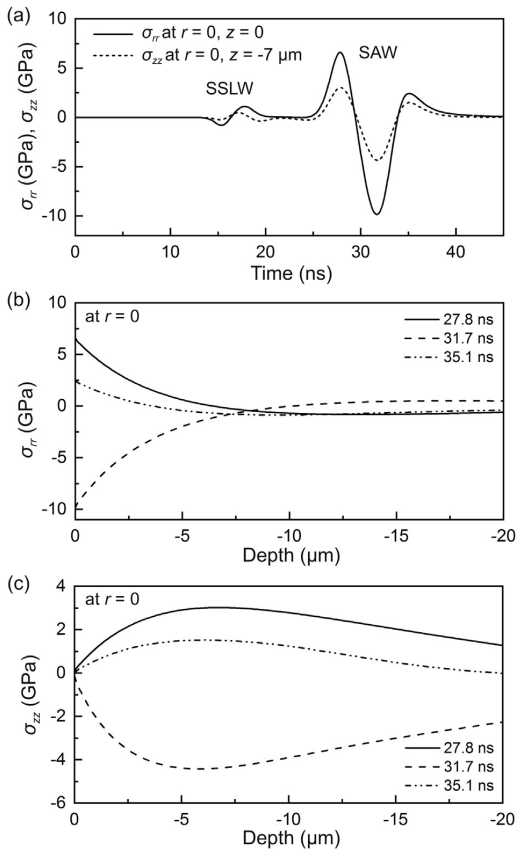

Fig. 4. (a) Non-zero principal stresses σ_{rr} (solid line) computed at the center of focus ($r = 0$) and at the surface ($z = 0$) and σ_{zz} (dotted line) at the center of focus ($r = 0$) and below surface ($z = 7$ µm, corresponding to the depth of maximum value) as a function of time. (b–c) Principal stresses, σ_{rr}, and σ_{zz}, at $r = 0$ for three delays, corresponding to stress extrema, as a function of depth for a laser energy of 0.75 mJ.

scale of spallation experiments. Second, in the present experiments, the initial tensile phase is not preceded by a compression (except of the much weaker SSLW), whereas in spallation experiments the pre-compression by an intense shock wave influences the spall strength [25,26]. Third, with the very small volume of material being loaded in the present experiments, there is a reduced possibility of surface defects being present, permitting a tensile strength approaching the theoretical limit [5]. Finally, as with more conventional methods, we cannot rule out the possibility that some degree of fracture has occurred at the nanoscale in any of our experiments, but leaves no visible trace with our methods of observation.

In summary, high stresses were locally attained using focusing laser-generated SAWs, and stress histories were determined from a combination of interferometric measurements and axisymmetric finite element simulations. We found that under nanosecond tensile loadings up to ~6 GPa with no pre-compression, no visible damage or fracture was observed on samples of glass. At higher excitation laser energies, we observed damage at the focal point in the form of a crater left by the fracture and ejection of a piece of material. The present method is applicable for a wide range of materials and opens prospects for ultra-high strain rate dynamic failure testing of novel materials with limited available volumes and for refining fracture models.

See supplementary material for sample fabrication, before-excitation and post-mortem images, laser-induced damage, simulation details, effects of non-linearity, temporal and spatial evolutions of the stress at the center of focus, and laser asymmetry considerations.

Acknowledgments

D.V. thanks Panagiotis Natsiavas for initial modeling efforts. This material is based upon work supported in part by the U. S. Army Research Office through the Institute for Soldier Nanotechnologies, under Cooperative Agreement Numbers W911NF-13-D-001 and W911NF-18-2-0048 and by the Office of Naval Research, Grant No. N000141512694. The authors acknowledge financial support from CNRS (Centre National de la Recherche Scientifique) under grant Projet International de Coopération Scientifique. C.A.S., K.A.N, and M.H.-G. acknowledge support from the U.S. Department of Energy, Office of Science, Office of Basic Energy Sciences, Division of Materials Sciences and Engineering under Award DE-SC0018091. X. Z and X. Z. acknowledge support by the National Science Foundation (grant number ECCS-1309835)

Appendix A. Supplementary data

Supplementary data to this article can be found online at https://doi.org/10.1016/j.scriptamat.2018.08.026.

References

[1] E. Christiansen, J. Hyde, R. Bernhard, Adv. Sp. Res. 34 (2004) 1097–1103.
[2] L. Wondraczek, J.C. Mauro, J. Eckert, U. Kühn, J. Horbach, J. Deubener, T. Rouxel, Adv. Mater. 23 (2011) 4578–4586.
[3] S.M. Wiederhorn, J. Am. Ceram. Soc. 52 (1969) 99–105.
[4] Schott Technical Glasses, Physical and Technical Properties, www.us.schott.com.
[5] G. Brambilla, D.N. Payne, Nano Lett. 9 (2009) 831–835.
[6] J.E. Field, S.M. Walley, W.G. Proud, H.T. Goldrein, C.R. Siviour, Int. J. Impact Eng. 30 (2004) 725–775.
[7] Z. Rosenberg, D. Yaziv, S. Bless, J. Appl. Phys. 58 (1985) 3249–3251.
[8] Z. Rosenberg, Y. Ashuach, E. Dekel, Int. J. Impact Eng. 35 (2008) 820–828.
[9] H.D. Espinosa, Y. Xu, N.S. Brar, J. Am. Ceram. Soc. 80 (2005) 2061–2073.
[10] G.I. Kanel, S.V. Razorenov, V.E. Fortov, Shock-Wave Phenomena and the Properties of Condensed Matter, 2004.
[11] M.J. Davis, Int. J. Appl. Glas. Sci. 7 (2016) 364–373.
[12] G.F. Raiser, J.L. Wise, R.J. Clifton, D.E. Grady, D.E. Cox, J. Appl. Phys. 75 (1994) 3862–3869.
[13] S.V. Rasorenov, G.I. Kanel, V.E. Fortov, M.M. Abasehov, High Pressure Res. 6 (1991) 225–232.
[14] N.K. Bourne, J.C.F. Millett, J.E. Field, Proc. R. Soc. Lond. A Math. Phys. Sci. 455 (1999) 1275–1282.
[15] E. Moshe, S. Eliezer, E. Dekel, A. Ludmirsky, Z. Henis, M. Werdiger, I.B. Goldberg, N. Eliaz, D. Eliezer, J. Appl. Phys. 83 (1998) 4004–4011.
[16] A.M. Lomonosov, P. Hess, Phys. Rev. Lett. 89 (2002), 095501. .
[17] G. Lehmann, A.M. Lomonosov, P. Hess, P. Gumbsch, J. Appl. Phys. 94 (2003) 2907.
[18] D. Veysset, A.A. Maznev, I.A. Veres, T. Pezeril, S.E. Kooi, A.M. Lomonosov, K.A. Nelson, Appl. Phys. Lett. 111 (2017), 031901. .
[19] T. Pezeril, G. Saini, D. Veysset, S. Kooi, P. Fidkowski, R. Radovitzky, K.A. Nelson, Phys. Rev. Lett. 106 (2011) 214503.
[20] D. Veysset, T. Pezeril, S. Kooi, A. Bulou, K.A. Nelson, Appl. Phys. Lett. 106 (2015) 161902.
[21] D. Veysset, U. Gutiérrez-Hernández, L. Dresselhaus-Cooper, F. De Colle, S. Kooi, K.A. Nelson, P.A. Quinto-Su, T. Pezeril, Phys. Rev. E 97 (2018), 053112. .
[22] E. Moshe, S. Eliezer, Z. Henis, M. Werdiger, E. Dekel, Y. Horovitz, S. Maman, I.B. Goldberg, D. Eliezer, Appl. Phys. Lett. 76 (2000) 1555.
[23] C. Huang, G. Subhash, J. Mech. Phys. Solids 51 (2003) 1089–1105.
[24] W. Chen, G. Ravichandran, J. Mech. Phys. Solids 45 (1997) 1303–1328.
[25] J. Cagnoux, F. Longy, J. Phys. Colloq. 49 (1988) C3-3-C3-10.
[26] R.L. Whelchel, T.H. Sanders, N.N. Thadhani, Scr. Mater. 92 (2014) 59–62.

References

[1] M. Morrisey and L. Mastin. *Vulcanian eruptions in Encyclopedia of Volcanoes, H. Sigurrsson*. 2000.

[2] Allen J.S. Waite G.P. Medici E.F. "Modeling shock waves generated by explosive volcanic eruptions". In: *Geophysical Research Letters* 41.2 (2014), pp. 414–421.

[3] Ch. K. Materese et al. "Ice chemistry on outer solar system bodies: elecron radiolysis of N2, CH4 and co-containing ices". In: *The Astrophysical Journal* 812.2 (Oct. 2015), p. 150.

[4] D. Nna-Mvondo et al. "Experimental impact shock chemistry on planetary icy satellites". In: *Icarus* 194.2 (2008), pp. 822 –835. ISSN: 0019-1035.

[5] E. A. Silber et al. "Physics of meteor generated shock waves in the Earth's atmosphere – A review". In: *Advances in Space Research* 62.3 (2018), pp. 489 –532. ISSN: 0273-1177.

[6] P. Krehl. *History of shock waves, explosions and impact: a chronological and biographical reference*. Springer Science & Business Media, 2008.

[7] Richard Courant and Kurt Otto Friedrichs. *Supersonic flow and shock waves*. Vol. 21. Springer Science & Business Media, 1999.

[8] M. Boustie et al. "Laser Shock Waves: Fundamentals and Applications". In: *1st international symposium on Laser Ultrasonics*. Montreal, France, July 2008.

[9] Utkin A.V. Razorenov S.V. et al. "Spallation in solids under shock-wave loading: analysis of dynamic flow, methodology of measurements, and constitutive factors". In: *High-Pressure Shock Compression of Solids II*. Springer, 1996, pp. 1–24.

[10] A. Telang et al. "Effect of temperature on microstructure and residual stresses induced by surface treatments in Inconel 718 SPF". In: *Surface and Coatings Technology* 344 (2018), pp. 93 –101. ISSN: 0257-8972.

[11] S. K. Shrivastava and Kailash. "Shock wave treatment in medicine". In: *Journal of Biosciences* 30.2 (Mar. 2005), pp. 269–275. ISSN: 0973-7138.

[12] M. Thiel. "Application of shock waves in medicine". In: *Clinical Orthopaedics and Related Research®* 387 (2001), pp. 18–21.

[13] A Sivakumar et al. "Effect of shock waves on dielectric properties of KDP crystal". In: *Journal of Electronic Materials* 47.8 (2018), pp. 4831–4839.

[14] Adrien Denoeud et al. "Dynamic X-ray diffraction observation of shocked solid iron up to 170 GPa". In: *Proceedings of the National Academy of Sciences* 113.28 (2016), pp. 7745–7749.

[15] Richard Renou et al. "Silica glass structural properties under elastic shock compression: Experiments and molecular simulations". In: *The Journal of Physical Chemistry C* 121.24 (2017), pp. 13324–13334.

[16] Tal Cohen and David Durban. "Longitudinal shock waves in solids: the piston shock analogue". In: *Proceedings of the Royal Society A: Mathematical, Physical and Engineering Sciences* 470.2164 (2014), p. 20130061.

[17] A Sivakumar et al. "Effect of shock waves on thermophysical properties of ADP and KDP crystals". In: *Optics & Laser Technology* 111 (2019), pp. 284–289.

[18] Uroš Trdan et al. "Application of massive laser shock processing for improvement of mechanical and tribological properties". In: *Surface and Coatings Technology* 342 (2018), pp. 1–11.

[19] Mathieu Ducousso et al. "Quantitative evaluation of the mechanical strength of titanium/composite bonding using laser-generated shock waves". In: *Applied Physics Letters* 112.11 (2018), p. 111904.

[20] Bob Nagler et al. “The matter in extreme conditions instrument at the Linac coherent light source”. In: *Journal of synchrotron radiation* 22.3 (2015), pp. 520–525.

[21] Mitchell A Wood et al. “Ultrafast chemistry under nonequilibrium conditions and the shock to deflagration transition at the nanoscale”. In: *The Journal of Physical Chemistry C* 119.38 (2015), pp. 22008–22015.

[22] Matthew Kuriakose et al. “Tailoring the blast exposure conditions in the shock tube for generating pure, primary shock waves: the end plate facilitates elimination of secondary loading of the specimen”. In: *PloS one* 11.9 (2016), e0161597.

[23] Curt Allan Bronkhorst et al. “Response and representation of ductile damage under varying shock loading conditions in tantalum”. In: *Journal of Applied Physics* 119.8 (2016), p. 085103.

[24] NV Saveleva et al. “Peculiarities of the elastic-plastic transition and failure in polycrystalline vanadium under shock-wave loading conditions”. In: *Technical Physics Letters* 41.6 (2015), pp. 579–582.

[25] Daniel Hawkins and John M Adams. *Shockwave nerve therapy system and method*. US Patent 9,237,984. 2016.

[26] Zi-jun Zou et al. “Low-intensity extracorporeal shock wave therapy for erectile dysfunction after radical prostatectomy: a review of preclinical studies”. In: *International journal of impotence research* 30.1 (2018), p. 1.

[27] Nikolaus B. M. Császár et al. “Radial Shock Wave Devices Generate Cavitation”. In: *PLOS ONE* 10.10 (Oct. 2015), pp. 1–19.

[28] Outi Supponen et al. “Shock waves from nonspherical cavitation bubbles”. In: *Physical Review Fluids* 2.9 (2017), p. 093601.

[29] Jing Luo and Zhipan Niu. “Jet and shock Wave from Collapse of two Cavitation Bubbles”. In: *Scientific reports* 9 (2019).

[30] GE Duvall and RA Graham. “Phase transitions under shock-wave loading”. In: *Reviews of Modern Physics* 49.3 (1977), p. 523.

[31] Sally June Tracy et al. “High-pressure phase transition in silicon carbide under shock loading using ultrafast X-ray diffraction”. In: *AGU Fall Meeting Abstracts*. 2017.

[32] SI Ashitkov et al. “The behavior of iron under ultrafast shock loading driven by a femtosecond laser”. In: *AIP Conference Proceedings*. Vol. 1793. 1. AIP Publishing. 2017, p. 100035.

[33] David R Jones et al. “The α–ω phase transition in shock-loaded titanium”. In: *Journal of Applied Physics* 122.4 (2017), p. 045902.

[34] S Zhao et al. “Amorphization and nanocrystallization of silicon under shock compression”. In: *Acta Materialia* 103 (2016), pp. 519–533.

[35] Dominik Kraus et al. “Nanosecond formation of diamond and lonsdaleite by shock compression of graphite”. In: *Nature communications* 7 (2016), p. 10970.

[36] Karl F Graff. *Wave motion in elastic solids*. Dover Publications, New York, 1975.

[37] Lord Rayleigh. “On waves propagated along the plane surface of an elastic solid”. In: *Proceedings of the London Mathematical Society* 1.1 (1885), pp. 4–11.

[38] Oldrich Novotny. “Seismic surface waves”. In: *Bahia, Salvador: Instituto de Geociencias* (1999).

[39] IA Viktorov. “Types of acoustic surface waves in solids/Review”. In: *Akusticheskii Zhurnal* 25 (1979), pp. 1–17.

[40] JG Scholte. “On the Stoneley wave equation”. In: *Proceedings of the Koninklijke Nederlandse Akademie van Wetenschappen* 45.part 1 (1942), pp. 20–25.

[41] Robert Stoneley. “Elastic waves at the surface of separation of two solids”. In: *Proceedings of the Royal Society of London. Series A, Containing Papers of a Mathematical and Physical Character* 106.738 (1924), pp. 416–428.

[42] AEH Love. “Buchbesprechungen über: Some Problems of Geodynamics.(Ref. A. UNSÖLD)”. In: *Zeitschrift fur Astrophysik* 67 (1967), p. 253.

[43] Horace Lamb. “On waves in an elastic plate”. In: *Proceedings of the Royal Society of London. Series A, Containing papers of a mathematical and physical character* 93.648 (1917), pp. 114–128.

[44] Sergey V Biryukov et al. *Surface acoustic waves in inhomogeneous media*. Vol. 20. Springer Science & Business Media, 2012.

[45] I. B. Zel'dovich et al. *Physics of shock waves and high-temperature hydrodynamic phenomena*. 1966.

[46] Xiong Zhang, Zhen Chen, and Yan Liu. "Chapter 2 - Governing Equations". In: *The Material Point Method*. Ed. by X. Zhang, Z. Chen, and Y. Liu. Oxford: Academic Press, 2017, pp. 11 –36. ISBN: 978-0-12-407716-4.

[47] D. S. Lemons and C. M. Lund. "Thermodynamics of high temperature, Mie–Gruneisen solids". In: *American Journal of Physics* 67.12 (1999), pp. 1105–1108.

[48] R. Valisetty et al. "HPC simulations of shock front evolution for a study of the shock precursor decay in a submicron thick nanocrystalline aluminum". In: *Modelling and Simulation in Materials Science and Engineering* 26.5 (Mar. 2018), p. 055008.

[49] J. H. Dymond and R. Malhotra. *The Tait-equation:100 years on*. Nov. 1988.

[50] Paul W Cooper. *Explosives engineering*. John Wiley & Sons, 2018.

[51] EE Meshkov. "Instability of the interface of two gases accelerated by a shock wave". In: *Fluid Dynamics* 4.5 (1969), pp. 101–104.

[52] J-Ch Robinet et al. "Shock wave instability and the carbuncle phenomenon: same intrinsic origin?" In: *Journal of Fluid Mechanics* 417 (2000), pp. 237–263.

[53] M Watanabe and K Takayama. "Stability of converging cylindrical shock waves". In: *Shock Waves* 1.2 (1991), pp. 149–160.

[54] J-Ch Robinet. "Bifurcations in shock-wave/laminar-boundary-layer interaction: global instability approach". In: *Journal of Fluid Mechanics* 579 (2007), pp. 85–112.

[55] CB Scruby and LE Drain. "Laser Ultrasonics: Techniques and Applications. 1990". In: *Bristol: Adam Hilger* (), pp. 116–123.

[56] C.B. Scruby. "Some applications of laser ultrasound". In: *Ultrasonics* 27.4 (1989), pp. 195 –209. ISSN: 0041-624X.

[57] T. C. Bor B. Pathiraj D. T. A. Matthews G. R. B. E. Römer H. Mustafa R. Pohl. "Picosecond-pulsed laser ablation of zinc: crater morphology and comparison of methods to determine ablation threshold". In: *Opt. Express* 26.14 (2018), pp. 18664–18683.

[58] B Sallé et al. "Femtosecond and picosecond laser microablation: ablation efficiency and laser microplasma expansion". In: *Applied Physics A* 69.1 (1999), S381–S383.

[59] Karl Heinz Leitz et al. "Metal ablation with short and ultrashort laser pulses". In: *Physics Procedia*. Vol. 12. PART 2. Elsevier, 2011, pp. 230–238.

[60] Boris N Chichkov et al. "Femtosecond, picosecond and nanosecond laser ablation of solids". In: *Applied physics A* 63.2 (1996), pp. 109–115.

[61] CK Jen et al. "Phase variation of focused surface acoustic wave". In: *Applied physics letters* 46.3 (1985), pp. 241–243.

[62] P Cielo, F Nadeau, and M Lamontagne. "Laser generation of convergent acoustic waves for materials inspection". In: *Ultrasonics* 23.2 (1985), pp. 55–62.

[63] Xiao Wang et al. "Focused bulk ultrasonic waves generated by ring-shaped laser illumination and application to flaw detection". In: *Journal of applied physics* 80.8 (1996), pp. 4274–4281.

[64] Zhonghua Shen et al. "Numerical simulation of the ultrasonic waves generated by ring-shaped laser illumination". In: *Chinese Optics Letters* 3.101 (2005), S335–S337.

[65] Jianfei Guan et al. "Numerical simulation of the ultrasonic waves generated by ring-shaped laser illumination patterns". In: *Optics & Laser Technology* 39.6 (2007), pp. 1281–1287.

[66] S. Dixon, T. J. Harrison, and P. A. Petcher. "Phase changes of ultrasonic bulk waves through focusing measured using a noncontact ultrasonic method". In: *Applied Physics Letters* 97.5 (2010), p. 054101. eprint: `https://doi.org/10.1063/1.3475926`.

[67] S Dixon et al. "Thermoelastic laser generated ultrasound using a ring source". In: *Journal of Physics D: Applied Physics* 45.17 (2012), p. 175103.

[68] D. Veysset et al. “Single-bubble and multibubble cavitation in water triggered by laser-driven focusing shock waves”. In: *Phys. Rev. E* 97 (5 May 2018), p. 053112.

[69] JP Cocchi, R Saurel, and JC Loraud. “Treatment of interface problems with Godunov-type schemes”. In: *Shock Waves* 5.6 (1996), pp. 347–357.

[70] Robert W Boyd. “Intuitive explanation of the phase anomaly of focused light beams”. In: *JOSA* 70.7 (1980), pp. 877–880.

[71] NCR Holme et al. “Gouy phase shift of single-cycle picosecond acoustic pulses”. In: *Applied physics letters* 83.2 (2003), pp. 392–394.

[72] Al A Kolomenskii, SN Jerebtsov, and HA Schuessler. “Focal transformation and the Gouy phase shift of converging one-cycle surface acoustic waves excited by femtosecond laser pulses”. In: *Optics letters* 30.15 (2005), pp. 2019–2021.

[73] S Zamiri et al. “Converging laser generated ultrasonic waves using annular patterns irradiation”. In: *Journal of Physics: Conference Series*. Vol. 520. 1. IOP Publishing. 2014, p. 012001.

[74] Jing Wang and Qibo Feng. “Converging ultrasonic shear-vertical waves generated by a double-line laser and its application for surface defect detection”. In: *Japanese Journal of Applied Physics* 54.4 (2015), p. 046602.

[75] VN Andreev et al. “Thermal conductivity of VO 2, V 3 O 5, and V 2 O 3”. In: *Physica Status Solidi. A, Applied Research* 48.2 (1978), K153–K156.

[76] HV Keer et al. “Heat capacity of pure and doped V2O3 single crystals”. In: *Journal of Solid State Chemistry* 19.1 (1976), pp. 95–102.

[77] Engineers Edge. *Thermal Diffusivity Table*. URL: `https://www.engineersedge.com/heat_transfer/thermal_diffusivity_table_13953.htm`.

[78] Amine Ould-Hamouda et al. “Single-shot time resolved study of the photo-reversible phase transition induced in flakes of Ti3O5 nanoparticles at room temperature”. In: *Chemical Physics Letters* 608 (2014), pp. 106–112.

[79] Elsa Abreu et al. "Ultrafast electron-lattice coupling dynamics in VO 2 and V 2 O 3 thin films". In: *Physical Review B* 96.9 (2017), p. 094309.

[80] G. D. Kahl and E. H. Wedemeyer. "Interferometric Analysis of Axisymmetric Plasma Flow". In: *The Physics of Fluids* 7.4 (1964), pp. 596–601. eprint: https://aip.scitation.org/doi/pdf/10.1063/1.1711244.

[81] Youssef Driss. *An Introduction to the Theory of Nonlinear Shock Waves*. Mar. 2017.

[82] Ludwig Mach. *Weitere Versuche über Projectile*. Carl Gerold, 1896.

[83] Gary A Sod. "A numerical study of a converging cylindrical shock". In: *Journal of fluid mechanics* 83.4 (1977), pp. 785–794.

[84] M Shabouei, R Ebrahimi, and K Mazaheri Body. "Numerical Solution of Cylindrically Converging Shock Waves". In: *arXiv preprint arXiv:1602.02680* (2016).

[85] Dante De Santis, Gianluca Geraci, and Alberto Guardone. "Node-pair finite volume/finite element schemes for the Euler equation in cylindrical and spherical coordinates". In: *Journal of Computational and Applied Mathematics* 236.18 (2012), pp. 4827–4839.

[86] T. Pezeril et al. "Direct Visualization of Laser-Driven Focusing Shock Waves". In: *Phys. Rev. Lett.* 106 (21 May 2011), p. 214503.

[87] K. Nagayama et al. "Shock Hugoniot compression curve for water up to 1 GPa by using a compressed gas gun". In: *Journal of Applied Physics* 91.1 (2002), pp. 476–482.

[88] Thorlabs. *UV Fused Silica High-Precision Windows*. URL: https://www.thorlabs.com/newgrouppage9.cfm?objectgroup_id=3983&pn=WG41050 (visited on 03/02/2020).

[89] Thorlabs. *N-BK7 High Precision Windows*. URL: https://www.thorlabs.com/newgrouppage9.cfm?objectgroup_id=1117&pn=WG11050 (visited on 03/02/2020).

[90] Dongxiao Han et al. "Thermal properties of carbon black aqueous nanofluids for solar absorption". In: *Nanoscale research letters* 6.1 (2011), p. 457.

[91] R. F. Trunin et al. "Compression of liquid organic substances in shock waves". In: *Khim. Fiz.* 11(3) (1992). in Russian, pp. 424–432.

[92] D. Veysset et al. "Acoustical breakdown of materials by focusing of laser-generated Rayleigh surface waves". In: *Applied Physics Letters* 111.3 (2017), p. 031901.

[93] K. T. Gahagan et al. "Ultrafast interferometric microscopy for laser-driven shock wave characterization". In: *Journal of Applied Physics* 92.7 (2002), pp. 3679–3682.

[94] D. Veysset et al. "Glass fracture by focusing of laser-generated nanosecond surface acoustic waves". In: *Scripta Materialia* 158 (2019), pp. 42 –45. ISSN: 1359-6462.

[95] Petra J van Koningsbruggen, Yonezo Maeda, and Hiroki Oshio. "Iron (III) spin crossover compounds". In: *Spin crossover in transition metal compounds I*. Springer, 2004, pp. 259–324.

[96] L Cambi and A Gagnasso. "Iron dithiocarbamates and nitrosodithiocarbamates". In: *Atti. Accad. Naz. Lincei* 13 (1931), pp. 809–813.

[97] JS Griffith. "On the magnetic properties of some haemoglobin complexes". In: *Proceedings of the Royal Society of London. Series A. Mathematical and Physical Sciences* 235.1200 (1956), pp. 23–36.

[98] WA Baker Jr and HM Bobonich. "Magnetic properties of some high-spin complexes of iron (II)". In: *Inorganic Chemistry* 3.8 (1964), pp. 1184–1188.

[99] Malcolm A Halcrow. *Spin-crossover materials: properties and applications*. John Wiley & Sons, 2013.

[100] Philipp Gütlich, Ana B Gaspar, and Yann Garcia. "Spin state switching in iron coordination compounds". In: *Beilstein journal of organic chemistry* 9.1 (2013), pp. 342–391.

[101] Keiichiro Nasu. *Photoinduced phase transitions*. World Scientific, 2004.

[102] Ian Lawthers and John J McGarvey. "Spin-state relaxation dynamics in iron (III) complexes: photochemical perturbation of the 2T. dbl-harw. 6A spin equilibrium by pulsed-laser irradiation in the ligand-to-metal charge-transfer absorption band". In: *Journal of the American Chemical Society* 106.15 (1984), pp. 4280–4282.

[103] S Decurtins et al. “Light-induced excited spin state trapping in a transition-metal complex: The hexa-1-propyltetrazole-iron (II) tetrafluoroborate spin-crossover system”. In: *Chemical physics letters* 105.1 (1984), pp. 1–4.

[104] Eric Collet. “Towards ultrafast photoinduced spin state switching”. In: *International Workshop Phase transition and Dynamical properties of Spin Transition Materials*. 2008.

[105] Maciej Lorenc et al. “Successive dynamical steps of photoinduced switching of a molecular Fe (III) spin-crossover material by time-resolved X-ray diffraction”. In: *Physical review letters* 103.2 (2009), p. 028301.

[106] Maciej Lorenc et al. “Cascading photoinduced, elastic, and thermal switching of spin states triggered by a femtosecond laser pulse in an Fe (III) molecular crystal”. In: *Physical Review B* 85.5 (2012), p. 054302.

[107] Roman Bertoni et al. “Femtosecond Spin-State Photoswitching of Molecular Nanocrystals Evidenced by Optical Spectroscopy”. In: *Angewandte Chemie International Edition* 51.30 (2012), pp. 7485–7489.

[108] Roman Bertoni et al. “Elastically driven cooperative response of a molecular material impacted by a laser pulse”. In: *Nature materials* 15.6 (2016), p. 606.

[109] Cristian Enachescu et al. “Model for elastic relaxation phenomena in finite 2D hexagonal molecular lattices”. In: *Physical review letters* 102.25 (2009), p. 257204.

[110] Laurentiu Stoleriu et al. “Thermal hysteresis in spin-crossover compounds studied within the mechanoelastic model and its potential application to nanoparticles”. In: *Physical Review B* 84.13 (2011), p. 134102.

[111] Antoine Tissot, Cristian Enachescu, and Marie-Laure Boillot. “Control of the thermal hysteresis of the prototypal spin-transition Fe II (phen) 2 (NCS) 2 compound via the microcrystallites environment: experiments and mechanoelastic model”. In: *Journal of Materials Chemistry* 22.38 (2012), pp. 20451–20457.

[112] Ludmila G Lavrenova et al. “Spin-crossover and thermochromism in complexes of iron (II) iodide and thiocyanate with 4-amino-1, 2, 4-triazole”. In: *Polyhedron* 14.10 (1995), pp. 1333–1337.

[113] O. Fouché et al. “Mechanism for optical switching of the spin crossover [Fe(NH2-trz)3](Br)2·3H2O compound at room temperature”. In: *Phys. Chem. Chem. Phys.* 12 (12 2010), pp. 3044–3052.

[114] E. D. Loutete-Dangui et al. “Thermal spin transition in $[\mathrm{Fe(NH_2-trz)_3}]\mathrm{Br_2}$ investigated by spectroscopic ellipsometry”. In: *Phys. Rev. B* 75 (18 2007), p. 184425.

[115] Victoria Shalabaeva et al. “Vacuum deposition of high-quality thin films displaying spin transition near room temperature”. In: *Journal of Materials Chemistry C* 5.18 (2017), pp. 4419–4425.

[116] Karl Ridier et al. “Finite Size Effects on the Switching Dynamics of Spin-Crossover Thin Films Photoexcited by a Femtosecond Laser Pulse”. In: *Advanced Materials* (2019), p. 1901361.

[117] KH Kim et al. *Colossal magnetoresistive manganites*. 2004.

[118] Jan H de Boer and Evert JW Verwey. “Semi-conductors with partially and with completely filled 3d-lattice bands”. In: *Proceedings of the Physical Society* 49.4S (1937), p. 59.

[119] NF Mott and R Peierls. “Discussion of the paper by de Boer and Verwey”. In: *Proceedings of the Physical Society* 49.4S (1937), p. 72.

[120] Nevill F Mott. “The basis of the electron theory of metals, with special reference to the transition metals”. In: *Proceedings of the Physical Society. Section A* 62.7 (1949), p. 416.

[121] E. Janod et al. “Resistive Switching in Mott Insulators and Correlated Systems”. In: *Advanced Functional Materials* 25.40 (2015), pp. 6287–6305.

[122] FJ Morin. “Oxides which show a metal-to-insulator transition at the Neel temperature”. In: *Physical review letters* 3.1 (1959), p. 34.

[123] NF Mott. “Metal-insulator transition”. In: *Reviews of Modern Physics* 40.4 (1968), p. 677.

[124] Masatoshi Imada, Atsushi Fujimori, and Yoshinori Tokura. “Metal-insulator transitions”. In: *Reviews of modern physics* 70.4 (1998), p. 1039.

[125] S. Ohkoshi et al. “Synthesis of a metal oxide with a room- temperature photoreversible phase transition”. In: *Nature Chemistry* 2 (July 2010), pp. 539–545.

[126] M. Foëx. “Étude dilatométrique et électrique de l’anomalie, présentée à basse température, par le sesquioxyde de vanadium”. In: *C. R. Acad. Sci.* 223 (1946), p. 1126.

[127] I. Lo Vecchio et al. “Optical properties of V_2O_3 in its whole phase diagram”. In: *Phys. Rev. B* 91 (15 Apr. 2015), p. 155133.

[128] JC Leiner et al. “Frustrated Magnetism in Mott Insulating (V 1- x Cr x) 2 O 3”. In: *Physical Review X* 9.1 (2019), p. 011035.

[129] S. Chen et al. “The effects of titanium or chromium doping on the crystal structure of V2O3”. In: *Journal of Solid State Chemistry* 44.2 (1982), pp. 192 –200. ISSN: 0022-4596.

[130] C. Tatsuyama and H. Y. Fan. “Raman scattering and phase transitions in V_2O_3 and $(V_{1-x}Cr_x)_2O_3$”. In: *Phys. Rev. B* 21 (7 Apr. 1980), pp. 2977–2983.

[131] M. Kadleikova, J. Breza, and M. Vesely. “Raman spectra of synthetic sapphire”. In: *Microelectronics Journal* 32.12 (2001), pp. 955 –958. ISSN: 0026-2692.

[132] H Senf and S Winkler. *Experimental Investigation of Wave and Fracture Phenomena in Impacted Ceramics: Sapphire.* Tech. rep. FRAUNHOFER-INST FUER KURZZEITDYNAMIK-ERNST-MACH-INST WEIL AM RHEIN (GERMANY), 1997.

Titre : Investigation de transitions de phases déclenchées par ondes de choc laser focalisantes

Mots clés : ultrasons générés par laser, ondes de choc, transitions de phase, matériaux bi-stables, coopérativité élastique

Résumé : La capacité de certains matériaux à changer d'état fondamental sous excitation laser a ouvert un champ de recherche autour de la manipulation de leurs propriétés par la lumière. Les processus chimiques et physiques mis alors en jeu sont riches et complexes. Dans ce contexte, le rôle prédominant de la coopérativité élastique pour l'amplification et la stabilisation de la transition a été mis en évidence récemment dans un matériau à transitions de spin irradié par laser. Ces observations font apparaître la perspective de commuter de façon permanente certaines propriétés des matériaux par des ultrasons non-linéaires, des ondes de choc excitées par laser. .

Dans un premier temps, nous introduisons le dispositif expérimental d'imagerie mono-coup résolu en temps, associée à la technique de focalisation des ondes de chocs excitées par laser au niveau de la surface de l'échantillon. La séparation spatiale des régions irradiées par le laser et influencées par les ondes de choc propagatives permet de discerner clairement les changements du matériaux induits uniquement par les ondes de choc. Dans un second temps, nous présentons nos résultats expérimentaux en lien avec cette technique innovante, aux matériaux dont les changements de phases impliquent un changement de volume macroscopique (systèmes spin-crossover, isolants de Mott). Des analyses post-mortem des échantillons ont permis de confirmer, dans certaines conditions expérimentales, une modification permanente de la phase du matériau par action de l'onde de choc. Ces résultats ouvrent de nombreuses perspectives pour la généralisation à de nombreux matériaux du phénomène de coopérativité élastique donnant lieu à des transitions de phases permanentes.

Title : Investigation of phase transitions triggered by laser-induced focusing shock waves

Keywords : laser ultrasonics, shock waves, phase transition, bi-stable materials, elastic cooperativity

The ability of certain materials to change its ground state due to laser excitation has arisen a lot of opportunities for light-control of material properties. The field of photo-induced phase transitions counts a rich variety of chemical and physical processes triggered by light-matter interactions involved during the phase transition process. Recently it was reported that elastically driven cooperativity leads to the amplification of spin state in molecular crystals and prolonged the lifetime of the transient state with an ultra-short laser pulse. The cooperative response appears during the propagation of non-linear coherent strain waves, in other words shock waves, coupled with the order parameter field. Shock waves can be seen as a new challenging pathway to achieve a permanently switched state with appropriate excitations. .

First, we introduce time-resolved single-shot imaging combined with the laser shock focusing technique that makes it possible to generate, acoustically focus, and directly visualize under a microscope shock waves propagating and focusing along the sample surface. The spatial separation of the laser-influenced and strain-influenced regions makes it possible to disentangle the material changes produced solely by the shock waves. Second, we present experimental results involving the shock-focusing technique to materials undergoing phase transitions linked with a macroscopic change of their volume (spin-crossover systems, Mott insulators). Post-mortem analyses of the samples confirm permanent phase transition under specific experimental conditions. These innovative results open doors for a generic elastically driven cooperativity.